HIGH-PERFORMANCE COPPER ALLOYS FABRICATED BY COLD SPRAY ADDITIVE MANUFACTURING

JIN SHENGXI

MPhil

The Hong Kong Polytechnic University

2025

The Hong Kong Polytechnic University

Department of Industrial and Systems Engineering

High-performance Copper Alloys Fabricated By Cold Spray Additive Manufacturing

JIN Shengxi

A thesis submitted in partial fulfilment of the requirements for the degree of Master of Philosophy

August 2025

Certificate of Originality

I declare that the thesis submitted by me is entirely my original work unless otherwise properly cited. Thus, to the best of my knowledge and belief, it does not contain any materials previously published or written by another person except where due reference is correctly cited.

Name: JIN Shengxi

Signature: ______________

Date: 15/08/2025

Table of Contents

Acknowledgements

First, I would like to express my great thanks of gratitude to my chief supervisor, Dr CHEN Zibin, who has given great favors to me during the whole process of my work, from the appropriate design of the experiments to the data analysis methodology, together with the patient revision of my manuscripts. I have benefited a lot from his encouragement, patience, and guidance. Additionally, I am deeply impressed by his serious approach to scientific research. Also, I would like to thank my co-supervisor, Professor Sandy To. She also provided me with a great deal of advice and guidance during my MPhil studies, particularly in the areas of scientific approaches and innovation.

Second, I would like to give my thanks to my excellent colleagues in our group. I am grateful to Mr LIU Qi, Mr DAN Xingdong, Mr CHEN Xuanlai, Ms SUN Yixuan, Mr Song Zizheng, Mr SHI Hengchao, Ms RAN Yating, Mr CHEN Yifan, Dr REN Chuanxi, Dr PU Ze, Dr ZHANG Dongdong, and Dr WEN Hongning for their support and companionship. They all helped me a lot in conducting the experiment as well as the operations of various experimental facilities. I am also moved by their enthusiasm and passion for research.

Also, I would like to acknowledge the help of Dr SUN Chengchuan and Dr LU Jing from Ji Hua Laboratory, Foshan, Guangdong Province, who helped with the preparation of the samples.

Finally, I would like to thank my parents as well as my friends for raising me when I faced problems. Thanks for their support from all perspectives.

List of Figures

Abstract

Copper and its alloys are critical materials in thermal and electrical industries due to their outstanding thermal and electrical conductivity. Their ability to efficiently transfer heat and electricity makes them indispensable in applications such as heat exchangers, electrical wiring, and electronic components. With the rapid development of high-end industrial components, the complexity of copper parts has extensively increased. Traditional manufacturing methods, such as casting and machining, often struggle to produce intricate designs cost-effectively. Additive manufacturing (AM) has emerged as a promising solution, offering design flexibility and reduced material waste. Among AM techniques, cold spray additive manufacturing (CSAM) stands out as a solid-state deposition process that minimizes thermal distortion and oxidation, making it ideal for producing high-quality copper components at a lower cost compared to laser-based AM methods.

Despite its advantages, cold-sprayed copper suffers from inferior mechanical properties, such as low strength and hardness, which limit its use in structural and high-load applications. Conventional approaches, such as incorporating hard ceramic particles or intermetallic compounds into the copper matrix, improve mechanical performance but drastically reduce thermal and electrical conductivity—key properties that make copper desirable in the first place. Therefore, alternative strengthening strategies must be developed to overcome this limitation without compromising the intrinsic advantages of copper.

This thesis aims to design and fabricate novel copper alloys via CSAM that achieve enhanced mechanical properties without sacrificing thermal and electrical conductivity. By optimizing alloy composition and processing parameters, the research seeks to develop materials that meet the demanding requirements of modern industrial applications. The successful implementation of such alloys would expand the use of CSAM in producing high-performance copper components, offering a cost-effective and efficient solution for advanced thermal and electrical systems.

Chapter 1 provides an overview of the distinctive properties of copper and its

alloys, along with their key industrial applications. Subsequently, it introduces CSAM, covering its historical development, deposition and bonding mechanisms, and current applications. Finally, the research challenges addressed in this thesis are outlined.

Chapter 2 details the experimental methodologies employed in this study. The sample preparation process is described, followed by an explanation of advanced electron microscopy techniques used for microstructural characterization, including scanning electron microscopy, electron backscatter diffraction, transmission electron microscopy, and scanning transmission electron microscopy. Additionally, the procedures for mechanical property testing, thermal and electrical conductivity measurements, and finite element method simulations are discussed.

Chapter 3 investigates a novel strategy to enhance the mechanical properties of cold-sprayed Cu while retaining its high conductivity through the introduction of Cu_2O nanoprecipitates. In this chapter, oxygen was introduced during the cold spray process to form Cu_2O precipitates within the Cu matrix. These precipitates strengthen the material with a yield strength of 480 MPa while maintaining exceptional thermal conductivity (310 W/m·K) and electrical conductivity (85.5% IACS). The precipitates pinned at grain boundaries effectively hinder the recovery and grain growth, thereby promoting the grain refinement and dislocation multiplication. This study presents a new approach for designing high-performance Cu-O alloys via nanoscale precipitate engineering, demonstrating significant potential for industrial applications.

Chapter 4 explores the fabrication of Cu-Sn alloys with superior compressive properties using CSAM. Bronze (Cu-Sn alloys) has been extensively utilized across industries throughout history. However, insufficient cooling rates in conventionally manufactured bronze often facilitate the formation of brittle δ-phase ($Cu_{41}Sn_{11}$) segregations that degrade mechanical properties. To overcome this limitation, CSAM was employed to deposit Cu-Sn alloys with controlled Sn content (5 wt.% and 10 wt.%) using pre-alloyed feedstock powders. The high deposition temperature and rapid cooling inherent to CSAM effectively suppressed δ-phase segregation. Notably, the heterogeneous Sn distribution in the Cu-10Sn alloy contributed to exceptional compressive performance (yield strength of approximately 1 GPa) compared to

Cu-5Sn and pure Cu. The higher Sn content lowers the recrystallization temperature of the alloy, thereby advocating the dynamic recrystallization during cold spray. The promoted grain refinement effect cooperated with segregated intermetallic compounds to enhance the mechanical properties of the as-sprayed Cu-10Sn alloys. This study demonstrates the feasibility of producing high-strength Cu-Sn alloys via CSAM while elucidating microstructural changes during deposition.

Chapter 5 summarizes the key findings of this research and proposes future directions for further investigation.

Chapter 1 Introduction

1.1. Cu and Cu based materials

The demand for Cu and copper-based materials has grown sharply in recent decades, accompanied by a surge in related research publications since 2000. According to Watari et al. [1], global Cu consumption has increased from approximately 30 million tons per year to about 100 million tons per year, representing a more than 330% increase (**Fig. 1-1**). This rapid expansion is driven by Cu's unique combination of properties: exceptional thermal and electrical conductivity, good ductility, and notable corrosion resistance. These characteristics make Cu difficult to replace with other commonly used metals, ensuring its continued relevance across a wide range of industrial applications.

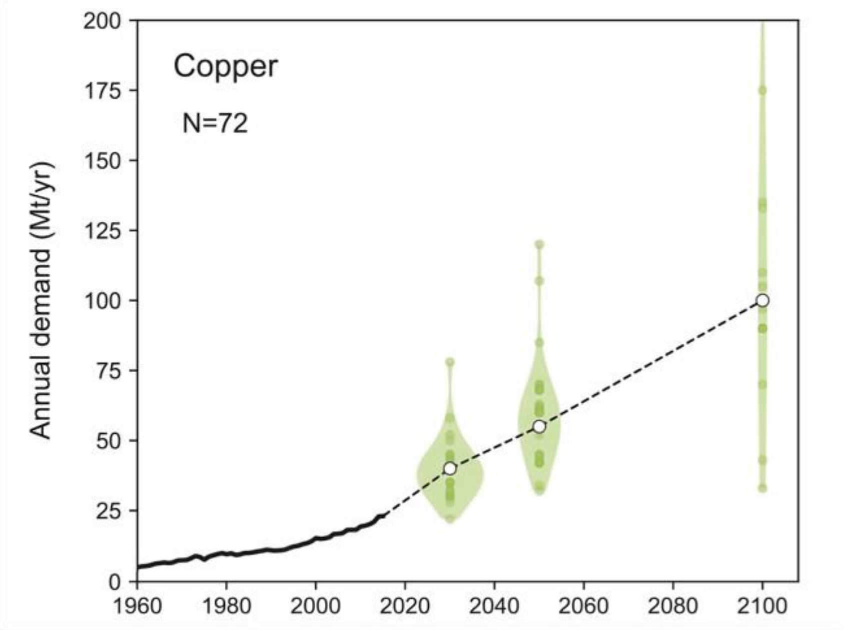

Fig. 1- 1 Prediction of the increasing demand for Cu by 2100. The circles signify the median of the collected data. N refers to the amount of data. The data were collected from World Bureau Metal Statistics in 2015 [1].

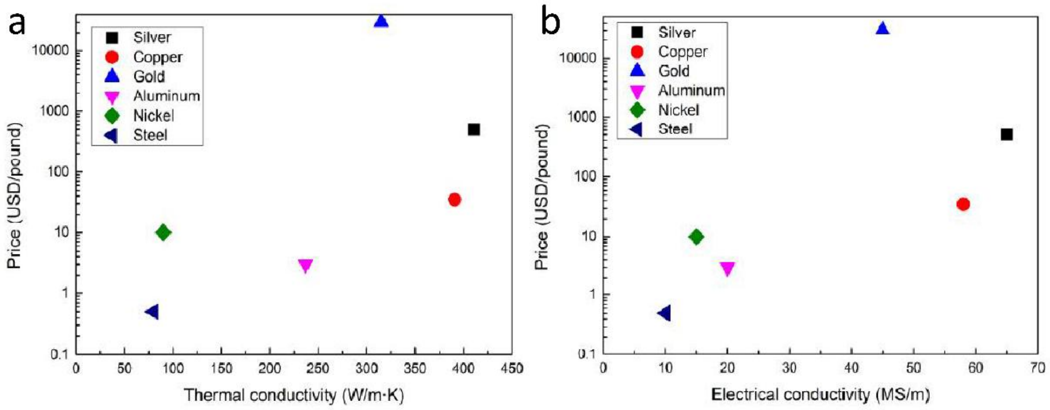

Fig. 1- 2 Comparison between (a) Thermal conductivity, (b) Electrical conductivity, and price (Jul. 2024) among several commonly used metals [2].

Compared with other commonly used metals, Cu offers a strong advantage in both thermal and electrical conductivity. As shown in **Fig. 1-2**, its performance in these properties is second only to silver (Ag), surpassing all others. However, Ag's significantly higher cost limits its large-scale production and use. In contrast, aluminum, steel, and nickel are less expensive than Cu, but their much lower thermal and electrical conductivities make them unsuitable for many thermal and electrical industry applications.

Cu's combination of high conductivity, good ductility, and relatively low cost supports its widespread use across numerous industrial sectors [3-5]. As illustrated in **Fig. 1-3**, its superior electrical conductivity makes it an ideal material for applications such as wiring, generator components, and electron tubes. In addition, its excellent thermal conductivity enables the production of heat sinks and condensers with complex geometries, delivering higher heat transfer efficiency than conventional aluminum-based radiators. Apart from those Cu based products, various Cu alloys also play critical roles in construction, electricity, and refrigeration industries. Among those, tin-bronze, known as Cu-Sn alloy, is one of the most widely used Cu alloys throughout human history. The excellent wear and corrosion resistance enable their primary applications in bearings, gears, as well as marine applications. Along with the increasing demand for Cu alloys with high strength, wear, and corrosion resistance, it is critical to design and optimize the structure of such alloys to achieve desired properties.

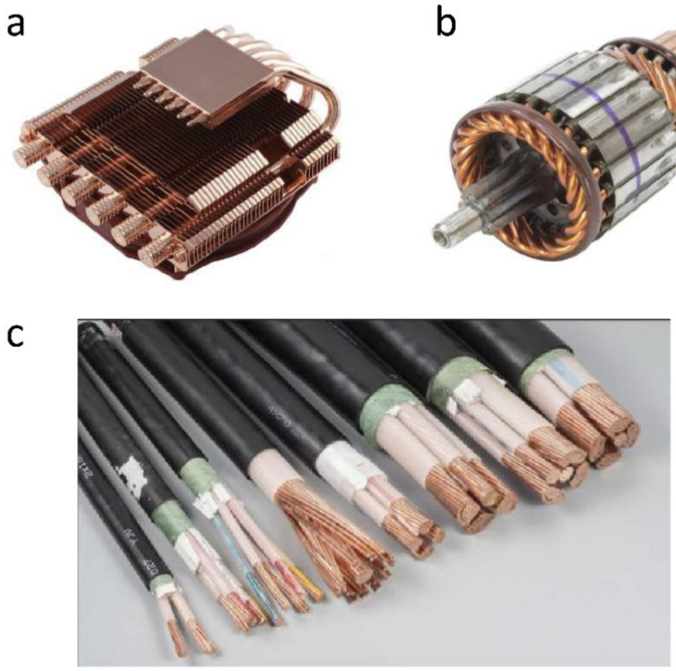

Fig. 1-3 Various applications of Cu. (a) Cu based radiators; (b) Cu component in generators; (c) Cu wires [6].

Although copper exhibits excellent thermal and electrical conductivity, Cu and Cu-based products often experience various forms of failure - including deformation, breakdown, and corrosion - after extended periods of service. These issues present significant challenges to their broader application.[7]. These limitations are particularly critical in the heat sink industry, where prolonged high-temperature exposure causes thermal softening, reducing hardness and strength. As a result, Cu components become more susceptible to deformation and failure, shortening their service life and restricting their use in demanding environments. Because many of these components are complex in shape and essential to industrial systems, replacement is both costly and time-consuming. Moreover, reliance on imported parts can be subject to external supply constraints. Therefore, developing effective methods for restoring Cu-based products is of considerable technical and economic importance.

Currently, common methods for repairing and remanufacturing Cu components include electroplating, thermal spraying, arc spraying, and plasma or laser cladding [8-11]. While each technique has its advantages, all introduce significant thermal effects during processing. Because Cu and its alloys are highly sensitive to heat, such thermal exposure can degrade their original properties and compromise performance. Therefore, there is a pressing need to develop novel manufacturing and restoration methods that combine high efficiency with minimal thermal impact, ensuring the reliable recovery and extended service life of Cu and Cu-based materials.

1.2. Cu fabricated by CSAM

1.2.1. Introduction to CSAM

Cold spray, a solid-state material deposition process [12-15], has attracted significant attention from both engineers and researchers in recent years. The technology was developed in the 1990s by Anatolii Papyrin [16] of the former Soviet Union. During a wind tunnel experiment, his team observed that particles traveling above a certain velocity adhered to the substrate instead of causing erosion. Continued experimentation led to the development of this novel manufacturing method. A schematic of a cold spray system is shown in **Fig. 1-4**. In this process, inert gases such as N_2, He, or Ar are used as carrier gases. Under high temperature and pressure, these gases accelerate metal powders through a specially designed De Laval nozzle, further increasing their velocity. Upon impact with the substrate—at speeds exceeding 600 m/s—the particles undergo severe plastic deformation and form a dense coating without melting [12-15].

Table 1-1 compares cold spray with laser-based additive manufacturing methods. Unlike conventional fusion-based techniques, cold spray deposits solid particles without inducing melting or phase transitions, and with minimal oxidation during spraying. This approach preserves the original properties of the feedstock powders, achieves high deposition efficiency, reduces costs, minimizes thermal impact on the substrate, and generates little material waste [17, 18]. These advantages make it particularly well-suited for repairing Cu-based components that are sensitive to temperature changes.

Initially, cold spray was applied to produce compact coatings on various substrates to enhance corrosion and wear resistance [19]. Subsequent research has focused on improving equipment design, optimizing spraying parameters, conducting simulations, and analyzing microstructural evolution. These efforts have advanced cold spray into a mature and effective surface-coating technology, paving the way for broader industrial applications.

With advances in cold spray equipment, the use of higher gas temperatures and pressures has increased coating thickness from several hundred micrometers to over 5 mm, offering new opportunities for additive manufacturing. Cold spray can now deposit a wide range of materials, including metals, ceramics, and composites. Among metallic feedstocks, Cu and Al are the most used, with substantial research published in the first two decades of the 21st century [20-24]. As this technology has matured, innovative approaches combining cold spray with auxiliary techniques have emerged. For example, laser assistance can soften feedstock powders to achieve higher deposition density; magnetic fields can further accelerate particles to increase velocity; and friction stir processing (FSP) can modify as-sprayed surfaces to enhance mechanical performance [25]. These combined methods, collectively known as CSAM, have been applied in manufacturing diverse engineering components to meet industrial needs, driving the demand for high-performance Cu and Cu-based materials.

Table 1-1 Comprehensive comparison of CSAM with other laser-based additive manufacturing methods

	CSAM	EBM	LMD	SLM
Powder fusion	No	Yes	Yes	Yes
Product size	Large	Limited	Limited	Limited
Fabrication time	Short	Long	Long	Long
Flexibility	High	Low	Low	Low
Feasible for repair	Yes	No	No	No
Cost	Low	High	High	High

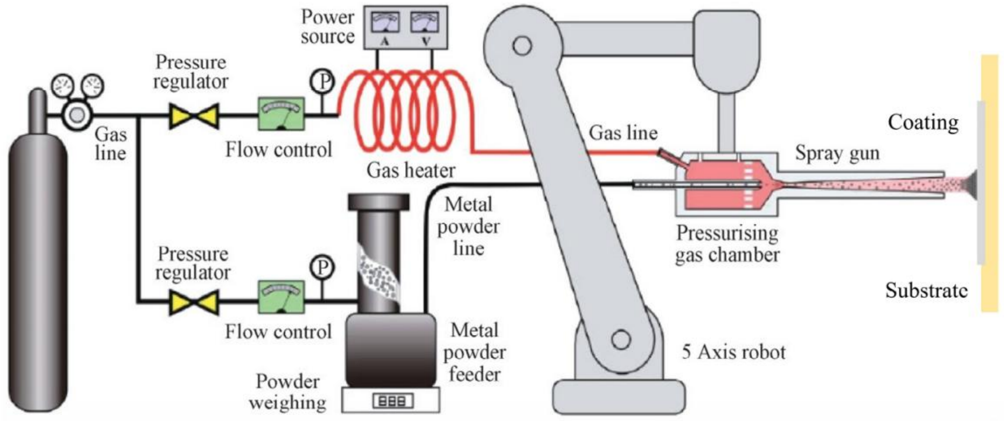

Fig. 1- 4 Schematic diagram of cold spray system [13].

1.2.2. Cold spray deposition mechanism

Since its invention, the formation mechanism of cold spray deposition has been a subject of extensive research, yet no consensus has been reached. One of the most widely accepted theories is the adiabatic shear instability (ASI) model proposed by Assadi et al. [26]. According to this theory, high-velocity particle impact induces intense plastic deformation and work hardening. Due to the extremely short impact duration, kinetic energy rapidly converts to thermal energy with minimal heat transfer, causing a localized temperature to rise at the interface that leads to adiabatic softening. When softening surpasses work hardening, plastic flow and a metal jet form at the interface, triggering ASI and completing deposition.

Building on Assadi’s work, Grujici et al. [27] studied different metals’ responses to ASI, finding that the metal jet breaks oxide films on particles and substrate surfaces, enhancing metallurgical bonding by increasing fresh metal contact area. This bonding is essential for coating formation. However, Hassani-Gangardj et al. [28] argued that ASI is not always necessary for bonding and that metal jet formation can result from extreme pressure gradients at particle interfaces, similar to explosive welding. Fardan et al. [29] modeled the ASI process (**Fig. 1-5**), showing temperature and strain evolution during impact, with jetting occurring where adiabatic softening exceeds work hardening (**Fig. 1-5(a)**). Conversely, Hassani-Gangardj [30] proposed that hydrodynamic plasticity, driven by pressure gradient release rather than ASI, causes bonding. During deposition, uneven shock wave compression in particles and substrate leads to jetting once hydrodynamic stress surpasses particle flow stress (**Fig. 1-5(b)**). This aligns with studies on hyper-velocity impacts like explosive welding [31]. These differing perspectives highlight ongoing debate and underscore the need for further investigation into the cold spray deposition mechanism.

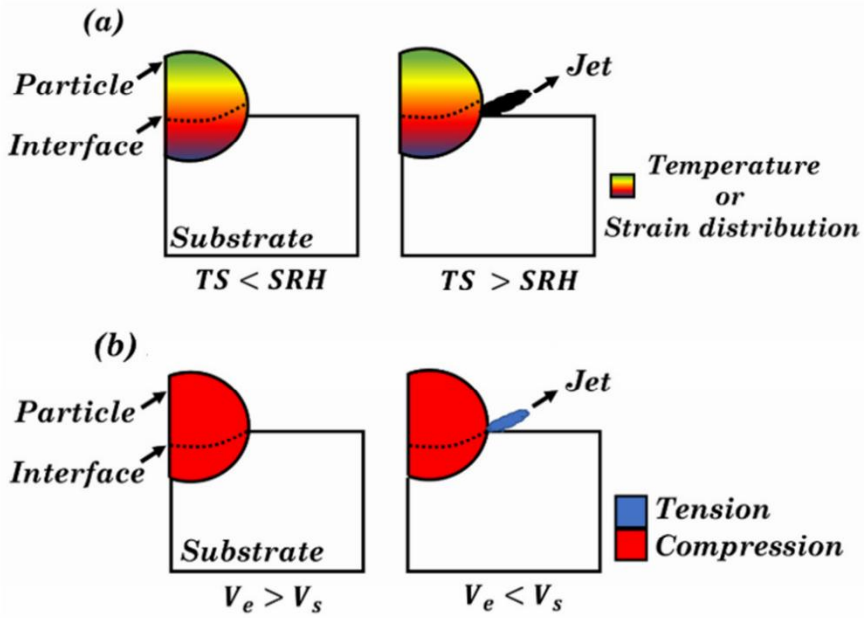

Fig. 1- 5 Schematic diagram of jet formation during deposition. a) ASI during deposition raised by Assadi et al. [26] and b) hydrodynamic plasticity during particle deposition by Hassani et al. [28]. Here, TS refers to thermal softening, SRH signifies strain rate hardening, Ve and Vs represent edge velocity and shock velocity.

1.2.3. Bonding mechanism of cold spray

Currently, four bonding mechanisms are recognized for cold-sprayed coatings based on the ASI deposition theory: physical, chemical, mechanical, and metallurgical bonding. Different materials and deposition conditions can result in one or more of these mechanisms contributing to inter-particle bonding. Hussain et al. [30] explained that metal jets formed after ASI break oxide films on coating surfaces, increasing fresh metal contact and promoting physical bonding driven mainly by Van der Waals forces under high pressure. Moridi et al. [32] focused on mechanical bonding, describing how pressure gradients during particle impact cause plastic deformation and metal jet formation. The resulting uneven particle interfaces create mechanical interlocks that strengthen bonding. Xie et al. [33] studied nickel coatings on aluminum substrates and identified chemical bonding through the formation of an Al_3Ni intermetallic compound, induced by the localized high temperatures generated during impact. Meanwhile, Grujicic et al. [34] argued that the heat generated during impact can elevate the interface temperature sufficiently to induce partial melting of the substrate surface. This process facilitates metallurgical bonding not only between the coating and the substrate but also among adjacent particles.

In summary, physical and mechanical bonding occur almost simultaneously during cold spray deposition. Typically, particles are mechanically entrapped by the softer substrate, forming interlocks that initiate mechanical bonding [13]. This mechanical bonding primarily governs the interfacial adhesion in cold-sprayed coatings. Metallurgical bonding, often arising from chemical bonding through atomic diffusion, generally exhibits superior mechanical properties [35-38]. However, because the temperature rise during cold spray is relatively low and bonding mainly results from intense particle deformation, mechanical bonding remains the dominant mechanism in most cold-sprayed coatings [39-41].

1.2.4. Cu and Cu based materials fabricated by CSAM

Cold spray has been widely adopted for fabricating metals, ceramics, composites, and even amorphous materials, with Cu and Cu-based materials among the earliest applications. Numerous studies have confirmed the feasibility of producing Cu coatings and bulk parts via cold spray additive manufacturing (CSAM). In 2008, Koivuluoto et al. [42] fabricated Cu coatings using low-pressure cold spray at 540 ℃ and 0.6 MPa driving gas pressure. The resulting coatings, shown in **Fig. 1-6**, were relatively dense but contained some weak bond interfaces. Heat treatment improved coating compactness by healing pores and reducing weak interfaces, though hardness dropped significantly—from 105 HV0.3 in as-sprayed samples after treatment.

Four years later, Koivuluoto [43] compared Cu coatings produced under high and low spraying pressures, finding that increased pressure enhanced both coating density and microhardness. Sundararajan et al. [44] examined the effect of heat treatment temperature on porosity and mechanical properties of Cu coatings, concluding that higher annealing temperatures reduced porosity via recovery and recrystallization but significantly degraded mechanical performance, including hardness and elastic modulus.

To further strengthen cold-sprayed Cu coatings, many efforts have focused on optimizing spraying parameters, modifying carrier gases, powder metallurgy, and post-treatments [45-47]. For example, Phani et al. [45] investigated vacuum and air heat treatments at varying temperatures and durations, establishing linear relationships between porosity, microhardness, and electrical conductivity in as-sprayed and heat-treated coatings. Li et al. [46] developed a novel feedstock combining gas-atomized Cu powders (GA Cu) with porous dendritic powders from electrolysis (E Cu). The porous E Cu filled gaps among solid GA Cu powders, yielding coatings with improved compactness, mechanical properties, and corrosion resistance. Zou et al. [47] replaced commonly used nitrogen with helium as the carrier gas, achieving nearly pore-free microstructures and superior mechanical and conductive properties.

However, these approaches have inherent limitations. Helium is 20 to 100 times more expensive than nitrogen, limiting economic feasibility for large-scale production. While annealing reduces pores and weak interfaces, recovery and grain growth inevitably degrade mechanical strength. Additionally, annealing in air causes surface oxidation, and vacuum annealing entails high costs.

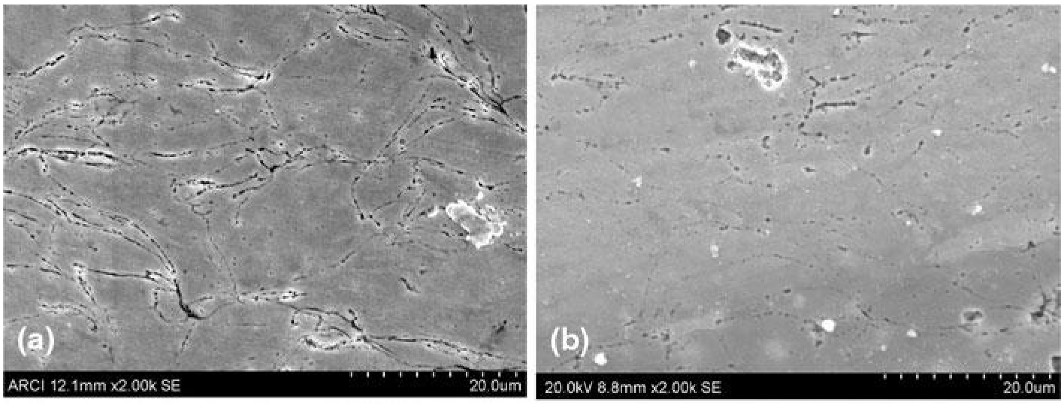

Fig. 1- 6 Cross-sectional microstructure of cold-sprayed Cu coatings. (a) As-sprayed sample. (b) Sample after heat treatment [44].

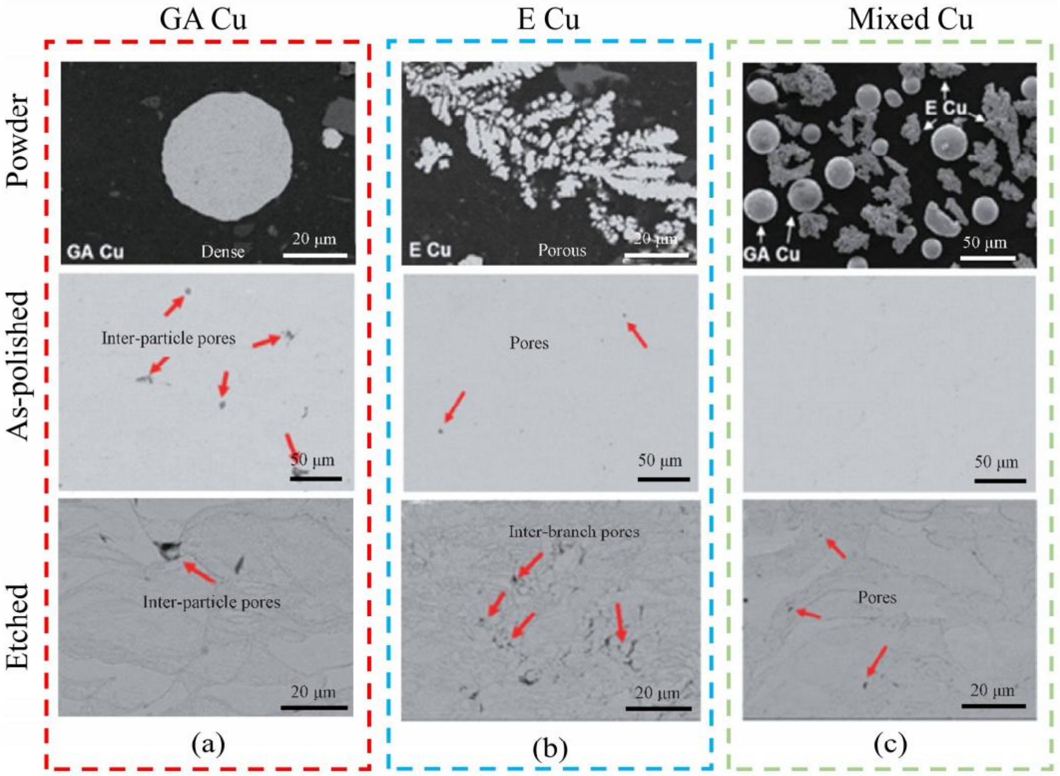

Fig. 1- 7 Cross-sectional microstructure of different feedstock Cu powders and the as-sprayed samples showcasing elimination of the interparticle pores by the mixture of GA and E Cu powders [46].

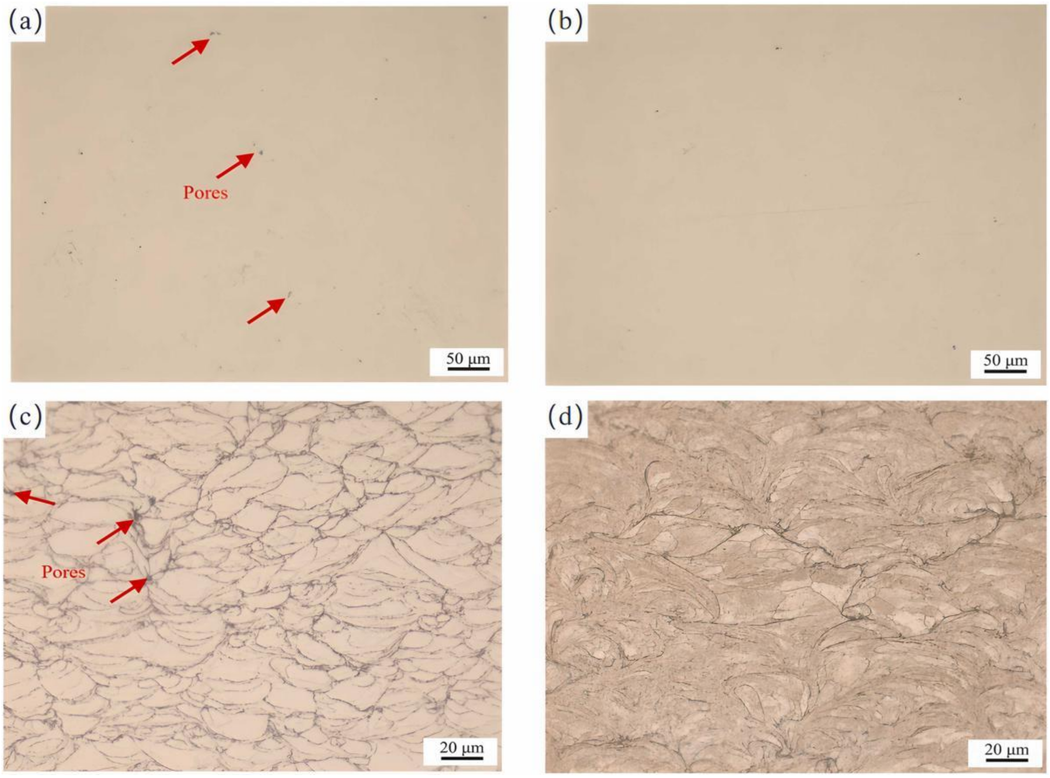

Fig. 1-8 Cross-sectional optical micrograph of the cold-sprayed Cu deposits by different carrier gases [47]. (a) Deposits fabricated via Nitrogen. (b) Deposits fabricated via Helium. (c) and (d) refer to the etched cross-sectional optical micrograph of (a) and (b), respectively.

Previous research shows that the mechanical properties of cold-sprayed Cu remain inadequate for many applications. Although severe plastic deformation and work hardening can increase the hardness and strength of cold-sprayed Cu compared to cast Cu, its relatively low mechanical strength still makes it prone to deformation. This limits the effectiveness of restoration and challenges its long-term performance. Therefore, further strengthening of cold-sprayed Cu before use is essential.

Common metal strengthening methods include solid solution strengthening, grain refinement, dislocation strengthening, and secondary phase strengthening. According to Ghosh et al. [48], grain refinement combined with deformation strengthening is the most effective approach for Cu. Work hardening increases dislocation density, while grain refinement raises grain boundary area—both contributing to enhanced strength [3]. However, excessive deformation can lead to dislocation accumulation and crack formation, reducing ductility. Moreover, these strengthening techniques typically require complex and time-consuming post-processing steps.

Secondary phase strengthening is widely applied in Cu and its alloys through the development of Cu-based composites, where Cu serves as the matrix, and hard reinforcements such as ceramics, diamond, graphene, metallic glasses, and nanoparticles are incorporated. This combination leverages the excellent ductility and machinability of Cu with the superior hardness and wear/corrosion resistance of ceramic phases. Coatings produced from these composites exhibit low porosity and strong interfacial bonding, resulting in enhanced wear resistance, corrosion protection, and mechanical performance, which broadens their industrial applicability [49-52]. Numerous studies have focused on fabricating high-performance cold-sprayed Cu-based composites, summarized in **Table 1-2**. For example, Cao et al. [49] added 15 wt.% SiC or Al_2O_3 to pure Cu, increasing microhardness to approximately 167 HV0.2. Both reinforcements yielded similar effects, and tribological tests demonstrated that the incorporation of hard ceramic phases significantly enhanced wear resistance compared to pure Cu coatings. Zhang et al. [50] incorporated 1.8 wt.% MoS_2 into the Cu matrix, which reduced the friction coefficient notably during sliding tests. The MoS_2 acted as a solid lubricant, replenishing worn areas and enhancing self-lubrication. Going beyond single-phase reinforcement, Bai et al. [51] introduced a Cu_2O/SiO_2 glass phase into Cu-SiC composites. By controlling glass content and annealing temperature, they achieved a friction coefficient of about 0.34 and a wear rate of 1.12×10^{-5} $mm^3/(N \cdot m)$ with 5 wt.% glass phase, offering a promising approach for wear-resistant Cu/SiC composites in high-temperature environments. Chang et al. [52] fabricated Cu-Cr coatings with ~15 wt.% Cr, enhancing microhardness to 145.7 HV while retaining 53% of annealed Cu's electrical conductivity, demonstrating potential for applications requiring both high strength and good conductivity.

With continual advancements in spraying equipment, cold spray technology has rapidly progressed both theoretically and experimentally. Research on cold-sprayed coatings has shifted from fundamental studies and process optimization to large-scale industrial production. As an efficient coating fabrication method, cold spray provides an ideal approach for producing Cu-based composite coatings with superior performance, thanks to its high kinetic energy, low thermal impact, efficiency, and cost-effectiveness. Growing experimental evidence supports the development of cold-sprayed Cu-based composites with excellent conductivity, wear resistance, and corrosion resistance, paving the way for their expanded industrial applications.

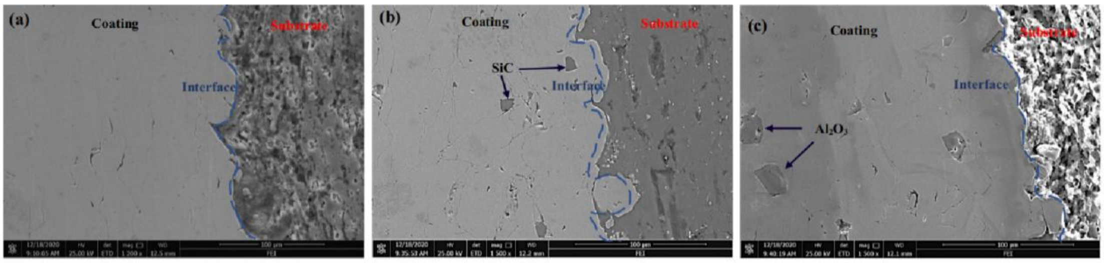

Fig. 1-9 Cross-sectional micrograph of the cold-sprayed Cu-ceramic composites [49]. (a) Cross-section of cold sprayed pure Cu. (b) Cross-section of cold sprayed Cu-SiC. (c) Cross-section of cold-sprayed Cu-Al_2O_3. The interfaces between coatings and substrate were marked by blue dashed lines individually.

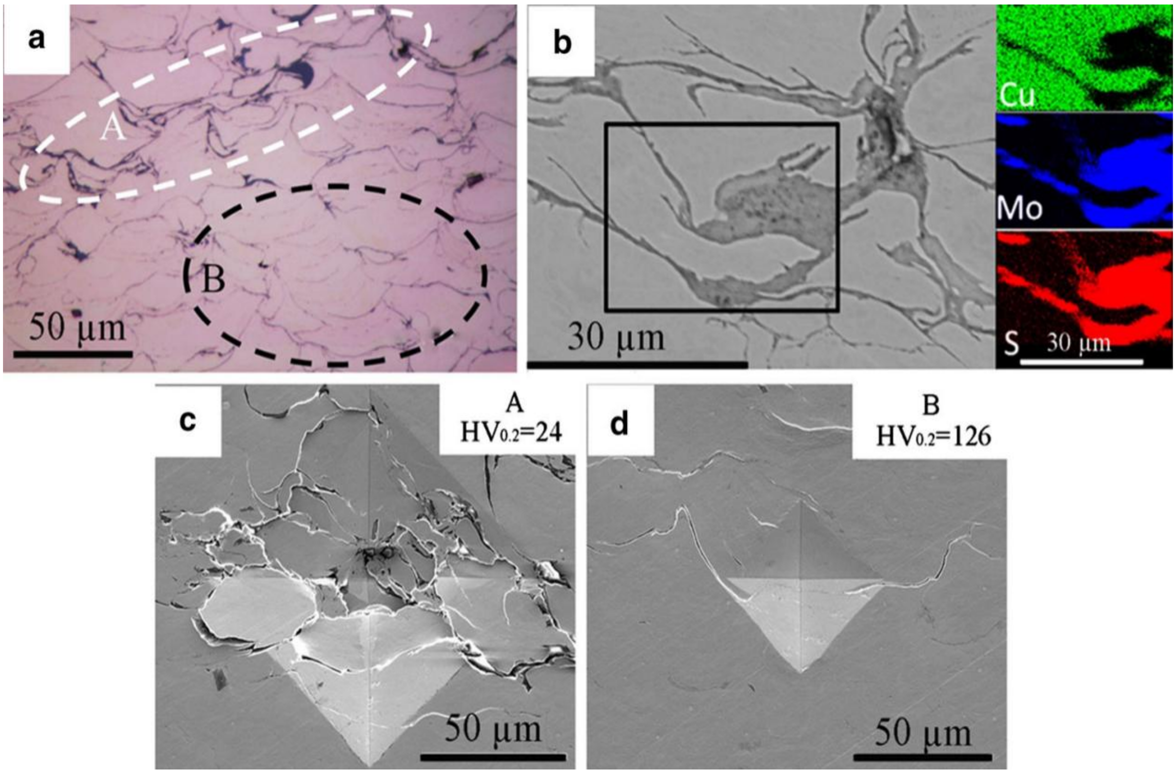

Fig. 1-10 Cross-sectional morphology of cold-sprayed Cu-MoS_2 coatings [50]. (a) Optical microscope images of cold sprayed Cu-MoS_2. (b) EDX mappings show the Cu, Mo and S composition in the rectangular area marked. (c) and (d) indentations of the microhardness test in

the region marked in (a), respectively.

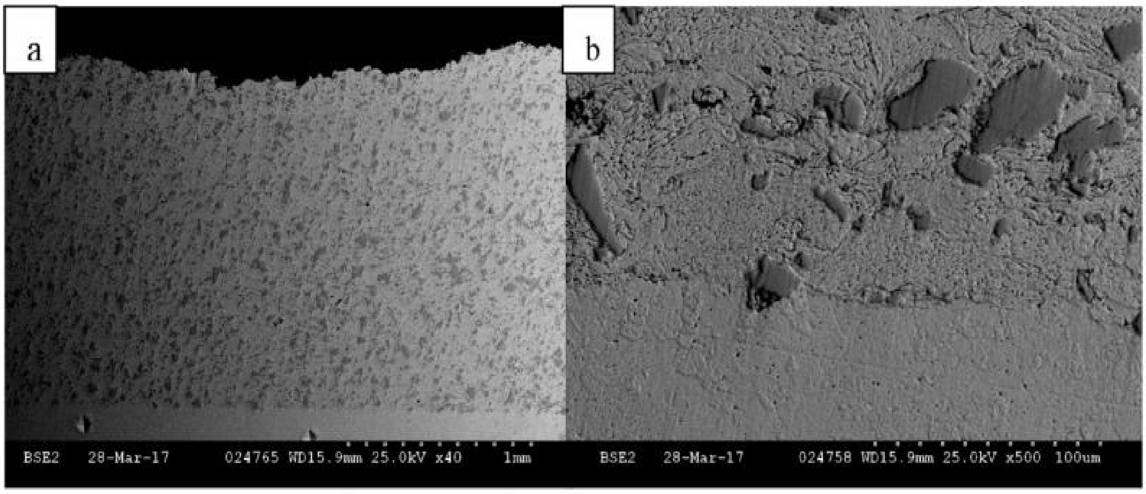

Fig. 1- 11 The SEM graphs of the as-fabricated Cu-Cr coatings after etching [52]. (b) is the magnified SEM image of the interface region in (a).

Table 1-2 The compositions, hardness, and relevant properties of various typical cold-sprayed Cu-based composites reported in literature.

Deposition	Composition	Hardness	Properties	Ref.
Cu/Al_2O_3	Cu+50%Al_2O_3	127HV0.3	Wear/corrosion resistant	[43]
Cu/Al_2Cu	Cu/Al_2Cu (5,10,15 wt.%)	132HV0.025	Conductive	[53]
Cu/Ni	Cu/Ni (6/16/3/48 wt.%)	190HV0.1	Corrosion resistant	[54]
Cu/SiC Cu/Al_2O_3	Cu+15%SiC Cu+15%Al_2O_3	~167HV0.2	Wear-resistant and thermally conductive	[49]
Cu/SiC +Cu_2O/SiO_2	Cu/SiC+Cu_2O/SiO_2 (3,5,7,9vol%)	~140HV	Improved tribological performance	[51]
Cu/MoS_2	Cu/MoS_2 (1.8 wt.%)	124HV0.2	Self-lubricating	[50]
Cu/Cr	Cu+25%Cr	145HV	Hard and conductive	[52]

1.3. Issues to be addressed

Based on the aforementioned background of research, Cu and Cu-based materials have wide applications in thermal and electrical fields. Cold spray additive manufacturing (CSAM) offers an efficient, cost-effective, and low-waste method for restoring and fabricating these materials compared to conventional fusion-based processes. However, challenges remain in CSAM-produced Cu materials. One major issue is the trade-off between strength and thermal/electrical conductivity. To address this, we introduced oxygen into the Cu matrix to strengthen the material while preserving competitive conductivity, as detailed in Chapter 3. After exploration of employing oxygen as a strengthening agent, the precipitation strengthening appeared to be an ideal strengthening approach for cold-sprayed Cu and Cu based materials. The existence of precipitation could significantly modify the microstructure of the as-sprayed Cu deposition. To achieve better mechanical properties to meet industrial demands for high-strength Cu alloys, the selection of an appropriate strengthening phase is critical. Considering the various intermetallic compounds that could achieve such a strengthening effect, the Sn element was chosen as a potential alloying agent in the Cu matrix throughout CSAM. To identify the influence of different Sn content on the microstructure and properties of as-sprayed Cu-Sn alloys, pre-alloyed Cu-Sn powders with Sn content controlled at 5 wt.% and 10 wt.% were employed for the fabrication of Cu-5Sn and Cu-10Sn alloys. Microstructural characterization and preliminary discussion of strengthening mechanisms are presented in Chapter 4.

1.3.1. The strength-conductivity dilemma of cold-sprayed Cu remains to be overcome

The literature review indicates that a variety of approaches—including optimization of processing parameters, modification of spraying gases, post-treatment techniques, and the incorporation of secondary phases—have been employed to enhance the mechanical performance of cold-sprayed Cu. Among these, incorporating secondary phases like intermetallic compounds, ceramics, and amorphous materials is the most effective strengthening approach. However, adding hard ceramic components significantly reduces both thermal and electrical conductivity, as these phases hinder heat and electron transport. **Fig. 1-12** compares hardness and thermal/electrical conductivity of Cu-based composites, showing that nearly all have thermal conductivity below 250 W/m·K, while pure cast Cu reaches 391 W/m·K.

Similarly, electrical conductivity for most composites is below 60% IACS, far lower than the 100% IACS of annealed Cu. Thus, while ceramic and intermetallic additions improve hardness, they do so at a substantial cost to conductivity. This underscores the pressing need for innovative strategies to address the inherent trade-off between strength and conductivity.

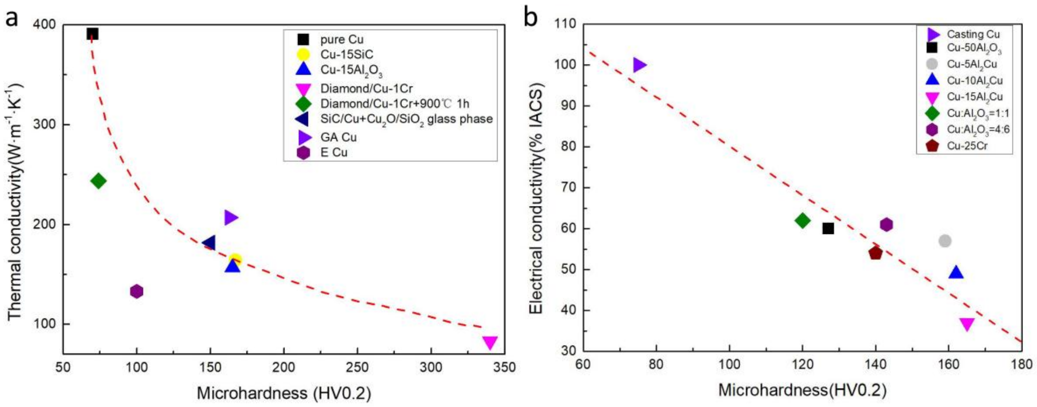

Fig. 1-12 A comprehensive comparison of the performances among the cold-sprayed Cu-based composites [43, 46, 49, 51-53, 55]. (a) Comparison between microhardness and thermal conductivity among the Cu-based composites. (b) Comparison between microhardness and electrical conductivity among these composites.

Selecting an appropriate secondary phase is critical to enhancing mechanical properties while maintaining competitive conductivity in Cu alloys. Recent studies indicate that oxygen is a promising strengthening agent in Cu. The Cu–O phase diagram [56], shown in **Fig. 1-13**, reveals that oxygen has very low solubility in Cu, leading to the formation of Cu_2O precipitates during solidification. Several works have explored Cu–O alloys with excellent strength and conductivity. For example, Liu et al. [57] used laser powder bed fusion (LPBF) to produce Cu–O alloys with 0.3 and 0.6 wt.% oxygen. The Cu–0.6O alloy exhibited a cellular microstructure with Cu_2O nanoprecipitates and achieved a tensile strength of 496.1 MPa alongside 68% IACS electrical conductivity. Similarly, Gu et al. [58] fabricated Cu–0.89O alloy via laser remelting, attaining high density, 405 MPa tensile strength, and approximately 74% IACS conductivity. However, these approaches are limited to laser-based additive manufacturing, and oxygen introduction via cold spray additive manufacturing (CSAM) remains unexplored.

To address this gap, we conducted a systematic study on cold-sprayed Cu–O alloys, detailed in Chapter 3. Gas-atomized Cu powders intentionally oxidized to 0.2 wt.% oxygen were used as feedstock. This enabled the formation of Cu_2O precipitates segregated at grain boundaries during deposition. The precipitates strengthened the material, increasing microhardness to ~136 HV and compressive yield strength to ~470 MPa, outperforming pure cold-sprayed Cu. At the same time, exceptional thermal conductivity (310 W/m·K) and electrical conductivity (85.5% IACS) were achieved, representing a breakthrough in overcoming the strength–conductivity trade-off in cold-sprayed Cu alloys and demonstrating promising potential for industrial applications.

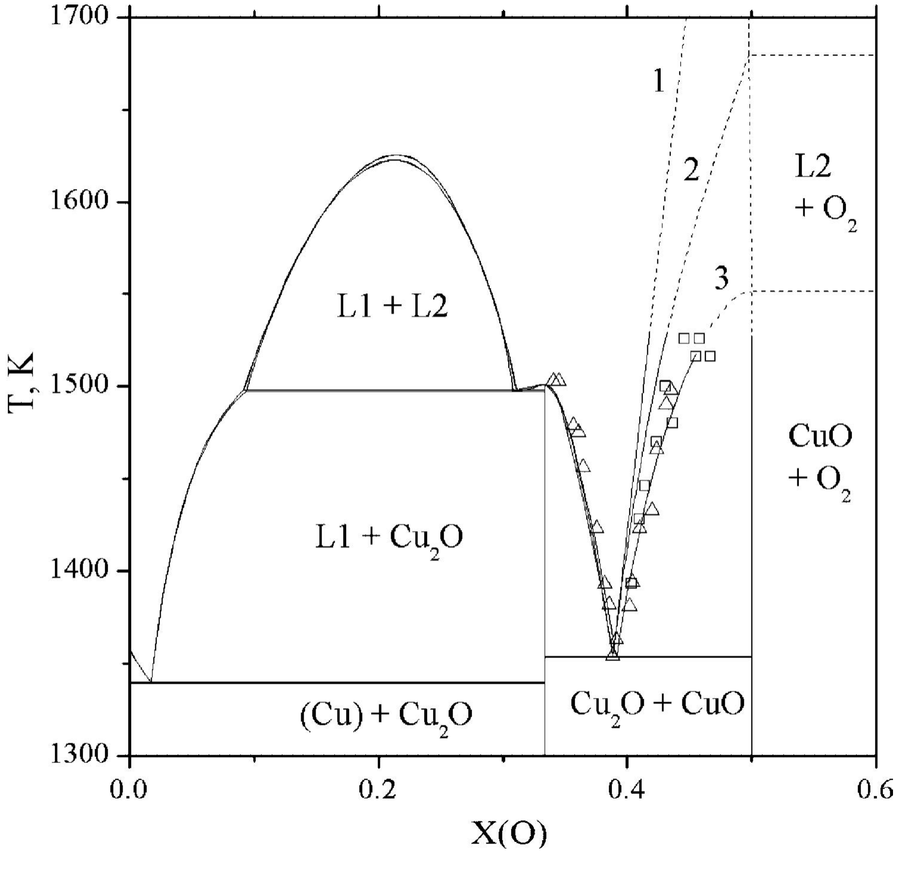

Fig. 1- 13 A calculated Cu-O phase diagram. The X axis denotes the content of oxygen [56].

The relationship between a material's structure and its properties remains a central focus of research, as elucidating this connection enables the prediction of material performance based on microstructural characterization. However, studies on microstructure evolution in cold-sprayed materials are still limited. To address this, advanced electron microscopy techniques were employed to characterize the as-sprayed Cu–0.2O alloy in detail. Complementary numerical simulations were performed to analyze strain and temperature distributions within particles and their evolution during spraying. Together, these approaches systematically investigate the origin, distribution, and strengthening role of Cu_2O precipitates, as well as their influence on maintaining thermal and electrical conductivity. This work aims to deepen the understanding of microstructure-property relationships in cold-sprayed Cu and Cu-based materials, providing a foundation for future research.

1.3.2. Lacking research on high-strength Cu alloys by CSAM

Although Cu exhibits excellent ductility, its strength remains insufficient for many demanding applications. High-strength Cu alloys are increasingly sought after in fields such as robotics, electronics, and the automotive industry [59-61], where components must endure prolonged loading with adequate strength and toughness. Designing Cu-based alloys with tailored mechanical properties is therefore critical. Among these alloys, bronze—primarily composed of Cu and Sn—stands out as an ideal candidate to meet industrial requirements. Thanks to its superior strength, wear resistance, and corrosion resistance [62-64], bronze is widely used in manufacturing bearings, springs, marine equipment, and electronic components [65-67]. Despite their advantages, traditionally manufactured Cu-Sn alloys exhibit drawbacks such as large grain sizes, shrinkage cavities, and grain boundary segregation of the hard and brittle δ phase, which significantly reduce hardness and strength and limit their applications [68]. With the increasing industrial demand for bronze components that exhibit superior performance and complex geometries, innovative fabrication strategies are required to address these challenges and achieve the desired mechanical properties [69, 70]. Current approaches primarily focus on enhancing cooling rates, promoting grain refinement, and incorporating alloying additions to suppress δ phase segregation. CSAM offers a promising solution, as its ultra-high strain rates facilitate rapid cooling, effectively inhibiting phase segregation. Furthermore, the unique bimodal microstructure formed during CSAM deposition induces significant grain refinement, thereby enhancing mechanical performance. However, research to date has largely centered on cold-sprayed bronze coatings for wear resistance, with limited exploration of CSAM for bulk Cu-Sn alloys with superior mechanical properties. Additionally, there still lacks a systematic study on the microstructural evolution underlying their enhanced properties. To fill this gap, we fabricated Cu-Sn alloys with 5 wt.% and 10 wt.% Sn (Cu-5Sn and Cu-10Sn) via CSAM, achieving superior compressive properties compared to conventional Cu-Sn materials. Using advanced electron microscopy, we analyzed the microstructural differences between Cu-5Sn and Cu-10Sn and their corresponding mechanical behaviors. Our study aims to advance the fabrication of high-strength Cu-Sn alloys by CSAM and clarify how microstructural evolution influences their properties, promoting broader industrial applications.

Chapter 2 Methodology

2.1. Materials fabrication

In Chapter 3, oxygen-bearing Cu powders (99.7 wt.% purity, containing 0.2 wt.% oxygen) were synthesized via gas atomization in an oxygen-rich environment (the oxygen content is kept at 2000 ppm) and subsequently employed as the feedstock for depositing the Cu-0.2O sample. In contrast, high-purity Cu powders (99.9 wt.% purity) were used to produce the pure Cu sample. The elemental compositions of the Cu-0.2O and pure Cu feedstock powders are presented in **Table 2-1**. Both powder variants exhibit a predominantly spherical morphology, with particle sizes ranging from 15 to 53 μm, as illustrated in **Fig. 2-1(a)** to **(c)**. Here, the particle size was measured by a laser particle analyzer (Malvern Mastersizer 3000) based on the powder weight of approximately 20 g. The two powder samples were deposited onto a sandblasted Al7075 substrate using a JHL CS-600 spraying system. The schematic diagram of JHL CS-600 is shown in **Fig. 2-2**. The system utilizes a preheating device to warm the driving gas, which carries and accelerates the feedstock powders as they pass through the nozzle, where they are further accelerated. Subsequently, the powders impact the substrate at supersonic velocities, resulting in the formation of a dense deposition. To prevent powder blockages caused by heat accumulation at the spray gun, a water-cooling device is employed to dissipate excess heat. During the spraying process, high-pressure nitrogen gas serves as both the driving and powder carrier gas. To investigate the performance and microstructure of cold-sprayed Cu-0.2O samples under varying spraying parameters and to identify the optimal conditions, five groups of samples were prepared with different gas temperatures and pressures. The specific parameters for each group are detailed in **Table 2-2**. The stand-off distance between the nozzle exits and the top surface of the substrate was set at 25 mm, the powder feed rate was 100 g/min, and the powders were axially fed into the nozzle with a transverse speed of 100 mm/s. The thickness of each layer of deposition was set as 400 μm. The thickness was determined by pre-spraying (repeated spraying with varying thickness to optimize the appropriate thickness with desired relative density), and it was controlled via adjusting the powder feeding rate, transverse speed, and spraying pressure. The spray gun was operated in an “S”-shaped pattern, as illustrated in **Fig. 2-3**, to enhance deposition efficiency and coating quality. Before spraying, the Al7075 substrate was sandblasted to improve the adhesion of the feedstock powders. The dimensions of the deposition were 50 mm × 50 mm × 5 mm.

In Chapter 4, pre-alloyed Cu-5Sn and Cu-10Sn powders were employed as the feedstock for the fabrication of Cu-5Sn and Cu-10Sn deposition. The chemical composition of Cu-5Sn and Cu-10Sn powders was demonstrated in **Table 2-3**. The morphology of Cu-5Sn and Cu-10Sn powders, together with their powder size distribution, was shown in **Fig. 2-4**. The sphericity of both the Cu-5Sn and Cu-10Sn powders is relatively lower compared to that of Cu powders, which may lead to lower interfacial bonding upon deposition. The gas pressure and temperature for Cu-5Sn and Cu-10Sn were set at 3.4 MPa and 700 ℃ after the optimization of processing parameters in Chapter 3. The thickness of each layer of deposition was set at 250 μm because the formability of Cu-Sn alloys is lower than that of Cu. Lower thickness of a single layer enables higher deposition efficiency. The stand-off distance between the exit of the nozzle and the substrate was set at 25 mm, the feeding rate of feedstock powders was 100 g/min, and the powders were axially fed into the nozzle with a transverse speed of 100 mm/s. The spray gun also moved following an “S” shape, and the Al7075 substrate was sandblasted before spraying to achieve better adhesion of feedstock powders. The dimensions of the deposition were 50 mm × 50 mm × 4 mm.

Table 2-1. Chemical composition of the feedstock Cu powders.

Element(wt.%)	Cu	O	As	Sb	Fe	Pb	Bi
Pure Cu	Bal.	0.05	0.002	0.002	0.005	0.005	0.001
Cu-0.2O	Bal.	0.20	0.0023	0.01	0.02	0.0048	0.002

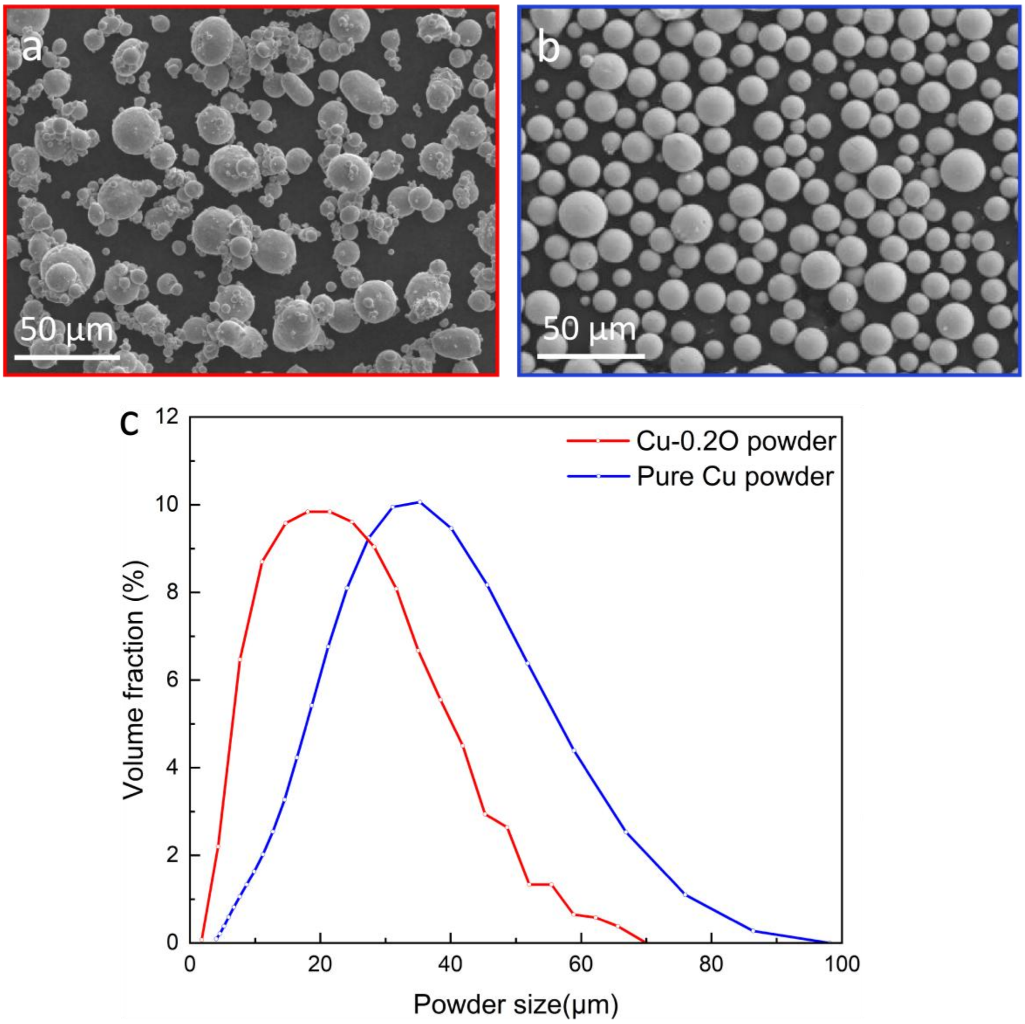

Fig. 2- 1 Morphology of commercial gas atomized Cu powders. (a) The morphology of Cu-0.2O powders. (b) The morphology of pure Cu powders. (c) Corresponding powder size distribution.

Table 2-2. Cold-sprayed Cu-0.2O samples with different spraying parameters

Sample	Gas pressure/MPa	Gas temperature/°C
3.4-500	3.4	500
3.4-600	3.4	600
3.4-700	3.4	700
3-700	3	700
2.6-700	2.6	700

Fig. 2- 2 Schematic diagram of JHL CS-600 spraying system, with different components marked.

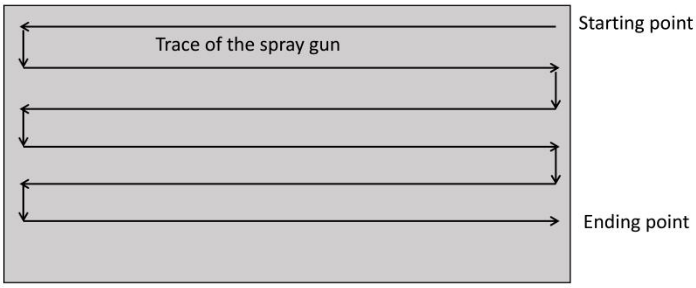

Fig. 2- 3 Schematic diagram of the "S" shape that the spray gun moves during the spraying process.

Table 2-3. Chemical composition of Cu-5Sn and Cu-10Sn powders

Element(wt.%)	Cu	Sn	Zn	Si	Fe	Pb	Bi
Cu-5Sn	Bal.	5.48	0.008	0.0053	0.0032		
Cu-10Sn	Bal.	~10	≤0.002	≤0.02	≤0.03	≤0.02	≤0.03

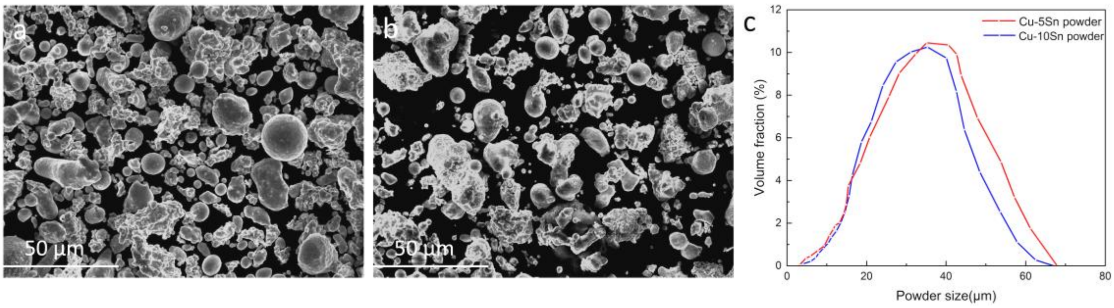

Fig. 2-4 Morphology of pre-alloyed Cu-5Sn and Cu-10Sn powders. (a) The morphology of Cu-5Sn powders. (b) The morphology of Cu-10Sn powders. (c) Corresponding powder size distribution.

2.2. Microstructure characterization techniques

2.2.1. Introduction to electron microscopy

The concept of imaging objects smaller than visible light began in 1925 when French physicist de Broglie [71] proposed that microscopic particles exhibit both particle and wave-like properties. Building on this, accelerated electrons—due to their shorter wavelength compared to visible light—became a theoretical basis for electron microscopy. Subsequently, German physicist Busch [72] suggested using magnetic coils as lenses to focus electron beams. Advancing this idea, Knoll and Ruska constructed the first transmission electron microscope (TEM) in 1932, replacing light with electron beams for imaging [73]. Although its resolution was low (~12×) due to a maximum accelerating voltage of 70 kV, this marked a significant breakthrough. In 1933, Ruska further developed a TEM capable of 10,000× magnification [74], demonstrating the potential of electron beams to achieve much higher image resolution.

The concept of scanning electron microscopy (SEM) was introduced around the same time [75]; however, due to the requirement for a highly focused scanning electron beam and detection of secondary electrons emitted from the sample, commercial SEM systems were not developed until 1965. With ongoing technological advancements, SEM resolution has improved rapidly. Today, electron microscopy is an essential tool in microscopic characterization and forms the foundation of most materials research and development. **Fig. 2-5** illustrates various types of electron emissions that occur when the electron beam interacts with a sample. During imaging, electrons interact with the sample variably. Electrons emitted in directions opposite to the incident beam include backscattered electrons, secondary electrons generated by the sample, characteristic X-rays, and Auger electrons. In the direction of the incident beam, electrons may be unscattered (projected electrons), inelastically scattered (transferring energy to the sample), or elastically scattered (mechanically deflected).

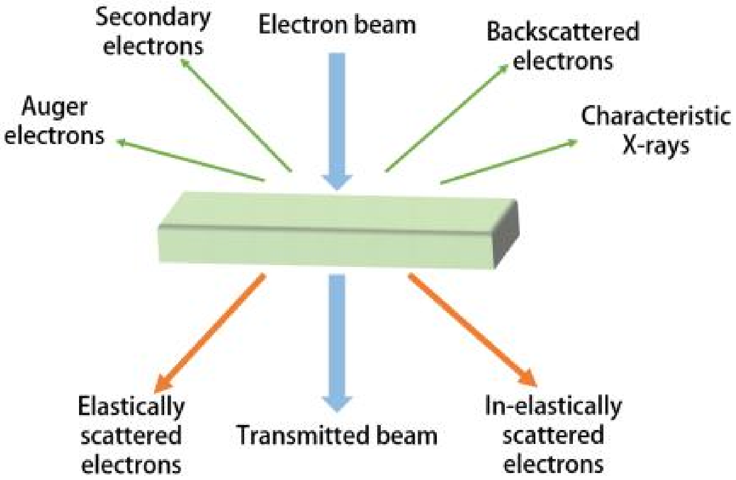

Fig. 2- 5 Different electrons after the electron beam interacted with a specimen.

2.2.2. Scanning electron microscopy

Scanning electron microscopy (SEM) primarily detects backscattered electrons and secondary electrons emitted from the sample upon irradiation by an electron beam. This technique is widely used to characterize the surface morphology and crystal structure of materials at the microscale. A schematic of a typical SEM setup is shown in **Fig. 2-6**. Electrons are generated from a filament and accelerated by an electric field. These electrons are focused on a beam spot by a series of magnetic lenses and directed onto the sample surface. The primary imaging signal comes from secondary electrons, which are low-energy electrons emitted from the sample's conduction band due to beam bombardment. Due to their very low energy, secondary electrons require an additional bias voltage applied by the detector to accelerate and efficiently collect them. This enables high-resolution surface imaging.

Electron backscatter diffraction (EBSD) is an SEM-based technique used to characterize the crystalline structure of materials [76]. **Fig. 2-7** shows a schematic of a typical EBSD setup. The process is performed within an SEM equipped with an EBSD detector, which includes a compact lens, a phosphorescent screen, and a low-light camera. During analysis, the electron beam is tilted at a 70° angle to the specimen surface. Backscattered electrons emerge from the sample and elastically diffract after interacting with the atomic lattice, losing some energy in the process. These electrons exit at various angles and strike the phosphor screen, forming Kikuchi patterns (EBSPs). The spatial resolution of EBSD depends on factors such as sample material and surface flatness; smoother surfaces improve pattern quality and detection efficiency. The indexed patterns provide detailed information on phases, grain boundaries, crystallographic orientations, and more, making EBSD a powerful tool for materials characterization.

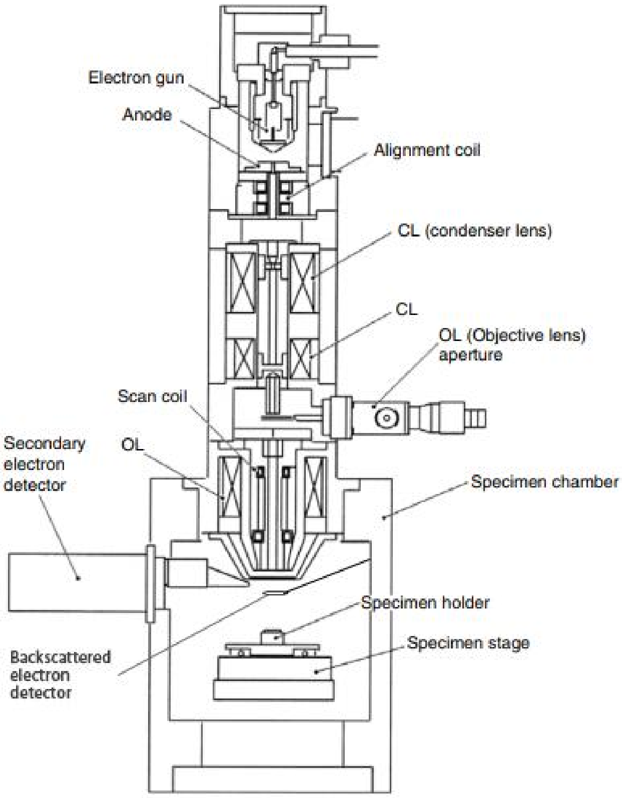

Fig. 2- 6 Schematic diagram of a typical SEM instrument [77].

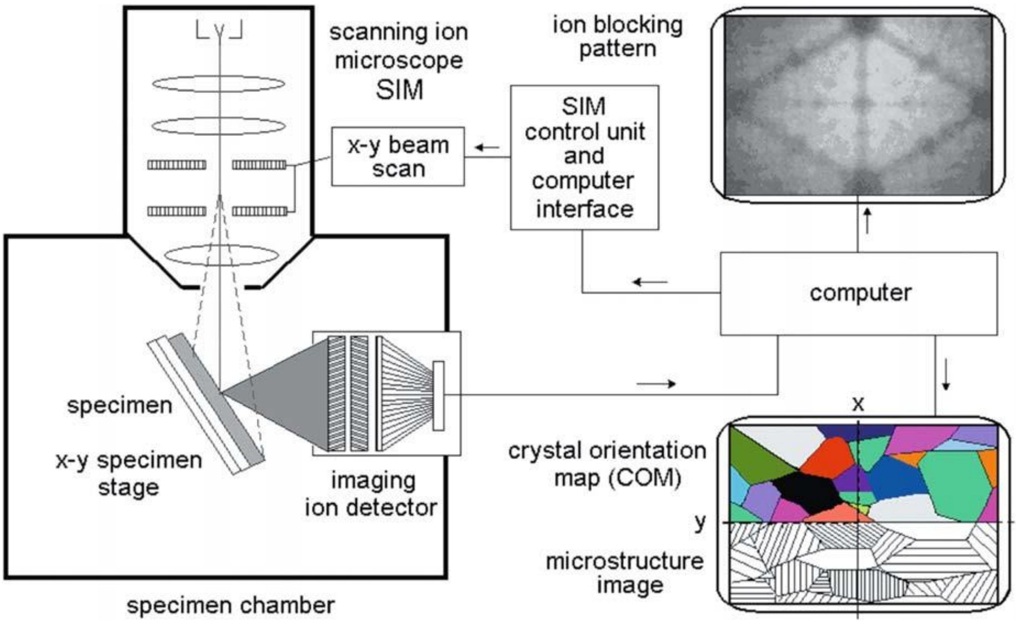

Fig. 2- 7 Working principle of EBSD [78].

2.2.3. Transmission electron microscopy

The working principle of transmission electron microscopy (TEM) is illustrated in **Fig. 2-8.** Electrons are emitted from an electron gun and accelerated by a high voltage. These electrons are then focused into a parallel beam or a convergent spot by two condenser lenses and directed onto the sample. The electrons that pass through the sample are magnified by intermediate lenses and projected onto a fluorescent screen or camera via a projection lens. By adjusting the focal length of the intermediate lens, either the diffraction pattern (DP) from the interaction between electrons and the sample's lattice (**Fig. 2-8(a)**) or a magnified image of the sample morphology (**Fig. 2-8(b)**) can be obtained. The diffraction pattern follows Bragg's law, providing detailed crystallographic information from the irradiated area, making TEM a crucial tool in crystallographic research. Since the electron beam must be transmitted through the sample, an accelerating voltage of 200 kV or higher is required. Additionally, the thickness of TEM samples should be less than 100 nm to ensure optimal imaging quality.

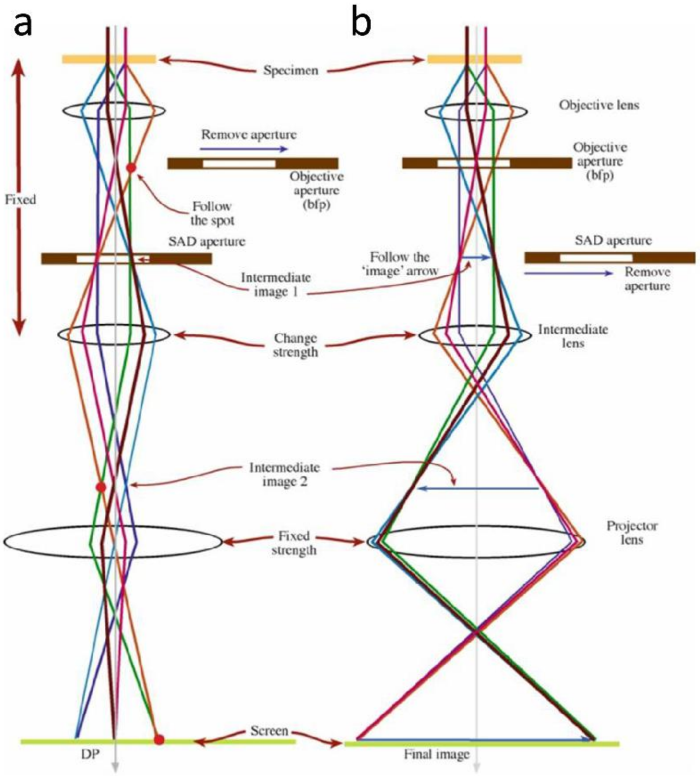

Fig. 2-8 Schematic diagram of the imaging principles of TEM [79]. (a) Diffraction mode (b) Image mode.

2.2.4. Scanning transmission electron microscopy

Scanning transmission electron microscopy (STEM) combines the capabilities of SEM and TEM to achieve elemental and electronic structure analysis at ultra-high resolution [80]. Unlike conventional SEM, scanning transmission electron microscopy (STEM) operates at higher accelerating voltages, typically ranging from 80 kV to 200 kV. This increase in accelerating voltage reduces the electron wavelength, thereby enhancing spatial resolution. The schematic of an aberration-corrected STEM is shown in **Fig. 2-9**. Electrons generated by the electron gun are focused on the specimen by the condenser and objective lenses. The electron beam scans the sample via scan coils, with the maximum scan angle limited by an objective aperture. Multiple detectors collect various signals to generate complementary STEM images. The annular dark-field detector blocks the transmitted beam while collecting scattered electrons to produce dark-field images [81]. By adjusting the inner angle of the dark-field detector with post-specimen lenses, image contrast is enhanced. High-angle scattered electrons collected by this detector produce high-angle annular dark-field (HAADF) images. These images capture elastically scattered electrons that retain their energy, providing information primarily on atomic position and mass. Assuming a uniform nanoscale sample thickness, atoms with higher atomic numbers appear brighter in HAADF images due to stronger scattering [82].

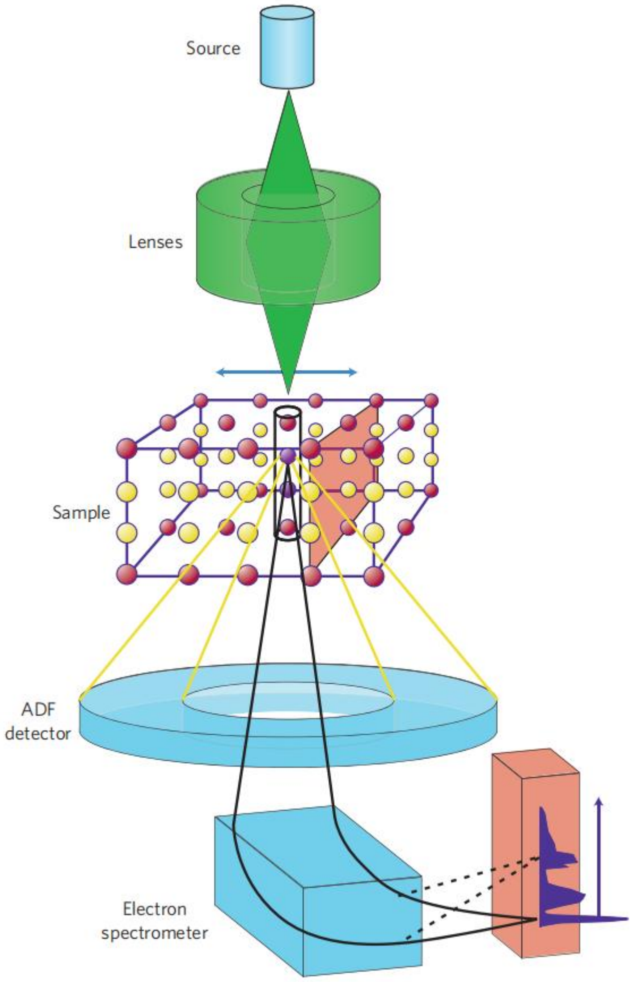

Fig. 2- 9 Working principles of a STEM [83].

2.3. Sample preparation for microstructure characterization

2.3.1. OM and SEM sample preparation and characterization

The as-sprayed samples were separated from the substrate and sectioned using an electrical wire cutting machine into dimensions of 5 mm × 5 mm × 1 mm, as illustrated in **Fig. 2-10**. Specimens were then embedded in epoxy resin with a diameter of 25 mm and mechanically ground and polished using a Struers Tegramin-25 automated polishing system. The preparation process involved sequential grinding with 28 μm silicon carbide paper, followed by polishing with diamond suspensions of 15 μm, 9 μm, 3 μm, and 1 μm for 5, 3, 2, and 5 minutes, respectively. This produced a bright, mirror-like surface with minimal visible scratches. Cross-sectional morphology was examined using a ZEISS Axiolab 5 optical microscope (OM), with porosity quantitatively analyzed via Image Pro Plus software based on five OM images per sample.

For SEM analysis, samples underwent electrolytic polishing after mechanical grinding using a DC power supply at 6 V for 30 seconds with a custom solution of deionized water, ethanol, phosphoric acid, isopropanol, and urea. Specimens were then rinsed with deionized water and ethanol and stored in a vacuum chamber to prevent oxidation. EBSD specimens, after mechanical preparation, were further polished using a Precision Etching and Coating System (PECS II, Gatan) with Ar ion milling at 4 keV and a 4° angle for one hour. Following ion polishing, the samples were ready for SEM observation.

Grain size distribution and geometrically necessary dislocations (GND) were analyzed using backscattered electron (BSE) imaging and EBSD on a Thermo Fisher Apreo 2 SEM operated at 20 kV, with an EBSD step size of 0.08 μm. Oxford AztecCrystal was employed for the calculation of area-weighted average grain size. Here, the average grain size was measured based on approximately 1300 grains measured for each field of view. Five figures for each specimen were photographed to eliminate accidental error. The equivalent circle diameter (μm) was chosen for the measurement of irregular grains. The GND analysis was operated using the module in Oxford AztecCrystal based on the Kernel Average Misorientation (KAM) value of each grain, and the average GND density was measured based on the mean value of five figures with a magnification of 15000 × to eliminate the accidental error. The detailed algorithm regarding the calculation of GND can be found in Pantleon's work in 2008 [84]. The recrystallization fractions of as-sprayed Cu-0.2O and pure Cu were determined using Channel 5 software.

2.3.2. TEM sample preparation and characterization

For TEM analysis, the samples were initially cut using a wire-cut electrical discharge machine to dimensions of 5 mm × 6 mm × 0.3 mm. It was then mechanically ground to approximately 30 μm in thickness using silicon carbide paper of 28 μm, 10 μm, 5 μm, and 1.5 μm, respectively. Then a disk with a diameter of 3 mm was prepared by a special puncher. After that, this disk was fixed and thinned by a Gatan 695 Precision Ion Polishing System (PIPS). Dual-beam mode was used with one gun located at the top of the surface and the other at the bottom. First, the Argon ion energy was set to 6 keV, and the angle between the gun and the sample surface was set to 6 degrees. It was approximately one hour until a tiny aperture appeared at the center of the sample. Then set the Argon ion energy to 4 keV and the inclination angle to four degrees to broaden this tiny aperture, which lasted for approximately twenty minutes. Finally, an Argon ion energy of 2 keV and an inclination angle of 2 degrees were used for cleaning the sample surface, with a duration of one hour. The sample was then taken out for observation under TEM.

TEM observations of the as-sprayed Cu-0.2O sample were conducted using a JEOL 2100F operated at 200 kV to examine its morphology. Selected area electron diffraction (SAED) was performed in corresponding regions to analyze the phase structure of the nanoscale precipitates. Additionally, high-resolution TEM (HRTEM), high-angle annular dark-field scanning transmission electron microscopy (HAADF-STEM), and energy-dispersive X-ray spectroscopy (EDS) mapping were carried out using a Thermo Scientific Spectra 300 microscope at an accelerating voltage of 300 kV.

2.4. Mechanical properties test

Vickers microhardness measurements were performed on the cold-sprayed Cu samples using a digital microhardness tester (Struers Duramin-40). The instrument employs a pyramidal diamond indenter (136° apex angle) to imprint the material surface under a controlled load. The resulting indentation dimensions were measured via an integrated optical system to calculate the Vickers hardness value. Testing parameters included a 200 g load and a 10 s dwell time. To ensure statistical reliability, 20 measurements were taken in a grid pattern (5 × 4 array) across the sample cross-section, maintaining a 0.5 mm spacing between adjacent indentations. Reported hardness values represent the average of these measurements.

An Instron 68TM-50 universal testing system was employed for the room-temperature compression tests. Cylindrical specimens (2 mm radius × 6 mm height) were extracted perpendicular to the cold spray deposition direction. The schematic diagram of the compressive sampling is shown in **Fig. 2-10(b)**. Uniaxial compression was applied at a constant strain rate of 10^{-3} s^{-1} to evaluate the mechanical response of the as-sprayed samples.

2.5. Thermal/electrical conductivity evaluation

The evaluation of thermal conductivity of the as-sprayed Cu-0.2O and pure Cu was conducted by a laser thermal conductivity meter according to the following formulas:

$$K = DC_{\rho} \cdot \rho \qquad (1)$$

$$D = W_{1/2} L^2 / (\pi^2 \cdot t_{1/2}) \qquad (2)$$

Where K is the thermal conductivity (W/(m·K)), C_{ρ} is specific heat (J/(kg·K)), D is the thermal diffusion coefficient (m^2/s), ρ is the density, $W_{1/2}$ is the parameter for simplification, L is sample thickness (m) and $t_{1/2}$ is the half of the time (s) when the sample reach the peak temperature. Disk-like specimens were used for thermal conductivity tests. The diameter of the samples was 12.7 mm, and the thickness was 2 mm, respectively. The schematic diagram of the thermal conductivity test specimen is shown in **Fig. 2-10(c)**. The thermal conductivity of each sample was evaluated based on the average results of three repeated tests.

The electrical conductivity measurement of the as-sprayed Cu-0.2O and pure Cu was conducted using a QJ36S digital DC tester with a four-point probe approach employed. This technique utilizes four equally spaced probes (8 mm inter-probe distance) to simultaneously measure voltage and current, enabling precise determination of resistivity and subsequent calculation of conductivity. Rectangular specimens (30 mm × 1 mm × 2 mm) were oriented with their longitudinal axis perpendicular to the spray deposition direction. The dimensions of the electrical conductivity specimen were depicted in **Fig. 2-10(d)**. Conductivity values were derived from the average of three distinct measurement regions per sample.

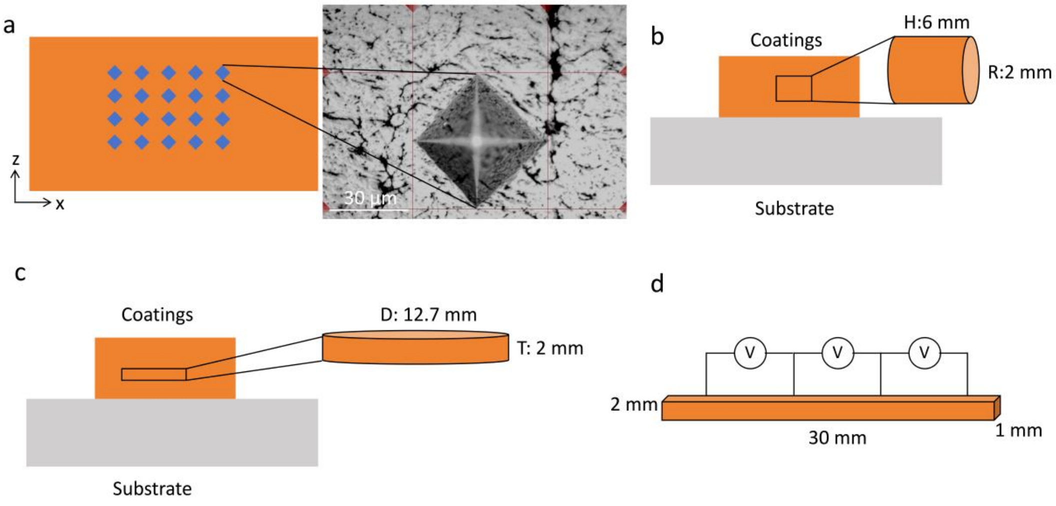

Fig. 2-10 The schematic diagram of the sampling and their corresponding dimensions. (a) Schematic diagram of the microhardness test and an OM image show the measurement procedure. (b) Sampling of the compressive test cylinder and its dimensions. (c) Sampling of the thermal conductivity test and dimensions of the disk. (d) Sampling of the electrical conductivity rectangular specimen and its dimensions.

2.6. FEM simulation

The cold spray process involves the impact of particles at supersonic velocities onto a substrate, a phenomenon that can be characterized as a nonlinear, dynamic contact problem. Due to the extremely brief duration of particle deposition, experimental investigation of the thermodynamic phenomena occurring during this process is challenging. Consequently, numerical simulation has become a widely adopted approach for elucidating thermodynamic behavior associated with particle-substrate interactions. In cold spray applications, where high-velocity impacts and significant plastic deformation are prevalent, the finite element method (FEM) has proven effective in simulating these phenomena [85-89].

Several numerical methods have been developed for modeling the cold spray process, each with distinct characteristics. The first is the Lagrangian numerical method, which describes object movement as functions of the coordinates and time associated with specific materials. This approach is particularly well-suited for representing solids as structured entities, as the nodes of the Lagrangian mesh move in concert with the material, allowing for precise definition and tracking of interfaces between different components [90-92].

The second method is the Arbitrary Lagrangian – Eulerian (ALE) approach, which integrates aspects of both pure Lagrangian and Eulerian analyses. The ALE method continuously redefines the computational grid in arbitrary or predefined ways throughout the simulation, making it applicable to both solids and fluids. By permitting the mesh to move independently of the material, the ALE approach maintains high mesh quality during the entire simulation [85-88, 93].

The third method is Smoothed Particle Hydrodynamics (SPH), an effective technique for solving continuum dynamic problems [90, 94-96]. In SPH, the domain is represented by discrete, unconnected particles, each possessing unique material properties. The physical parameters of each particle are computed based on the data from neighboring particles, making SPH particularly useful for simulating high-velocity impact phenomena such as those encountered in cold spray deposition.

The Coupled Eulerian-Lagrangian (CEL) approach is employed when Eulerian materials interact with Lagrangian elements via Eulerian-Lagrangian contact [92, 97]. In this method, the Eulerian volume fraction of a given material within each element is calculated to track its flow through the mesh. An element fully occupied by a material is assigned to a volume fraction of one, while an empty element is assigned to zero. By defining different element types, both thermal and dynamic effects can be incorporated. Compared to the aforementioned simulation approaches, the CEL method can address more complex interaction problems, including severe plastic deformation accompanied by ultra-high strains. Therefore, the CEL method has been selected for the simulations conducted in this study.

The temperature evolution during particle deposition was systematically investigated through FEM conducted by Abaqus/Explicit (version 6.14.4). The CEL approach was selected for this simulation due to its well-established accuracy and robustness in modeling impact phenomena. The simulation configuration, illustrated in **Fig. 2-11**, modeled the impact of a single 40 μm diameter Cu particle onto an Al substrate at an initial velocity of 600 m/s, with particular focus on analyzing the resulting temperature distribution and plastic strain evolution in both the particle and substrate. The simulation framework incorporated three key components: a Lagrangian Cu particle, an Al substrate, and a confining Eulerian domain designed to prevent particle outflow during the impact process. Material behavior was characterized using the Mie-Grüneisen equation of state as well as the Johnson-Cook model [98] for elastic response and strain hardening effects. The corresponding model is expressed as the formula below:

$$\sigma = [A + B\varepsilon^n][1 + C\ln\varepsilon^*][1 - T^{*m}] \tag{3}$$

Here, ε represents the equivalent plastic strain; $\varepsilon^* = \varepsilon_1/\varepsilon_0$ signifies the strain rate, and ε_0 is set to be 1.0 s^{-1}; $T^* = (T-T_0)/(T_m-T_0)$ denotes the temperature; n represents the exponent of work hardening effect; A, B and m are material-dependent constants; T is the temperature in Kelvin; T_m refers to the melting point of the materials and T_0 is the temperature for reference. The material parameters used in the simulation are listed in **Table 2**. The total simulation time was set to 50 ns, which was sufficient to capture the complete impact and deformation process. A general contact algorithm was applied with a friction coefficient of 0.3. Additionally, the efficiency of kinetic energy of the particle transferred to heat energy was set at 90% considering the energy loss. For meshing, a refined element size of 1.5 μm was used for the particle and Eulerian domain to ensure accuracy, while a coarser 3 μm mesh was applied to the substrate. The initial temperature of the environment, the Cu powder, and the Al substrate were set to 298 K. The C3D8RT element type was selected for both the particle and substrate, whereas the EC3D8RT element, which accounts for thermal effects, was used for the Eulerian domain.

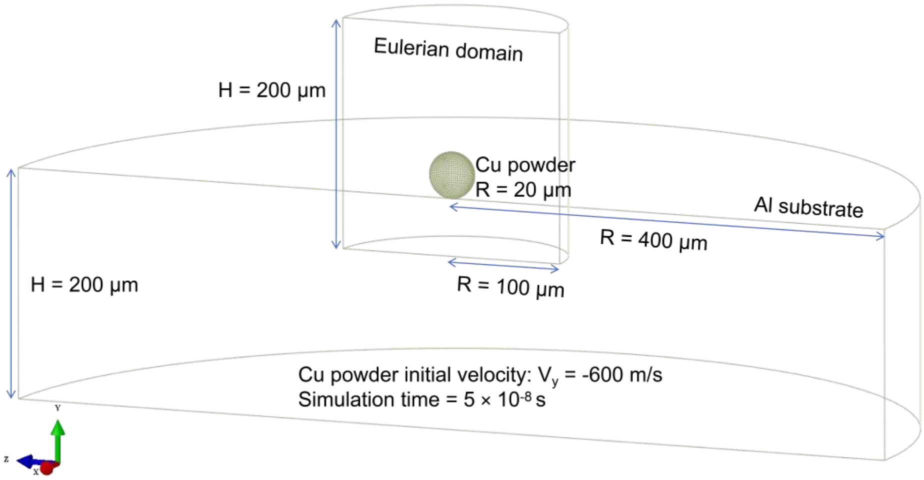

Fig. 2- 11 Schematic diagram of the CEL simulation with the view cut of the YZ plane. The Cu powder is located in the inner region of the Eulerian, and the initial distance between the bottom of the Cu powder and the top surface of the Al substrate is set to 0.

Table 2-4. The parameters of the material properties used in the simulation [22, 88, 95, 99].

Properties (unit)	Cu powder	Al substrate
Density ρ (kg/m^3)	8900	2700
Shear modulus G (GPa)	44.7	27
Thermal conductivity λ (W/m·K)	385	237.2
Specific heat c (J/kg·K)	383	898.2
Sound velocity c_0 (m/s)	3940	5386
Slope of U_s with U_p s	1.489	1.339
Grüneisen coefficient Γ_0	2.02	1.97
Yield stress A (MPa)	90	148.4
Hardening constant B (MPa)	292	345.5
Hardening exponent n	0.31	0.183
Strain rate constant C	0.025	0.001
Thermal softening exponent m	1.09	0.895
Melting point T_m (K)	1356	916
Reference temperature T_0 (K)	298	293
Johnson-Cook damage d_1, d_2, d_3, d_4, d_5	0.54, 4.89, 3.03, 0.014, 1.12	0.071, 1.248, 1.142, 0.147, 1

Chapter 3 Enhancing strength and thermal/electrical conductivity of cold sprayed copper via inducing Cu_2O precipitates

3.1. Introduction

Cold spray is a solid-state material deposition process that has been widely adopted across various industries for the cost-effective repair of high-value Cu and Cu-based failed components [100, 101]. Unlike conventional methods such as thermal spraying, plasma spraying, and laser melting deposition—which involve high temperatures harmful to temperature-sensitive Cu—cold spray avoids fusion and phase changes, preserving the original properties of feedstock powders [12-14, 17]. This technique offers advantages, including maintained high thermal conductivity, shorter manufacturing times, greater flexibility, and minimal material waste. However, despite its cost efficiency and retention of excellent electrical and thermal conductivity, cold-sprayed Cu deposits often suffer from insufficient mechanical properties, with microhardness typically below 100 HV and compressive strength under 400 MPa. As these Cu components frequently operate in high-temperature environments where thermal softening gradually reduces strength, their low hardness and strength limit their long-term durability and application potential.

To address the inherent limitations in the mechanical properties of cold-sprayed copper (Cu) components, considerable research has been devoted to enhancing their microhardness and strength, predominantly through precipitates and secondary-phase strengthening mechanisms. As previously discussed in Chapter 1, the incorporation of ceramic reinforcements or intermetallic phases within the Cu matrix has proven effective in impeding dislocation motion, thereby augmenting mechanical strength. However, these ceramic reinforcements and intermetallic compounds significantly degrade thermal and electrical conductivity by acting as barriers to heat and electron transfer. For example, the thermal conductivity of such composites typically remains below 250 W/m·K [43, 102-104], far lower than that of pure cast Cu (390 W/m·K). Similarly, their electrical conductivity rarely exceeds 35 MS/m [53, 105, 106], which is only about 60% of that of pure Cu. This inherent trade-off between mechanical strength and conductivity significantly limits the wider application of cold-sprayed Cu-based materials. Therefore, novel strategies are urgently needed to overcome this challenge.

To improve strength and hardness while slightly sacrificing conductivity, selecting an optimal secondary phase is critical. Recent studies have shown that oxygen in Cu and Cu alloys can act as an effective strengthening agent, owing to its extremely low solubility in Cu [107] (≈ 0.008% at 1070°C), which promotes the formation of precipitates rather than solid solutions. Researchers have explored Cu-O alloys through compositional design, microstructure optimization, and post-processing to balance strength and conductivity. For instance, Liu et al. [57] fabricated Cu-0.3O and Cu-0.6O alloys via laser powder bed fusion (LPBF), achieving a tensile strength of 491.6 MPa with 68 % IACS conductivity, while Gu et al. [58] introduced 0.93 wt.% oxygen into a Cu matrix via laser remelting, enhancing relative density and attaining a tensile strength of 405 MPa with 74 % IACS conductivity. However, these efforts centered on laser-based additive manufacturing, leaving cold-sprayed Cu-O alloys underexplored, and the strengthening mechanisms, as well as the influence of oxygen on conductivity, remain poorly understood.

In this study, Cu powders were intentionally oxidized via an oxygen-assisted gas atomization process before cold spraying. This approach generated nanoscale Cu_2O precipitates dispersed along Cu grain boundaries, resulting in a microhardness and compressive strength significantly higher than those of pure cold-sprayed Cu, while maintaining exceptional thermal and electrical conductivity compared with Cu-based composites. The distribution, strengthening mechanisms, and conductivity effects of Cu_2O precipitates were systematically investigated using advanced electron microscopy and finite element method simulations. This work presents a novel strategy for designing high-performance Cu alloys via nanoscale precipitate engineering, with promising potential for industrial applications.

3.2. Processing parameter optimization

Two main driving factors affect the deposition of Cu powders: gas temperature (T) and gas pressure (P), respectively. As shown in **Fig. 3-1**, numerical simulations by Yin et al. [108] indicate that the simulated velocity of the powders tends to increase with increasing spraying temperature and pressure. Gas pressure directly influences the velocity of feedstock powders [108]. There is always a threshold velocity for successful deposition on the substrate, which varies for different materials, called the critical velocity (Vc) [109]. Only when the velocity of the powders exceeds Vc can they form a deposit instead of rebounding. Consequently, higher gas pressure enables the powders to form a deposit on the substrate more effectively, thereby enhancing the deposition efficiency (DE), defined as the ratio of the powder mass deposited on the substrate to the total feedstock mass. Higher DE enhances the bonding strength of Cu deposition and reduces material waste.

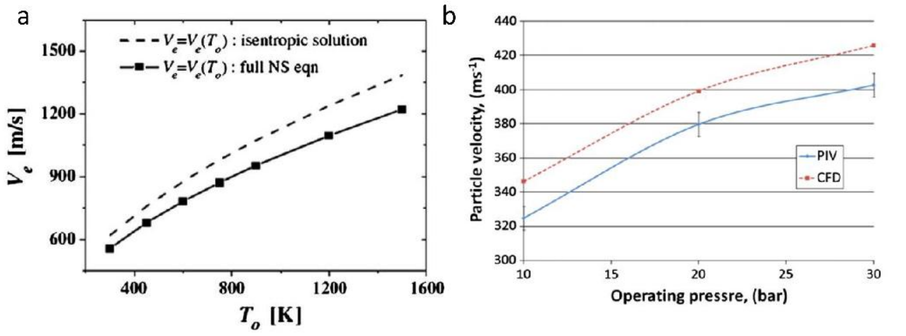

Fig. 3- 1 Influence of (a) gas temperature and (b) gas pressure on the velocity by simulation [30].

Gas temperature also plays a crucial role in promoting powder deformation. Higher gas temperatures preheat the powders before impact, inducing thermal softening that facilitates more severe plastic deformation. Additionally, elevated temperatures generate more metal jetting upon impact, which enhances adiabatic shear instability (ASI) at the interface between particles and substrate, aiding the formation of strong metallurgical bonds. The relative density, mechanical properties, and thermal/electrical conductivity of the cold-sprayed Cu-0.2O samples will be detailed in the following sections, alongside the effects of gas temperature and pressure on performance and microstructure evolution.

3.2.1. Influence of the spraying parameters on formability

Fig. 3-2 presents optical images of the cross-sectional microstructure of cold-sprayed Cu-0.2O samples deposited under varying gas pressures. At a relatively low gas pressure of 2.6 MPa, internal defects such as pores and cracks are evident, primarily due to insufficient interfacial bonding. Increasing the gas pressure from 2.6 MPa to 3 MPa raises the particle impact velocity, promoting a transition from mere mechanical interlocking to metallurgical bonding. This results in higher compactness and fewer defects. When the gas pressure reaches its peak value of 3.4 MPa, the particle impact velocity is maximized, further enhancing metallurgical bonding between adjacent particles and achieving the highest compactness; consequently, the 3.4-700 sample (fabricated with a gas pressure of 3.4 MPa and gas temperature of 700 ℃) shows no large pores or bonding cracks in its cross-sectional microstructure.

A similar trend is observed with increasing gas temperature, as illustrated in **Fig. 3-3.** The 3.4-500 sample (fabricated with a gas pressure of 3.4 MPa and a gas temperature of 500 ℃, as illustrated in **Table 2-2**) exhibits numerous micropores and weak bond interfaces, indicating that low spraying temperature and insufficient powder preheating hinder intimate particle contact. As the temperature rises from 500 °C to 700 °C, thermal softening facilitates more severe deformation upon impact, resulting in the relative density of the as-sprayed samples increasing significantly from 97.5 % to 99.2 %, demonstrating a clear densification effect.

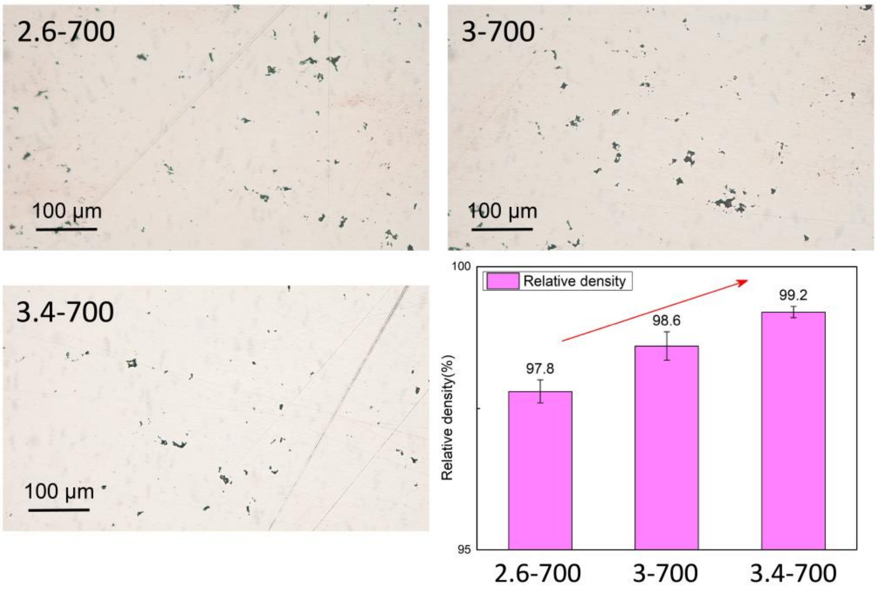

Fig. 3- 2 Relative density evolution with increasing gas pressure and corresponding cross-sectional microstructure.

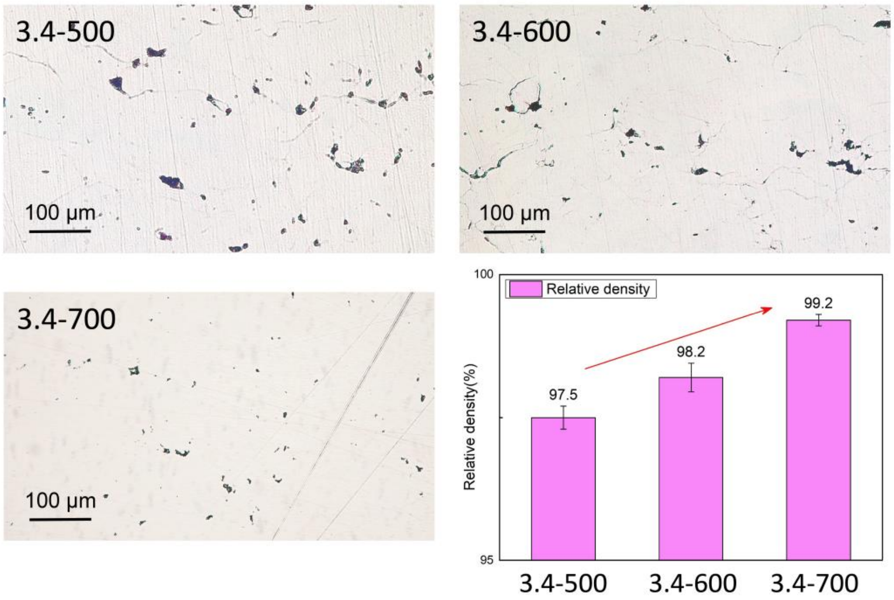

Fig. 3- 3 Relative density evolution with increasing gas temperature and corresponding cross-sectional microstructure.

After optimizing the processing parameters, the cross-sectional microstructures of cold-sprayed Cu-0.2O and pure Cu using the spraying parameters of 3.4 MPa and 700 ℃ are shown in **Fig. 3-4.** The originally spherical Cu powders are significantly deformed into a lath-like shape after deposition, with visible internal defects such as micro-pores and cracks, which we attribute to poor interfacial bonding. The optical microscopy images in **Fig. 3-4** reveal that both samples exhibit relatively dense cross-sectional microstructures, with relative densities exceeding 99 %. However, compared to pure Cu, the Cu-0.2O sample shows noticeably more micro-pores and voids. This difference results from the higher microhardness of the oxides compared to the Cu matrix, which increases resistance to plastic deformation during deposition, promoting the formation of micro-pores and voids and causing a slight decrease in relative density from about 99.7 % for pure Cu to 99.2 % for Cu-0.2O. Further details will be discussed in the following sections.

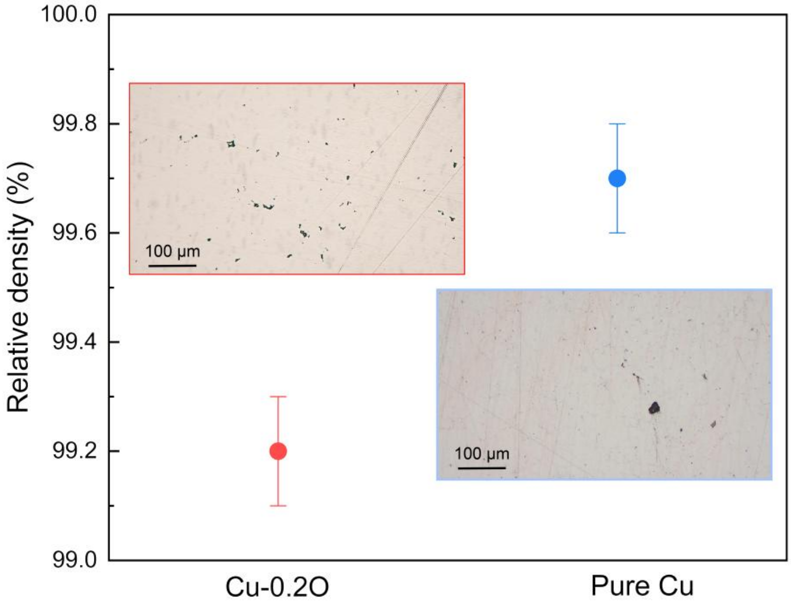

Fig. 3- 4 Relative density and cross-sectional microstructure of as-sprayed Cu-0.2O and pure Cu. The cross-section of each sample was photographed by OM.

3.2.2. Influence of the spraying parameters on mechanical properties

The microhardness comparison of different cold-sprayed Cu samples is presented in **Fig. 3-5.** Severe plastic deformation combined with work hardening during the cold spray process significantly enhances microhardness. While the Vickers microhardness of pure casting Cu is approximately 75 HV, our cold-sprayed Cu shows a notable increase, rising from 112 HV to 136 HV as the spraying parameters increase. Notably, samples sprayed under lower parameters exhibit greater variability in microhardness, reflected by a higher standard deviation. This is due to the tamping effect: when spraying parameters are insufficiently high, the initially deposited layers have lower relative density. Subsequent particles impact and compact these layers, inducing secondary plastic deformation and improving compactness. As a result, the microhardness at the bottom of the deposition is higher than at the top. With increasing spraying parameters, overall compactness and deposition efficiency improve, reducing the tamping effect and producing a more uniform microhardness distribution throughout the sample.

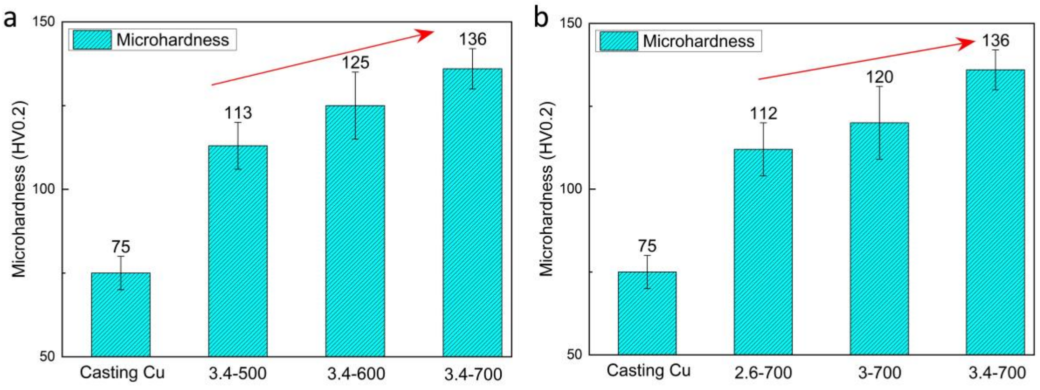

Fig. 3- 5 Hardness comparison of casting Cu with cold-sprayed Cu-0.2O of different process parameters. (a) Hardness comparison with increasing gas temperature. (b) Hardness comparison with increasing gas pressure.

3.2.3. Influence of the spraying parameters on conductivity

The thermal conductivity of as-sprayed Cu-0.2O samples under different spraying parameters is compared in **Fig. 3-6**. As gas pressure and temperature increase, improved interfacial bonding reduces defects, minimizing obstacles to heat transfer. The cold-sprayed Cu-0.2O samples exhibit thermal conductivity values ranging from 259 to 310 W/m·K, which is more than 80% of that of pure cast Cu. Notably, thermal conductivity shows an almost linear increase with spraying pressure, while no clear trend is observed with rising temperature. This suggests that spraying pressure has a more significant impact on thermal conductivity than spraying temperature.

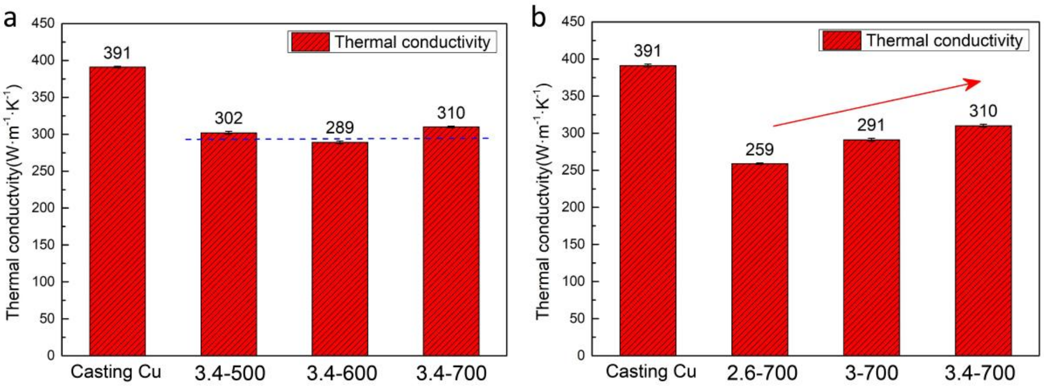

Fig. 3- 6 Thermal conductivity comparison of casting Cu with cold-sprayed Cu-0.2O of different process parameters. (a) Thermal conductivity with increasing gas temperature. (b) Thermal conductivity with increasing gas pressure.

The electrical conductivity of the as-sprayed samples under different spraying parameters is shown in **Fig. 3-7**. Similar to thermal conductivity, electrical conductivity increases as the spraying temperature rises from 500 ℃ to 700 ℃, improving from approximately 70% IACS to 85.5% IACS, approaching the value of pure casting Cu. A comparable trend is observed with the spraying pressure increases from 2.6 MPa to 3.4 MPa, where conductivity gradually rises from 75.3% IACS to 85.5% IACS. The increase in electrical conductivity is more pronounced with higher gas temperature than with gas pressure, indicating that spraying temperature has a greater influence. This is because higher temperatures promote metallurgical bonding between adjacent particles and reduce internal defects, resulting in improved electrical performance.

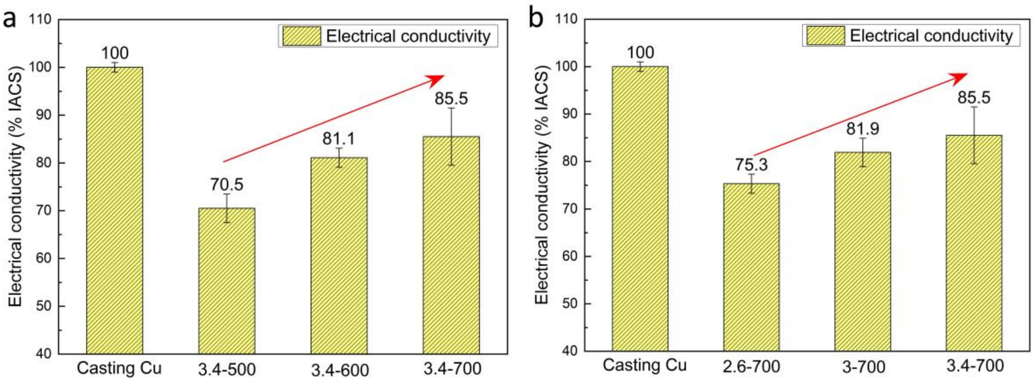

Fig. 3- 7 Electrical conductivity comparison of casting Cu with cold-sprayed Cu-0.2O of different

process parameters. (a) Electrical conductivity with increasing gas temperature. (b) Electrical conductivity with increasing gas pressure.

3.2.4. Microstructural evolution under different spraying parameters

The IPF mappings of cold-sprayed Cu-0.2O samples under different spraying parameters are shown in **Fig. 3-8** and **Fig. 3-9**. All samples exhibit a bimodal microstructure, characterized by coarse grains in the particle interiors and fine grains at particle interfaces. The primary difference between samples at varying gas pressures lies in grain size distribution, as shown in **Fig. 3-8**. Increasing the spraying pressure from 2.6 MPa to 3.4 MPa causes the area-weighted grain size to first slightly decrease from 2.75 μm to 2.63 μm, then sharply drop to 1.75 μm. A similar trend is observed with temperature, where increasing from 500 ℃ to 700 ℃ gradually reduces the area-weighted grain size from 1.88 μm to 1.75 μm.

At the lowest gas pressure (2.6 MPa), a relatively large fraction of coarse grains (9–10 μm) coexists with a significant portion of fine and ultra-fine grains (<1 μm), indicating pronounced heterogeneity. When pressure increases to 3 MPa, the coarse grains shrink to 6–7 μm, while medium-sized grains (2–4 μm) markedly increase in area fraction. At 3.4 MPa, coarse grains reduce further to less than 5 μm, accompanied by a continued rise in fine and ultra-fine grains. These changes suggest that higher spraying pressure promotes grain refinement, shifting the dominant grain size from coarse to medium and eventually fine grains, thereby reducing the bimodal nature and creating a more uniform grain size distribution.

In contrast, the effect of spraying temperature on grain size distribution is less pronounced. As shown in **Fig. 3-9,** increasing temperature leads to modest grain refinement, with area-weighted grain size decreasing from 1.88 μm to 1.75 μm. The grain size distribution remains relatively uniform, with only a small fraction of coarse grains near 6 μm.

Based on these observations, we conclude that increasing gas pressure significantly enhances grain refinement and reduces bimodal microstructure, resulting in finer and more uniform grains. According to the Hall-Petch effect, these finer grains make a substantial contribution to the improvement of microhardness. The influence of gas temperature on grain refinement is comparatively minor. This is because gas pressure directly affects particle velocity; higher velocity generates greater strain rates upon impact, which more effectively triggers dynamic recrystallization and grain refinement in cold-sprayed Cu-0.2O samples.

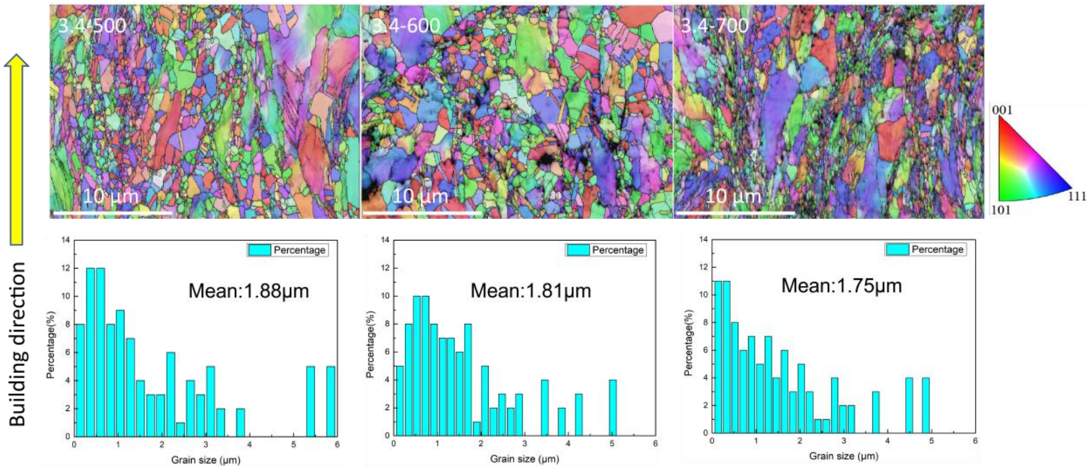

Fig. 3- 8 Microstructure evolution with gas pressure increases. The corresponding grain size distributions of each sample are attached at the bottom of the IPF mappings.

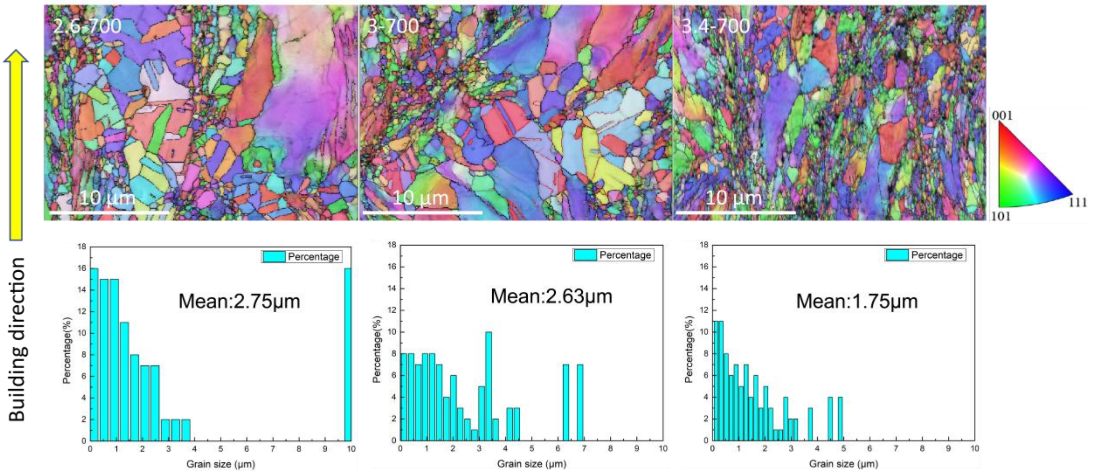

Fig. 3- 9 Microstructure evolution with gas temperature increases. Corresponding grain size distributions of each sample are attached at the bottom of the IPF mappings.

In addition to grain size, dislocation density plays a crucial role in enhancing microhardness. Previous research on pure Cu processed by LPBF demonstrated that high dislocation densities, ranging from 10^{15} to 10^{16} m^{-2}, significantly contribute to both microhardness and strength [52]. The distribution of Geometrically Necessary Dislocations (GND) in as-sprayed Cu-0.2O samples is presented in **Fig. 3-10** and **Fig. 3-11**. The high dislocation density induced by severe plastic deformation during the cold spray process can also reach the level of 10^{15} m^{-2}, which is believed to have a significant influence on enhanced microhardness. Meanwhile, it can be observed that along with gas pressure increase, the GND density of the cold-sprayed Cu-0.2O samples is enhanced from 16.35×10^{14} m^{-2} to 29.03×10^{14} m^{-2}. The same evolution trend is kept as the gas temperature increases, which leads to the GND density increase from 14.72×10^{14} m^{-2} to 29.03×10^{14} m^{-2}, respectively.

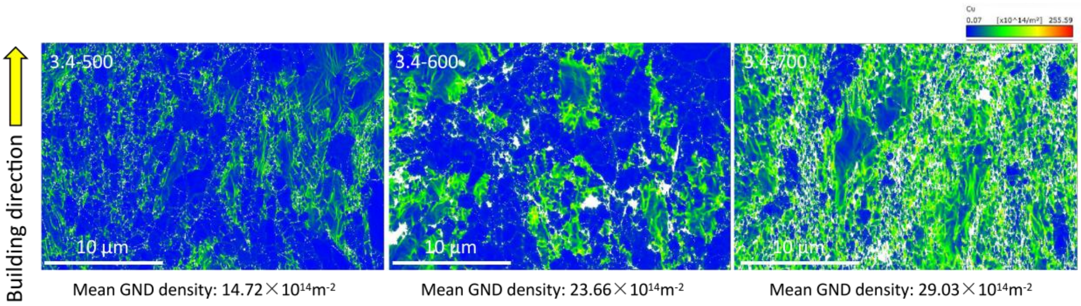

Fig. 3- 10 The GND density evolution with the gas pressure increasing from 2.6 MPa to 3.4 MPa. The mean GND density of each sample is attached at the bottom.

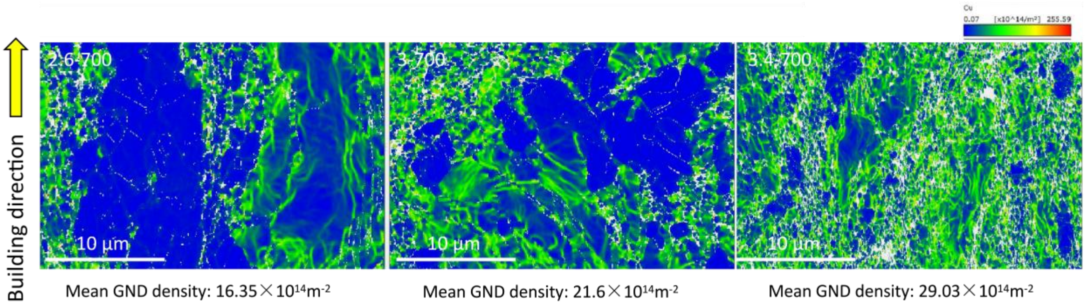

Fig. 3- 11 The GND density evolution with the gas temperature increasing from 500 °C to 700 °C. The mean GND density of each sample is attached at the bottom.

A comprehensive comparison of the above-mentioned cold sprayed samples, including their average grain size and GND density, is summarized in **Table 3**. By integrating the microstructure evolution of these as-sprayed samples with their corresponding mechanical properties and thermal/electrical conductivity, it can be inferred that both gas temperature and gas pressure play important roles in driving microstructure evolution, thereby significantly influencing overall material properties. As the gas pressure increases, the enhanced particle velocity upon impact promotes severe plastic deformation, which in turn facilitates dynamic recrystallization primarily at the particle interfaces, resulting in the generation of a larger quantity of ultra-fine and nanoscale grains. Therefore, increasing the gas pressure induces a marked grain refinement effect. Moreover, the intensified plastic deformation encourages dislocation accumulation at particle interfaces, thereby increasing the corresponding GND density. The refined grain structure combined with the elevated dislocation density jointly contributes to the observed increase in microhardness. Additionally, higher gas pressure aids in compacting the as-sprayed samples, improving relative density through the elimination of pores and weak bonding interfaces. These defects are critical factors limiting thermal and electrical conductivity because they can effectively obstruct heat and electrical transfer. Consequently, both thermal and electrical conductivities tend to improve as gas pressure increases. Gas temperature also plays a significant role by enhancing metallurgical bonding between adjacent particles upon impact. As a result, higher gas temperature leads to higher relative density in the as-sprayed samples. It also contributes to grain refinement, although this effect is less pronounced compared to that of increasing gas pressure. Based on the optimization of the above processing parameters, we have selected 3.4 MPa and 700 °C as the optimal conditions, and the Cu-0.2O samples discussed in the following sections of this chapter are sprayed using these parameters.

Table 3-1 Comprehensive comparison of the as-sprayed samples with their area-weighted mean grain size and mean GND density.

Samples	Area-weighted mean grain size/μm	Mean GND density/$10^{14}m^{-2}$
3.4-500	1.88	14.72
3.4-600	1.81	23.66

3.4-700	1.75	29.03
3-700	2.63	21.6
2.6-700	2.75	16.35

3.3. Mechanical properties and thermal/electrical conductivity

The microhardness and compressive properties of cold-sprayed Cu-0.2O were compared with those of cold-sprayed pure Cu, as illustrated in **Figs. 3-12(a)** and **(b)**. The Cu-0.2O sample exhibited a hardness of approximately 136 HV, representing a 15% increase over pure Cu, which had a hardness of 118 HV (**Fig. 3-12(a)**). In terms of compressive behavior, the Cu-0.2O sample demonstrated significantly higher compressive strength than pure Cu, with a compressive yield strength of over 450 MPa and an ultimate compressive strength exceeding 600 MPa. In contrast, pure Cu exhibited approximately 300 MPa of yield strength and an ultimate compressive strength of around 400 MPa, despite both materials displaying nearly identical compressive plasticity.

The electrical and thermal conductivity of the cold-sprayed Cu-0.2O alloy were measured at 85.5% IACS and 310 W/m·K, respectively. Notably, the results indicate negligible loss in electrical and thermal conductivity compared to cold-sprayed pure Cu (85.3% IACS and 343 W/m·K). When considering both hardness and conductivity—properties for which a trade-off typically exists—the cold-sprayed Cu-0.2O sample exhibits an exceptional combination of microhardness and electrical/thermal conductivity. As illustrated in **Figs. 3-12(c)** and **(d)**, high-purity Cu produced via casting exhibits the highest thermal and electrical conductivity, albeit with a hardness below 75 HV. Although the incorporation of ceramic reinforcements such as SiC and Al_2O_3 enhances the hardness of Cu composites to approximately 150 HV, this strengthening effect comes at the expense of significantly reduced thermal and electrical conductivity, which fall below 200 W/m·K and 60% IACS, respectively. Notably, the Cu-0.2O sample demonstrates a distinctive balance of hardness/strength and conductivity, outperforming both cast Cu and nearly all existing cold-spray Cu-ceramic composites. This suggests that the controlled introduction of oxygen into Cu powders may provide a viable pathway to mitigate the conventional trade-off between hardness and conductivity in cold-sprayed Cu components.

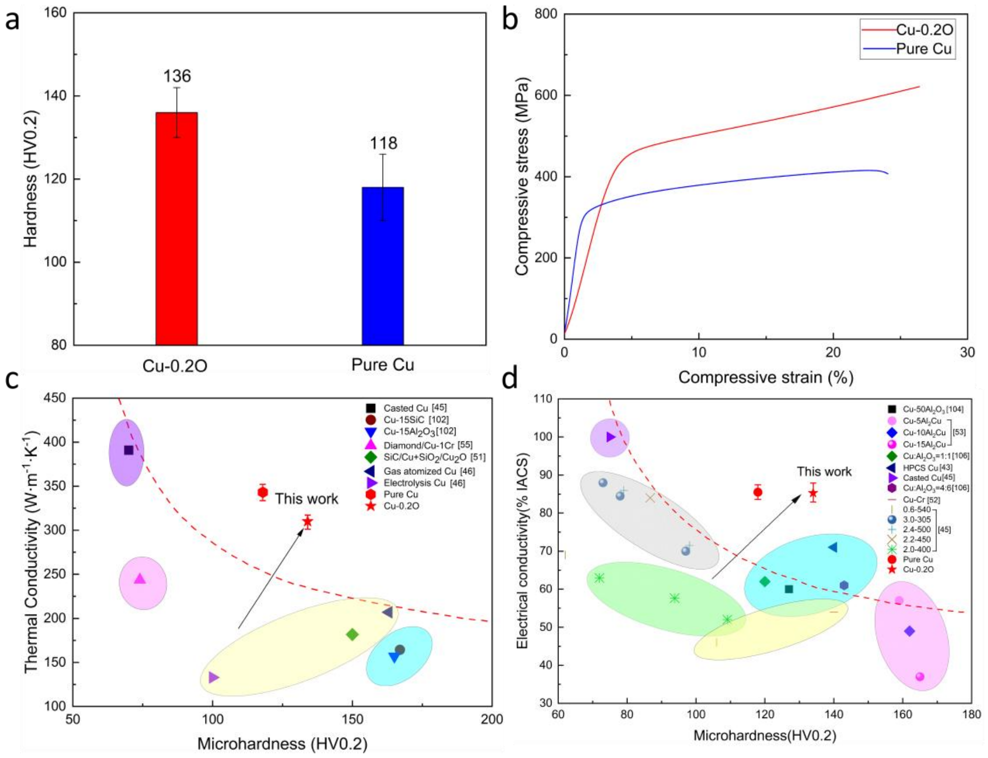

Fig. 3- 12 Performance and properties of as sprayed Cu-0.2O and pure Cu. (a) Microhardness comparison; (b) Compressive stress-strain curves of Cu-0.2O and pure Cu; (c) Microhardness and thermal conductivity comparison with other Cu based composites; (d) Microhardness and electrical conductivity comparison with other Cu based composites.

3.4. Cross-sectional microstructure

Fig. 3-13 presents the cross-sectional microstructures of both Cu-0.2O and pure Cu samples. During deposition, the accelerated Cu powders were ejected from the nozzle and impacted the substrate at supersonic velocity. This impact caused the spherical powder particles to deform into a lath-shaped morphology, as highlighted in **Fig. 3-13(a)**. High-magnification examination of individual powders (**Fig. 3-13(b)**) revealed the presence of numerous nanoscale dark-contrast features in the Cu-0.2O sample. Notably, these features exhibited a hierarchical distribution pattern: the majority were concentrated near powder boundaries, with significantly fewer observed within powder interiors. Furthermore, within grain interiors, these features predominantly aligned along grain boundaries. In contrast, the cold-sprayed pure copper sample showed no evidence of such dark-contrast features, as clearly demonstrated in **Figs. 3-13(c)** and **(d)**.

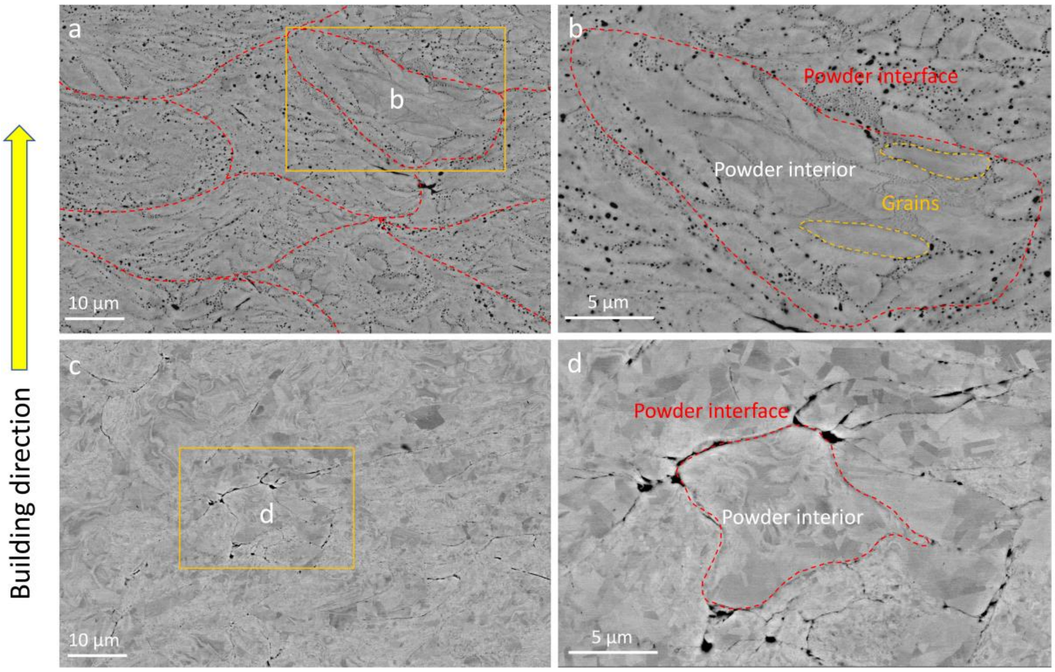

Fig. 3-13 The BSE images of the cross-sectional microstructure of (a) Cu-0.2O; (b) magnified region in (a). (c) Pure Cu; (d) magnified region in (c).

EBSD analysis of the Cu-0.2O and pure Cu samples is presented in **Fig. 3-14**. The Cu-0.2O sample displayed a characteristic bimodal grain size distribution (**Fig. 3-14(a)**). It can be seen that ultra-fine and nanoscale grains were primarily concentrated at inter-powder boundaries, while coarser grains dominated the powder interiors. Comparative analysis revealed that despite both samples exhibiting bimodal structures, the Cu-0.2O sample possessed a considerably smaller average grain size (1.75 μm) than pure Cu (5.83 μm) (**Figs. 3-14(a)** and **(b)**). Furthermore, the Cu-0.2O sample contained a substantially greater proportion of ultra-fine grains (<1 μm) compared to its pure Cu counterpart. Notably, while abundant annealing twins were observed in the pure Cu sample, they were scarcely present in the Cu-0.2O sample.

The geometrically necessary dislocation (GND) density distributions of both samples are shown in **Figs. 3-14(c)** and **(d)**. It was observed that dislocations tended to concentrate at particle interfacial regions. Quantitative analysis demonstrated that the Cu-0.2O sample exhibited nearly triple the GND density (29.03×10^{14} m^{-2}) of pure Cu (9.47×10^{14} m^{-2}).

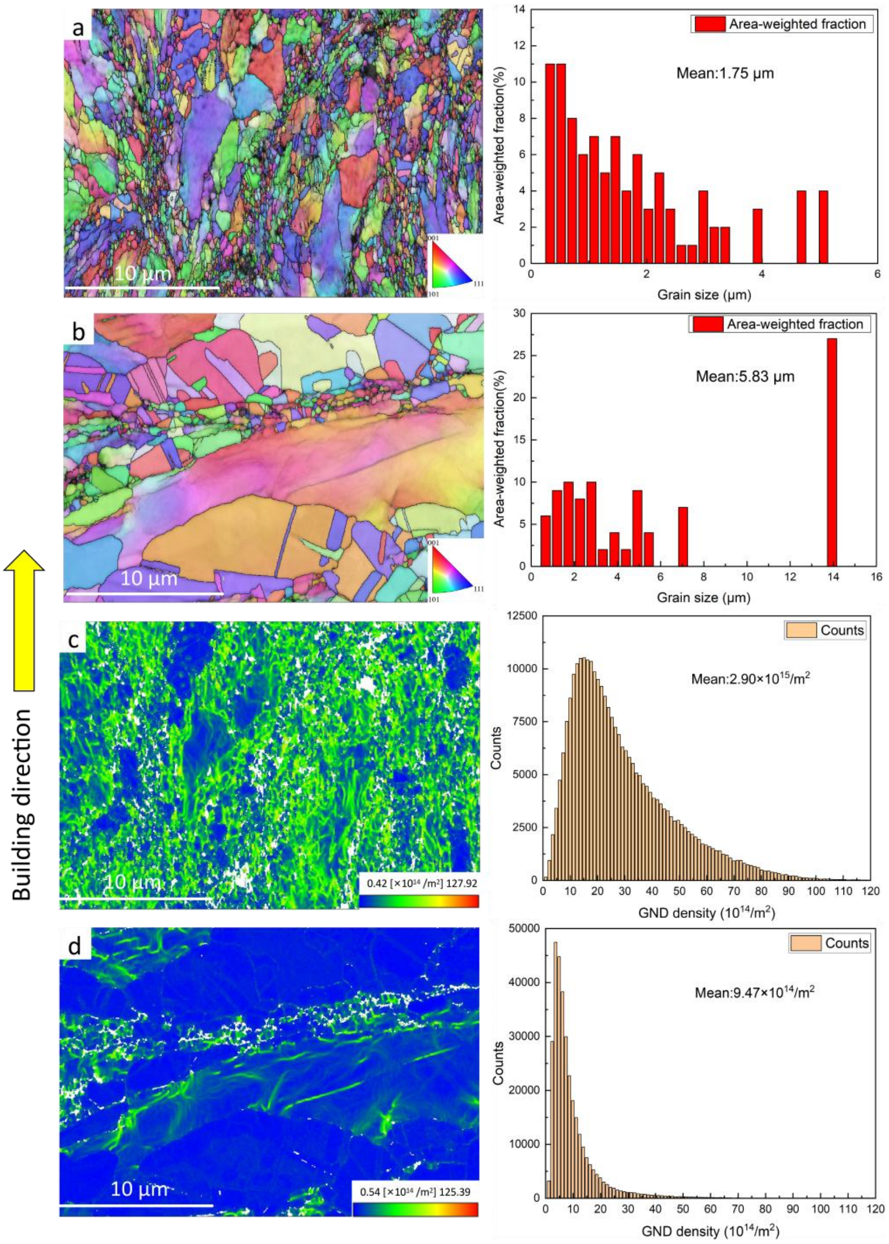

Fig. 3- 14 Inverse pole figure Z (IPFZ) colored orientation map and GND distribution of Cu-0.2O and pure Cu. (a) and (b): IPFZ mappings of Cu-0.2O and pure Cu, respectively; (c) and (d): GND density of Cu-0.2O and pure Cu, respectively. The grain size distribution and GND distribution on the right are attached to each figure.

The nanoscale dark-contrast features observed in **Fig. 3-13** were systematically investigated using multi-scale characterization techniques. **Fig. 3-15(a)** presents a bright-field (BF) TEM image of the cold-sprayed Cu-0.2O sample, revealing numerous bright-contrast domains (indicated by yellow circles) preferentially located near grain boundaries. The contrast variation suggests these domains represent significantly thinner regions compared to their surroundings. Based on comparative analysis of morphological characteristics - including feature geometry, dimensional scale, and spatial distribution - these bright-contrast domains in the BF-TEM images exhibit direct correlation with the dark-contrast features previously observed in **Fig. 3-13**.

Selected area electron diffraction (SAED) analysis conducted on these bright-contrast domains (**Fig. 3-15(b)**) revealed two distinct sets of diffraction patterns. The pattern with smaller interplanar spacing was indexed to the Cu matrix (marked with white circles) along the [011] zone axis, while the second set with larger spacings (marked with red circles) corresponded to Cu_2O. The Cu_2O phase was conclusively identified by measuring the deviation of interplanar spacing. An orientation relationship of $[011]Cu$ // $[011]Cu_2O$ and $\{111\}Cu$ // $\{111\}Cu_2O$ was observed between the Cu_2O precipitate and the Cu matrix.

Complementary HAADF-STEM imaging combined with EDS mapping provided further confirmation of Cu_2O nanoprecipitates. In HAADF-STEM mode, three distinct features were resolved (**Fig. 3-16(a)**): (1) bright-contrast Cu matrix, (2) dark-contrast Cu_2O nanoprecipitates, and (3) completely black regions representing nanoscale voids. EDS elemental mapping (**Figs. 3-16(b)** and **(c)**) clearly revealed oxygen distribution within the Cu_2O + Cu region. High-resolution HAADF-STEM imaging and corresponding Fast Fourier Transform (FFT) analysis (**Figs. 3-16(d)** and **(e)**) distinctly identified the structures of the Cu_2O nanoprecipitates and the diffraction patterns from both Cu_2O (red circles) and Cu (white circles) phases. Here, an orientation relationship of [011] Cu // [011] Cu_2O and {111} Cu // {111} Cu_2O existed between the Cu_2O precipitate and the adjacent Cu matrix. Subsequent Inverse FFT (IFFT) reconstruction (**Figs 3-16(f)** and **(g)**) after selective masking yielded interplanar spacing measurements of 2.48 Å for Cu_2O (111) and 2.10 Å for Cu (111), in excellent agreement with theoretical values.

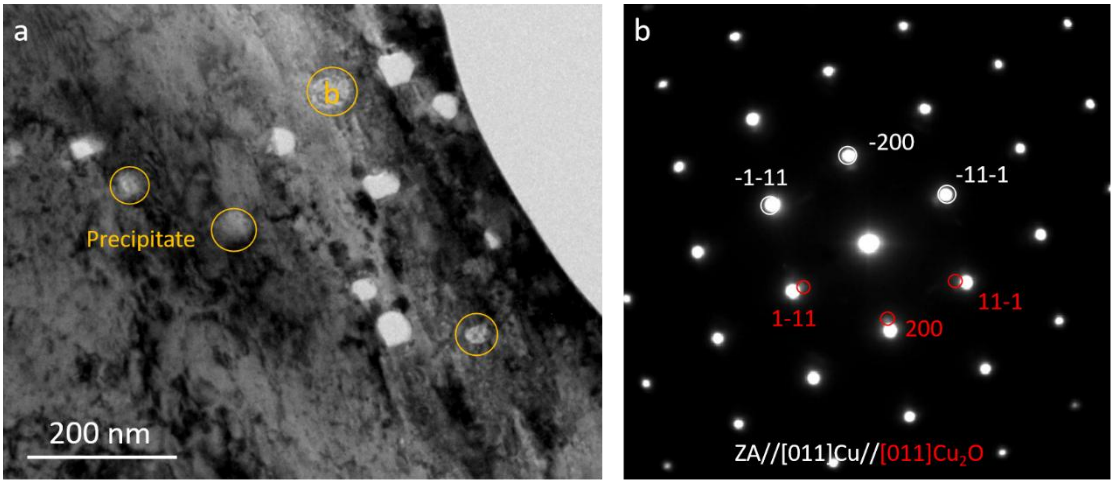

Fig. 3-15 TEM images of Cu-0.2O with nanoprecipitates located at grain boundaries. (a) BF-image of the nanoprecipitates and the adjacent Cu matrix. (b) SAED patterns collected from the nanoprecipitate region.

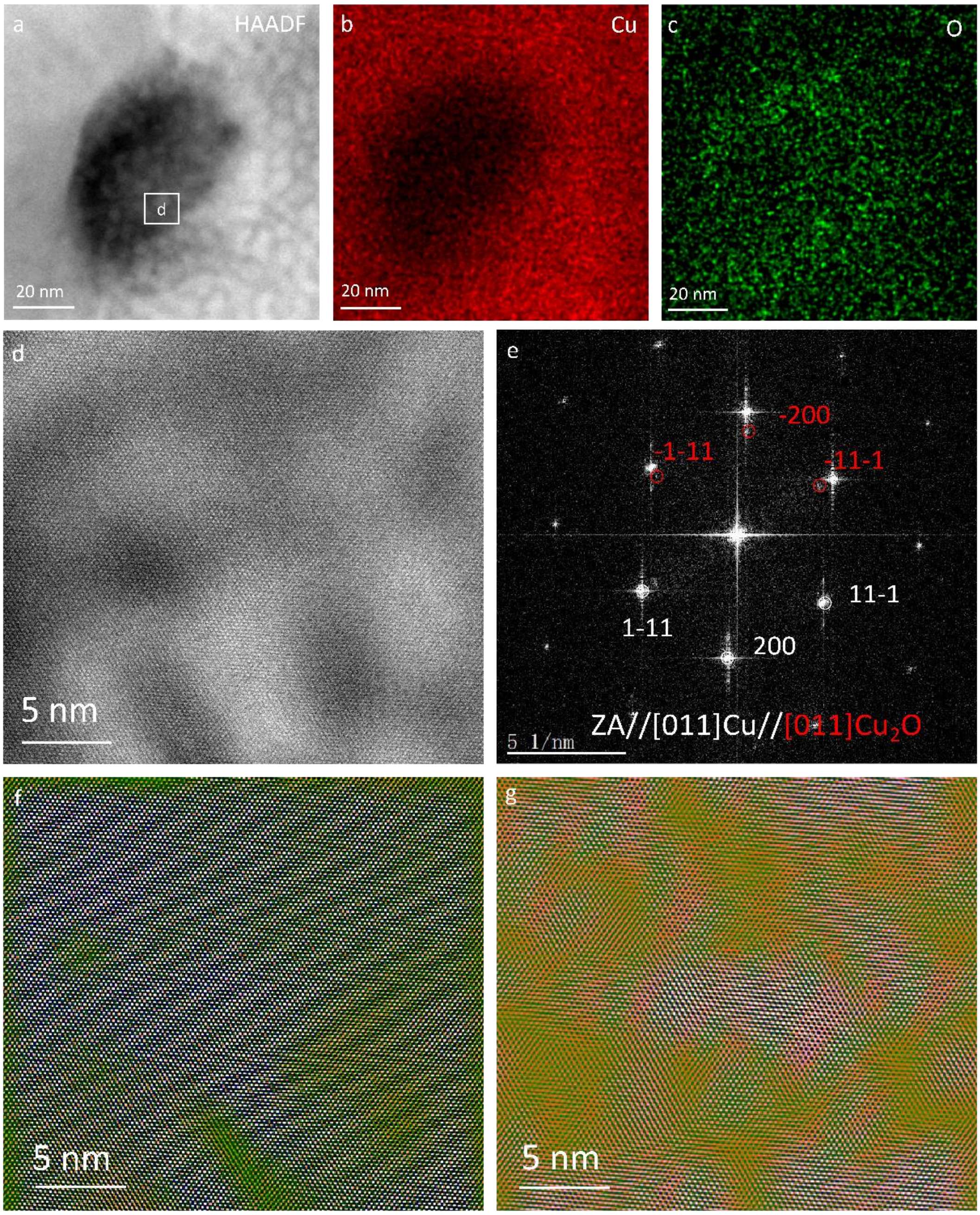

Fig. 3- 16 HRTEM image showing the nanoprecipitates region. (a-c) HAADF-STEM image and corresponding EDS mappings of nanoprecipitates and their adjacent areas. (d) HRTEM image of the nanoprecipitates enlarged in (a); (e) Corresponding reduced FFT patterns of Cu_2O (marked by red circles) and Cu matrix (marked by white circles); (f) IFFT image of Cu matrix; (g) IFFT image of Cu_2O.

3.5. Discussion

3.5.1. Bimodal microstructure and hierarchical distribution of Cu_2O precipitates

Cold spray, as a process involving severe plastic deformation, is characterized by ultra-high strain rates and localized temperature increases at the interfacial region. These thermodynamic phenomena are widely recognized to exert a significant influence on the intrinsic microstructure of the as-sprayed samples, thereby determining their resultant properties. To examine the thermal and mechanical response during powder impact, a CEL approach was implemented to simulate the collision of a single Cu powder with an Al substrate, with results presented in **Fig. 3-17**. **Figs. 3-17(a)** and **(b)** display the plastic strain and temperature distribution of the Cu powder, while **Figs. 3-17(c)** and **(d)** illustrate the strain and temperature evolution of the particle interface during the impact. The high-velocity impact induces severe plastic deformation in the spherical Cu powder, causing its transformation into a lamellar morphology. The conversion of kinetic energy to thermal energy, coupled with the exceptionally high strain rate ($>10^9$ s^{-1}) that inhibits heat dissipation, generates significant temperature elevation at the powder-substrate interface. As the powder surface experiences primary deformation, it develops the maximum equivalent plastic strain exceeding 600% (**Fig. 3-17(a)**). Concurrently, heat generated by plastic deformation becomes concentrated at the surface, producing peak temperatures approaching 420°C. The superior thermal conductivity of Cu subsequently promotes heat conduction from the surface toward the powder interior, establishing a distinct thermal gradient (**Fig. 3-17(b)**).

The extreme thermomechanical conditions during impact provide a mechanistic understanding of the observed bimodal grain structure formation [110, 111]. Upon supersonic impact, surface-localized heating from energy dissipation initiates dynamic recrystallization at the powder surface, as illustrated in **Fig. 3-18**. The process begins with dislocation propagation and lattice rotation along the deformation direction, followed by significant dislocation accumulation at the surface that first forms elongated subgrains. As plastic strain continues to accumulate, these elongated subgrains progressively transform into smaller equiaxed grains, with increasing misorientation between adjacent grains developing into high-angle grain boundaries to accommodate further deformation. This sequence ultimately produces refined sub-micron and nanoscale grains at the powder surface, while the core region retains relatively coarse grains due to experiencing substantially less plastic deformation [26], thereby creating the characteristic bimodal microstructure in both of the cold-sprayed Cu-0.2O and pure Cu samples.

It is observed in the raw Cu-0.2O powders that the Cu2O precipitates are uniformly distributed along grain boundaries. However, SEM analysis reveals a distinct radial gradient in Cu_2O precipitate density, with the highest concentration observed at the powder surface that gradually diminishes toward the interior regions. The schematic diagram of the migration of Cu_2O precipitates is shown in **Fig. 3-19**. Since these precipitates concentrate along grain boundaries, the grain boundary behavior will significantly affect their distributions. Grain boundary migration is predominantly determined by the temperature gradient, where regions with higher temperature appear to be more attractive for grain boundaries, as supported by molecular dynamics (MD) and phase field simulations [112, 113]. According to our FEM simulation, the elevated surface temperatures provide a greater thermodynamic driving force for grain boundary migration compared to the relatively cooler powder cores. These precipitates, along with grain boundary migration, will be transferred to the powder interfacial regions, as illustrated in **Fig. 3-19(b)**. Consequently, the enhanced precipitation kinetics at high-temperature surface regions result in significantly greater Cu_2O precipitate density at the powder surface relative to interior regions.

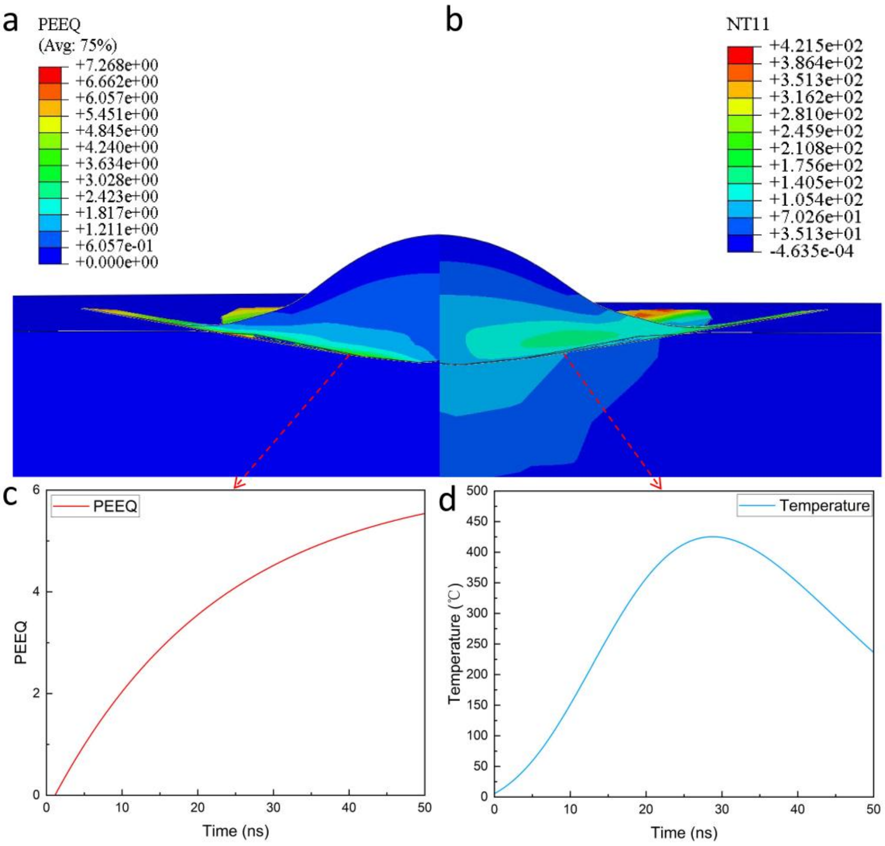

Fig. 3- 17 Simulation results of the Cu powder impacting at the Al substrate at 50 ns. (a) Equivalent plastic strain (PEEQ) distribution of Cu powder. (b) Temperature distribution of the Cu powder. (c) PEEQ evolution of the particle interface. (d) Temperature evolution of the particle interface.

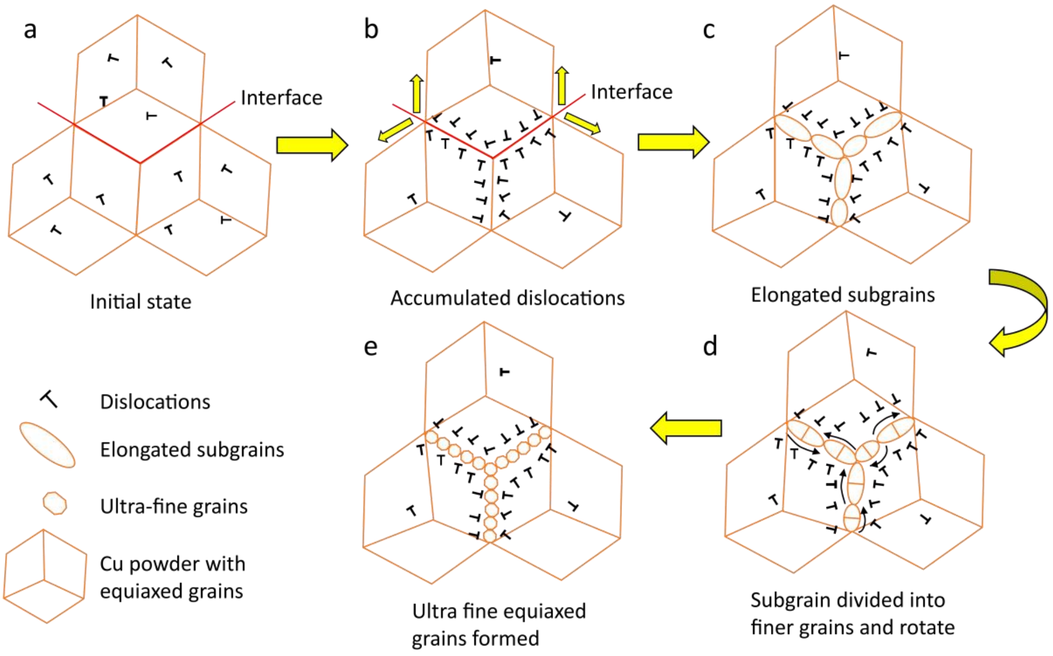

Fig. 3- 18 Schematic diagram of microstructure evolution during particle impact. (a) Initial state with a uniform dislocation distribution; (b) upon impact, numerous dislocations start to accumulate at the interfaces between adjacent particles; (c) the accumulated dislocations trigger the generation of elongated sub-grains; (d) elongated sub-grains are divided into equiaxed grains and rotate to accommodate more strain; (e) finally equiaxed ultra-fine and nanograins are formed at particle interface.

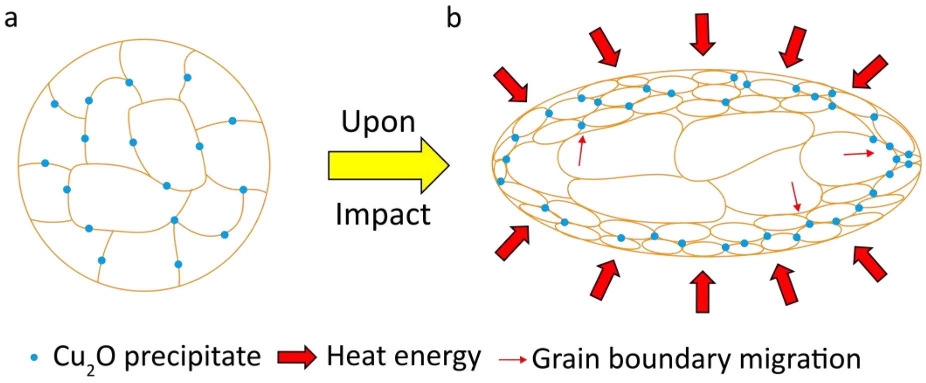

Fig. 3- 19 Schematic diagram of the Cu2O precipitates migrating towards powder interfaces along with grain boundary migration due to thermal gradient during the spraying process. (a) Initial spherical powder. (b) Severely deformed powder upon impacting the substrate.

Additionally, as observed in **Figs. 3-13**, **3-15**, and **3-16**, the Cu_2O nanoprecipitates exhibit a preferential distribution along grain boundaries adjacent to nanoscale voids. The underlying mechanism can be described as follows: Grain rotation, induced by dislocation accumulation, generates residual stress at the powder surface. This stress, in conjunction with localized thermal expansion, promotes the formation of internal defects such as voids. These voids preferentially nucleate at grain boundaries due to their higher energy state compared to intragranular regions, resulting in a thermodynamically unstable structure. According to the void healing mechanism proposed by Ouyang et al. [114], heat treatment at 500 °C facilitates pore healing primarily through nanograin growth at particle interfaces and grain boundary migration toward these regions. Grain boundaries serve as diffusion pathways for vacancies and adjacent elements, enabling oxide migration along moving boundaries to fill voids and promote healing. In the case of cold-sprayed Cu with Cu_2O precipitates, impact-induced peak temperatures can reach ~420 °C (**Figs. 3-17(b)** and

(d)), a condition sufficient to initiate grain boundary migration and oxide diffusion toward pores. However, the limited duration of localized heating restricts significant grain boundary motion, preventing complete pore filling. Furthermore, Cu_2O precipitates pinned at grain boundaries inhibit grain growth, leading to their clustering near voids and reducing void size to the nanoscale. Nevertheless, full void healing is not achieved under these conditions.

3.5.2. Cu_2O precipitation strengthening mechanism

Solid solutions, grain boundaries, precipitation, and dislocations all contribute to the strengthening of the as-sprayed Cu-0.2O and pure Cu samples. The strengthening mechanism is shown in the formula below:

$$\sigma_{ys} = \sigma_0 + \sigma_{gb} + \sigma_{ss} + \sigma_{dis} + \sigma_p \tag{4}$$

Where σ_{ys} represents the total yield strength; σ_0 denotes the intrinsic frictional stress of Cu, approximately 60 MPa [115]. σ_{gb} signifies the strength contributed by grain boundaries, σ_{ss} refers to the strengthening by solid solutions, σ_{dis} indicates the strength contributed by dislocations, and σ_p represents the strength attributed to precipitation. Due to the extremely low solubility of oxygen in the Cu matrix, σ_{ss} is neglected. According to the grain size distribution depicted in **Fig. 3-14(a)**, the Cu-0.2O sample's grain size distribution exhibits a shift towards finer grains, with a higher proportion of ultra-fine and nano-sized grains at particle interfaces compared to pure Cu. With more intense deformation, the quantity of fine and ultra-fine grains at the interface between adjacent particles increases due to the enhanced dynamic recrystallization. According to the Hall-Petch effect [116, 117], there exists a relationship between strength and the grain size, shown in (5):

$$\sigma_{gb} = k \cdot d^{-1/2} \tag{5}$$

Where k is the constant based on the materials ($0.11 \text{MPa} \cdot \text{m}^{1/2}$) [115] and d refers to the average grain size. Since grain size is inversely proportional to strength, a higher yield strength was achieved with finer grains. With the mean grain size of the Cu-0.2O and pure Cu sample being approximately 1.75 μm and 5.83 μm, the contribution of the grain boundaries is estimated to be 83 MPa and 45 MPa. Moreover, the Cu-0.2O sample exhibits a significantly higher GND density, nearly triple that of pure Cu. As more dislocations accumulate at particle interfaces, lattice sliding and secondary deformation are effectively impeded. The impact of dislocation density on strength can be summarized as follows [118]:

$$\sigma_{dis} = M\alpha Gb \cdot \rho_{GND}^{1/2} \tag{6}$$

where M is the Taylor factor, which equals approximately 3 for Cu; α is the Nye factor, around 0.2; G refers to the shear modulus (44.7 GPa); b is the Burgers factor (0.256 nm), and ρ_{GND} refers to the geometrically necessary dislocation (GND) density measured by the EBSD characterization. It is noteworthy that the strength contributed by the dislocations is proportional to the GND density. Based on the aforementioned calculations, the strengthening effect resulting from the increased dislocation density of Cu-0.2O and pure Cu can be inferred to be approximately 300 MPa and 215 MPa considering mis-indexing, respectively.

The precipitation strengthening effect of Cu_2O is estimated via the Orawan model [119, 120], as illustrated in the formula below:

$$\sigma_p = M\frac{0.4Gb}{\pi\sqrt{1-v}} \cdot \frac{ln(\frac{2r}{b})}{1.2r(\frac{2\pi}{3f})^{1/2}} \tag{7}$$

Where *M, G, and b* refer to the same components as the dislocation strengthening model, v denotes Poisson’s ratio (0.34), r represents the mean radius of a spherical Cu_2O precipitate (approximately 9 nm), and f signifies the volume fraction of the precipitate, which is around 2.65% assuming all the oxygen forms precipitation during the spraying. There is no precipitation in pure Cu; thus the precipitation strengthening for pure Cu is neglected. Taking the above calculations, the strengthening effect of Cu_2O precipitates is estimated as 65 MPa. The contributions of each strengthening mechanism to the yield strength of Cu-0.2O and pure Cu are illustrated in **Figs. 3-20(a)** and **(b)**, respectively. Overall, the σ_{ys} of the Cu-0.2O and pure Cu is calculated to be 508 MPa and 315 MPa, which is slightly higher than our experimental results shown in **Fig. 3-12(b)**. This deviation is predominantly caused by the nano-scaled voids and some weak bond interfaces present in the as-sprayed Cu-0.2O, which degrade the yield strength to some extent.

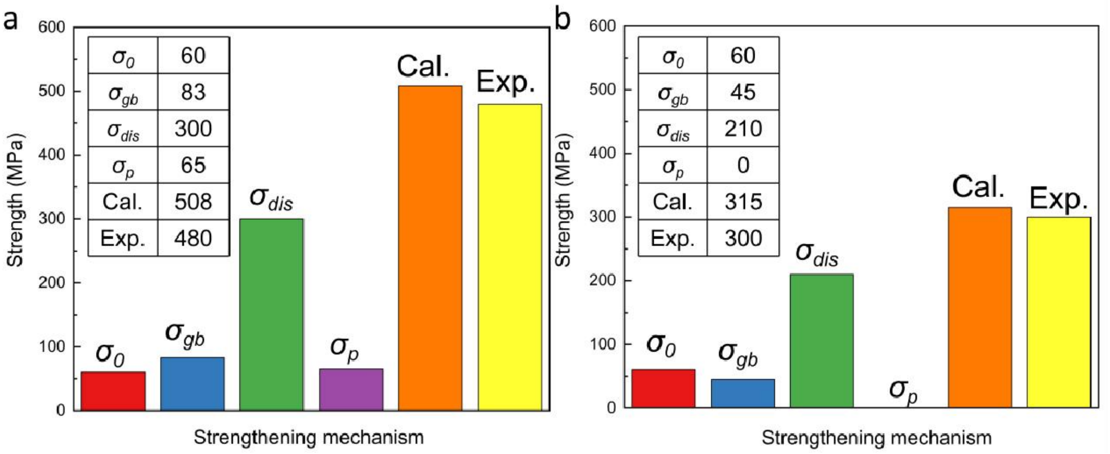

Fig. 3- 20 Schematic diagram of contributions to the yield strength of each strengthening mechanism. (a) Strengthening mechanism of Cu-0.2O. (b) Strengthening mechanism of pure Cu as a contrast. Cal. and Exp. refer to the calculated and experimental values of the yield strength, respectively.

To investigate the influence of the Cu_2O precipitates on the microstructure evolution during deposition of the Cu-0.2O sample, the recrystallization fraction mappings of cold-sprayed Cu-0.2O and pure Cu are generated using Channel 5 software and presented in **Fig. 3-21**. Here, grains are classified according to their average misorientation values. Those with misorientation values lower than 1° are considered totally recrystallized grains, while those with values higher than 7.5° are identified as severely deformed grains. Grains with misorientation values between 1° and 7.5° refer to substructures [121]. Blue, yellow, and red grains refer to the totally recrystallized grains, substructures, and deformed grains, respectively (the green area in **Fig. 3-21(a)** denotes zero resolution). In the case of our Cu-0.2O sample, substructures constitute approximately half of the grains; the number fraction of recrystallized grains is slightly higher than that of deformed grains, at 28% and 21% of the grains, respectively. Meanwhile, coarse grains are consistently considered as substructures, while fine grains comprise recrystallized grains and some deformed grains, as depicted in **Fig. 3-21(c)**. However, the pure Cu sample exhibits few deformed grains, with nearly 60% recrystallized grains and 40% substructures, as shown in **Fig. 3-21(b)** and **(d)**. Notably, the Cu-0.2O sample possesses a higher fraction of deformed grains and a significantly lower fraction of fully recrystallized grains compared to the pure Cu sample. This indicates that the presence of Cu_2O precipitates at grain boundaries effectively hinders the nucleation process [122, 123]. Here, the Cu_2O precipitation pinned at the grain boundaries will lower the grain boundary energy, thus impeding the grain boundary migration. Also, due to the misfit of the lattice parameter between Cu_2O and Cu, the existence of Cu_2O at grain boundaries can induce a stress field, thereby increasing the energy barrier for nucleation at grain boundaries. Therefore, the following grain growth is hindered, which leads to a refinement of grains. Besides, during the deposition, dislocations start to pile up at the particle interfaces where dynamic recrystallization occurs. The formation of ultra-fine and nano-grains is accompanied by the rearrangement and annihilation of dislocations. The existence of Cu_2O precipitates at grain boundaries will impede the annihilation of dislocations, thus maintaining a high GND density compared to that of pure Cu. Based on the comparison of grain size distribution, GND density, and recrystallization fraction mappings between these two samples, the strengthening mechanism of nanoscale Cu_2O precipitates can be summarized as follows: in addition to the precipitation strengthening effect, the nanoscale Cu_2O precipitates located at grain boundaries effectively impede the recovery and grain growth processes after recrystallization while providing a dislocation pinning effect. This results in numerous ultra-fine and nanograins at particle interfaces due to the promoted dynamic recrystallization. The refined grains and increased dislocation density both contribute to the enhancement of both hardness and compressive strength in the Cu-0.2O sample, as compared to pure Cu.

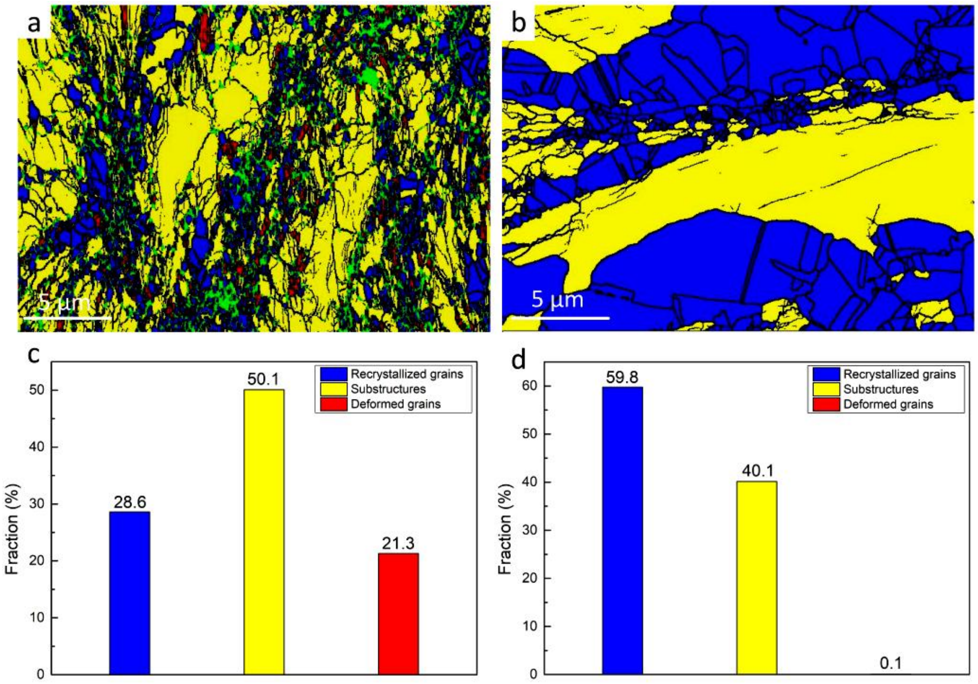

Fig. 3-21 Recrystallized fraction figure of (a) Cu-0.2O and (b) pure Cu. (c) Number fractions of different grains of Cu-0.2O. (d) Number fractions of different grains of pure Cu.

3.5.3. Maintained thermal and electrical conductivity

The electrical conductivity of a material will be affected by several factors that constrain electron motion, thereby restricting electrical conduction. According to Mattern's Law [124, 125], electrical resistivity, the inverse of electrical conductivity, can be summarized with the following components:

$$\Omega = \Omega_0 + \Omega_{\text{solid solution}} + \Omega_{\text{precipitate}} + \Omega_{\text{gb}} + \Omega_{\text{dis}} \qquad (8)$$

Here, Ω denotes the total resistivity, Ω_0 represents the intrinsic resistivity (a material-dependent property), while $\Omega_{\text{solid solution}}$, $\Omega_{\text{precipitate}}$, Ω_{gb}, and Ω_{dis} correspond to the resistivities contributed by the solid solution, precipitates, grain boundaries, and dislocations, respectively. As for our sample of cold-sprayed Cu with Cu_2O precipitates, the extremely low solubility of oxygen in the Cu matrix renders the resistivity contribution from the solid solution negligible. Consequently, Ω_0 is approximately 1.75 μΩ·cm, equivalent to that of pure Cu. Regarding Ω_{dis}, a dislocation density of 1 cm^{-2} may increase electrical resistivity by approximately 1.50 × 10^{-13} μΩ·cm [126]. Given an average dislocation density of 29.03 × 10^{14} m^{-2} (**Fig.**

3-14c), the calculated Ω_{dis} is 0.044 μΩ·cm.

The resistivity contribution from grain boundaries can be derived using the following equation:

$$\Omega_{gb} = \frac{3}{2} \times \frac{\lambda}{D} \times \frac{R}{1-R} \times \Omega_0 \tag{9}$$

Where λ is the mean free path of free electrons (40 nm for Cu) [125], D represents the average grain size, and R denotes the coefficient of reflection (approximately 0.506 for Cu) [126]. Based on the average grain size of 1.75 μm (**Fig. 3-14(a)**), the grain boundary contribution to resistivity is 0.052 μΩ·cm. Taking the influence of grain boundaries and dislocation density, the estimated resistivity is 1.85 μΩ·cm, with a corresponding conductivity of 53.9 MS/m.

For Cu_2O precipitates, the resistivity at room temperature is approximately 100 μΩ·cm, corresponding to a conductivity of 1 MS/m. Assuming all the oxygen precipitated (0.2 wt.%), the corresponding volume fraction of Cu_2O precipitation is estimated as 2.65%. It is difficult to directly calculate the resistivity contributed from Cu_2O; the Klemens model [127] is used to estimate the electrical conductivity of the Cu-0.2O, since Cu with Cu_2O precipitates can be a composite. The electrical conductivity is expressed as follows:

$$\sigma_e = \sigma_m V_m + \sigma_r V_r - 1/3 V_r V_m \frac{(\sigma_m - \sigma_r)^2}{\sigma_m V_m + \sigma_r V_r} \tag{10}$$

Here, σ_e is the electrical conductivity of the Cu-0.2O, σ_m, σ_r represent the electrical conductivity of Cu matrix (53.9 MS/m) and Cu_2O reinforcement (1 MS/m), V_m, V_r signify the volume fraction of Cu matrix (99.735%) and Cu_2O reinforcement (0.265%), respectively. Taking the above calculation, the electrical conductivity of Cu-0.2O is estimated as 52.14 MS/m, corresponding to approximately 89.6% IACS. This value is slightly higher than the experimental results (85.5% IACS), as illustrated in **Fig. 3-12(d)**. Such deviation is mainly caused by other defects, like nanoscale pores and particle interfaces with poor metallic bonding.

A linear correlation exists between thermal and electrical conductivity in metallic materials, as heat transfer is predominantly mediated by electrons. According to the Wiedemann-Franz law [128], this relationship can be expressed as:

$$k_e = L\sigma_e T \tag{11}$$

Where k_e is the electron-mediated thermal conductivity, L signifies the Lorentz constant (2.44 × 10^{-8} W·K^{-2}), σ_e denotes electrical conductivity, and T is temperature. Based on the experimental electrical conductivity of 85.5% IACS, the theoretical thermal conductivity of cold-sprayed Cu-0.2O is estimated at 349 W/m·K. Taking the same calculation on pure Cu, the theoretical conductivity is 348 W/m·K, corresponding well with the experimental results (**Fig. 3-12(c)**). Since Cu with Cu_2O precipitates can be treated as a composite material—where Cu serves as the matrix and Cu_2O as the reinforcement—the thermal conductivity can be further described using Ivan's composite theory [129]:

$$k_c = k_m[1 + \frac{3V_f(\delta - 1)}{2 + \delta - V_f(\delta - 1)}] \tag{12}$$

Here, k_c denotes the thermal conductivity of the composite, while k_m represents that of the matrix (349 W/m·K calculated from the electrical conductivity); V_f signifies the volume fraction of the reinforcement (approximately 2.65% assuming all the oxygen precipitated), and δ is the ratio of the thermal conductivity of the reinforcement to that of the matrix. Given the thermal conductivity of Cu_2O at room temperature is ~6 W/m·K, resulting in δ of 1.72%. Applying this model yields a theoretical thermal conductivity of approximately 336 W/m·K, slightly exceeding experimental values. Discrepancy arises primarily from the increased grain boundary density and dislocation density, both of which scatter electrons, reducing their mean free path and thus diminishing thermal conductivity. According to the Kapitza resistance model [130], Liu et al. [131] demonstrated through simulations and experiments that thermal conductivity in nanoscale Cu grains improves with increasing grain size up to 1 μm, beyond which the effect plateaus. Given that the average grain sizes of cold-sprayed Cu-0.2O and pure Cu are 1.75 μm and 5.83 μm, respectively, the resulting thermal conductivity deviation is estimated at ~30 W/m·K. Furthermore, the elevated dislocation density induced by Cu_2O precipitation further reduces thermal conductivity. Dislocations act as defects that scatter both electrons and phonons—the primary heat carriers in metals [130]. Thus, the combined effects of grain boundaries and dislocations account for the observed deviation between experimental and theoretical thermal conductivity values.

3.6. Summary

In this study, we systematically investigated the feasibility of inducing Cu_2O nanoprecipitation within a copper matrix via CSAM. Following preliminary optimization of the processing parameters, the formation and distribution of Cu_2O precipitates were examined using advanced electron microscopy in conjunction with FEM simulations. The effects of these precipitates on the mechanical properties, as well as the thermal and electrical conductivity of the as-sprayed Cu-0.2O alloy, were quantitatively analyzed. Upon optimization of the processing parameters, the cold-sprayed Cu-0.2O alloy exhibited exceptional compressive strength with minimal compromise in conductivity. This represents a preliminary breakthrough in addressing the longstanding strength-conductivity trade-off in Cu and Cu-based materials fabricated via CSAM, thereby enhancing their potential for broader industrial applications.

The cooperation of Cu_2O precipitates into the Cu matrix successfully improves strength with little sacrifice of conductivity. Taking advantage of precipitation strengthening, investigating another more effective alloying element for Cu strengthening is essential. Sn was chosen as a candidate due to its similar atomic size and mass compared to Cu. Various intermetallic compounds between Cu and Sn facilitate a more effective strengthening effect of Sn compared to oxygen. We fabricated cold-sprayed Cu-Sn alloys with varying Sn content and investigated the underlying strengthening mechanism, as detailed in Chapter 4.

Chapter 4 Cu-Sn alloys with superior mechanical properties fabricated via CSAM

4.1. Introduction

Bronze, a Cu-Sn alloy, is among the most widely used alloys throughout human history. The performance of Cu-Sn alloys is largely determined by their tin content. The primary applications of Cu-Sn alloys are illustrated in **Fig. 4-1**. Generally, when the tin content is below 5 wt.%, the alloy exhibits good plasticity and moderate conductivity, making it suitable for electronic components such as electrical connectors and high-precision springs [62, 63, 65, 68]. As the tin content increases beyond 10 wt.%, mechanical properties, wear resistance, and corrosion resistance improve significantly [132], enabling their use in bearings, gears, and marine applications. However, conventional manufacturing methods for Cu-Sn alloys face several challenges. For example, high-tin bronze produced by traditional casting often contains defects like shrinkage cavities and micro-cracks. Moreover, a hard and brittle intermetallic phase known as the δ phase ($Cu_{41}Sn_{11}$) tends to segregate at grain boundaries due to insufficient cooling rates during casting [68]. This segregation substantially weakens the mechanical performance of Cu-Sn products, restricting their broader application [133].

To address the challenges encountered during the fabrication of Cu-Sn alloys, numerous studies have explored novel strategies for producing high-performance Cu-Sn materials. Current methods to suppress δ phase segregation include increasing the solidification rate and adding alloying elements. CSAM, a solid-state deposition technique, presents a promising alternative for fabricating Cu-Sn alloys. This process primarily uses metal powders as feedstock, which are carried by inert gases (N_2 or Ar) through a specially designed Laval nozzle, accelerating them to supersonic velocities. Upon exiting the nozzle, the powders impact the substrate and form a dense deposit without melting and with minimal oxidation, preserving the original state of the powders. Deposition occurs through severe plastic deformation at an ultra-high strain rate. The resulting work-hardening effect promotes extensive dislocation accumulation, leading to significant strengthening. Additionally, the process achieves a high cooling rate [134], as supported by experimental data and numerical simulations, which inhibits the formation of the brittle δ phase during fabrication. Therefore, CSAM is considered an effective method to produce Cu-Sn alloys with reduced defects and superior mechanical properties.

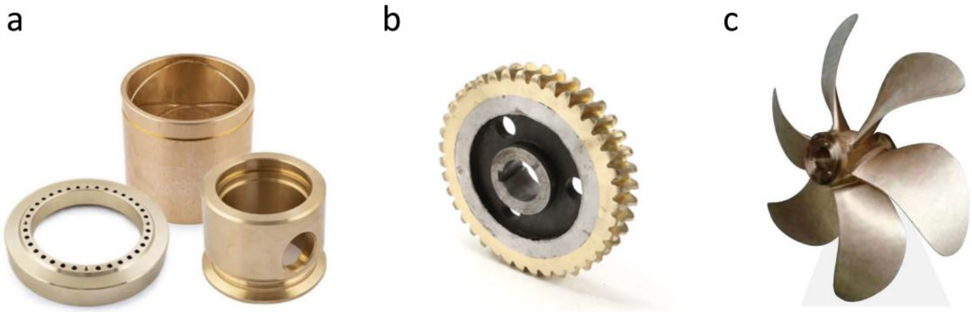

Fig. 4-1 Main applications of Cu-Sn alloys. (a) Cu-Sn bearings. (b) Cu-Sn gears. (c) Screw propeller in the marine industries.

Several recent studies have focused on Cu-Sn coatings fabricated by cold spray. Guo et al. [135] used two types of pre-alloyed Cu-Sn powders, containing 6.5 wt.% and 8.5 wt.% Sn, to produce Cu-6Sn and Cu-8Sn coatings, respectively. The as-sprayed samples were heat-treated in vacuum at 600 °C for 3 hours to examine the effects of heat treatment on their tribological performance. It was found that increasing the tin content reduced the wear rate, thereby improving wear resistance. Although heat treatment enhanced relative density by eliminating weak bonding interfaces, the associated thermal softening significantly decreased hardness and wear resistance. Similarly, Ozdemir et al. [136] fabricated Cu-10Sn coatings via low-pressure cold spray and conducted preliminary investigations on wear and corrosion behavior. The as-sprayed Cu-10Sn coatings exhibited superior hardness compared to conventionally sintered counterparts. During wear tests, higher applied loads resulted in reduced wear rates, attributed to the smearing of Sn-rich particles on the contact surface. However, most existing research has concentrated on cold-sprayed anti-wear coatings, with limited exploration of bulk-like Cu-Sn alloys fabricated by CSAM with enhanced mechanical properties. Moreover, studies on the microstructure evolution of Cu-Sn alloys during spraying remain scarce. To address these gaps and investigate the unique microstructure of cold-sprayed Cu-Sn alloys with varying Sn content, this study employed two pre-alloyed tin-bronze powders containing 5 wt.% and 10 wt.% Sn as feedstocks to fabricate Cu-5Sn and Cu-10Sn alloys. We characterized their relative density, mechanical properties, and cross-sectional microstructure, and conducted a preliminary analysis of how Sn content affects the microstructure and mechanical performance of the as-sprayed Cu-Sn alloys.

4.2. Experimental Results

4.2.1. Relative density

The cross-sectional microstructure of as-sprayed Cu-5Sn and Cu-10Sn samples, captured by optical microscopy (OM), is shown in **Fig. 4-2**. After mechanical grinding and polishing, the interfaces between adjacent particles became clearly visible. The particles underwent severe plastic deformation during deposition, resulting in a compressed lamellar shape. Some micro-cracks and pores were primarily observed at the particle interfaces (the black areas in **Figs. 4-2(a)** and **(b)**), indicating insufficient metallurgical bonding in both Cu-5Sn and Cu-10Sn samples. The corresponding porosity values are presented in **Fig. 4-2(c)**, showing an increase from 1.2% to 2.2% as the Sn content rises. Powder morphology is believed to influence both deposition efficiency and compactness. As previously illustrated in **Fig. 2-4**, the Cu-5Sn and Cu-10Sn powders exhibit relatively low sphericity, suggesting their mobility and deformability are more limited compared to spherical powders. Furthermore, the addition of Sn to the Cu matrix strengthens the powder, increasing resistance to deformation. Consequently, the porosity of the as-sprayed samples increases with Sn content, rising from 5 wt.% to 10 wt.%.

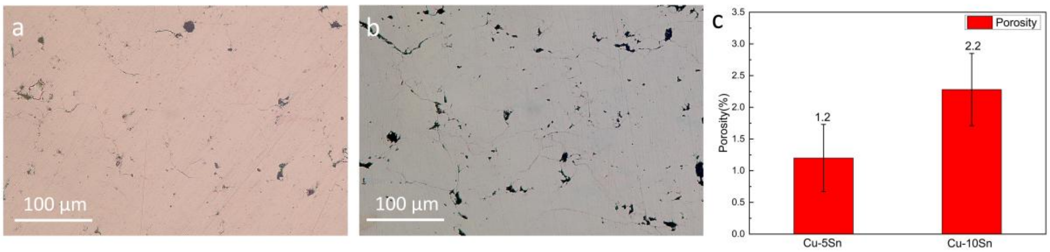

Fig. 4-2 Cross-sectional optical graphs of Cu-Sn alloys. (a) Cross-sectional microstructure of Cu-5Sn. (b) Cross-sectional microstructure of Cu-10Sn. (c) Corresponding porosity of as-sprayed Cu-5Sn and Cu-10Sn samples.

4.2.2. Mechanical performances

The mechanical performance of as-sprayed Cu-5Sn and Cu-10Sn samples is presented in **Fig. 4-3**. Microhardness values were calculated based on the applied load and the size of indentations on the cross-sections of the samples. As shown in **Fig. 4-3(a_1)** and **(a_2)**, the indentation area of Cu-5Sn is larger than that of Cu-10Sn, indicating greater deformation under the same load. Consequently, Cu-10Sn exhibits higher hardness than Cu-5Sn, as shown in **Fig. 4-3(a)**. Additionally, the standard deviation of microhardness in Cu-10Sn is lower, reflecting a more uniform hardness distribution. During the spraying process, after the initial layers are deposited, subsequent powder particles continuously compact the top surface, causing secondary plastic deformation and enhancing the hardness and strength of the lower layers. This phenomenon is known as the tamping effect. Although tamping improves mechanical properties at the bottom layers, it creates a hardness gradient from bottom to top since the effect is less pronounced near the surface. With increasing Sn content, the strengthened Cu-Sn alloys resist secondary plastic deformation more effectively, resulting in a more uniform hardness distribution in Cu-10Sn compared to Cu-5Sn.

The compressive performance of as-sprayed Cu-5Sn and Cu-10Sn is shown in **Fig. 4-3(b)**. The Cu-5Sn sample demonstrated a compressive yield strength exceeding 600 MPa and an ultimate compressive strength of 900 MPa. In comparison, Cu-10Sn exhibited significantly higher strengths, with a yield strength of 950 MPa and an ultimate compressive strength of 1200 MPa. Additionally, Cu-5Sn yielded earlier than

Cu-10Sn, suggesting that increasing Sn content may slightly reduce the Young's modulus of the as-sprayed Cu-Sn alloys. They both showcased much higher compressive strength than pure Cu. **Fig. 4-3(c)** provides a comprehensive comparison of compressive properties among our cold-sprayed Cu-5Sn, Cu-10Sn, and other Cu-Sn-based alloys. It clearly shows that Cu-10Sn alloys possess superior compressive strength compared to all others, with minimal loss in ductility. The underlying mechanisms responsible for these outstanding compressive properties will be discussed later.

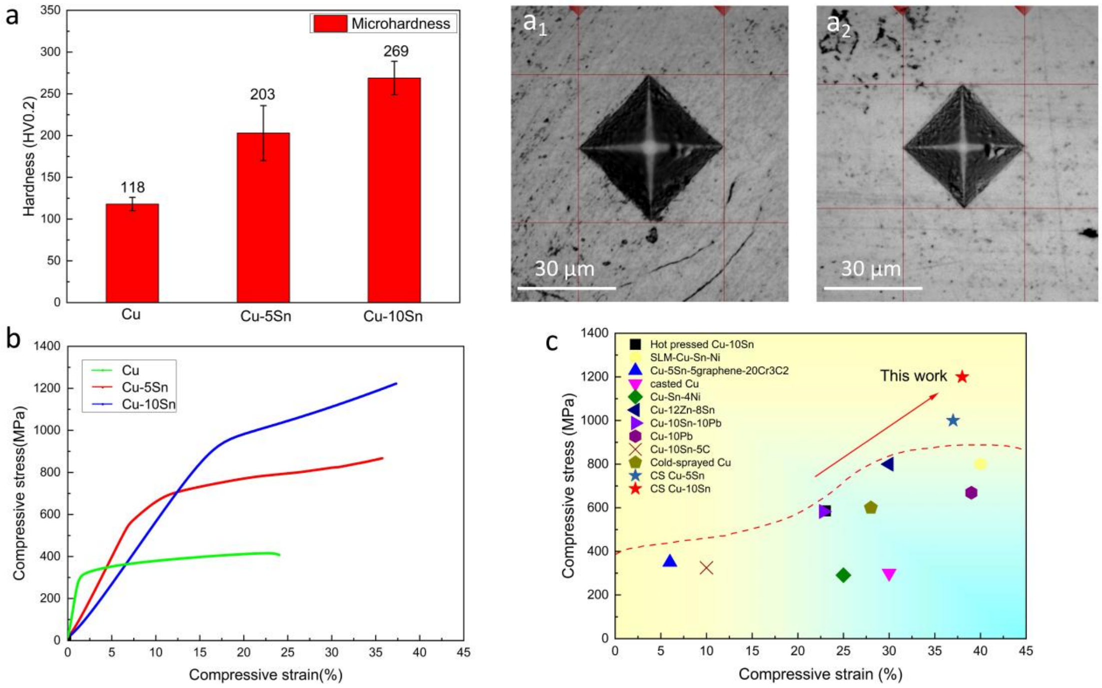

Fig. 4- 3 Mechanical performances of as-sprayed Cu-5Sn and Cu-10Sn alloys. (a) Microhardness comparison between Cu-5Sn and Cu-10Sn; (a_1) Indentation of the microhardness test of Cu-5Sn; (a_2) Indentation of the microhardness test of Cu-10Sn. (b) Compressive stress-strain curves of Cu-5Sn and Cu-10Sn. (c) Comprehensive comparison of compressive properties among our Cu-5Sn, Cu-10Sn, and other Cu-Sn alloys [137-141].

4.2.3. Microstructure characterization of Cu-Sn alloys

The Cu-Sn phase diagram, along with the phase compositions of the as-sprayed Cu-5Sn and Cu-10Sn samples, is presented in **Fig. 4-4**. Both alloys consist of α-Cu solid solutions and intermetallic compounds. XRD analysis reveals that the main phases in Cu-5Sn are α-Cu, Sn, and $Cu_{10}Sn_3$, while Cu-10Sn also contains an additional η phase (Cu_6Sn_5). These differences in phase composition influence the microstructure of the alloys, which in turn affect their mechanical properties. Further details will be discussed in the following chapters.

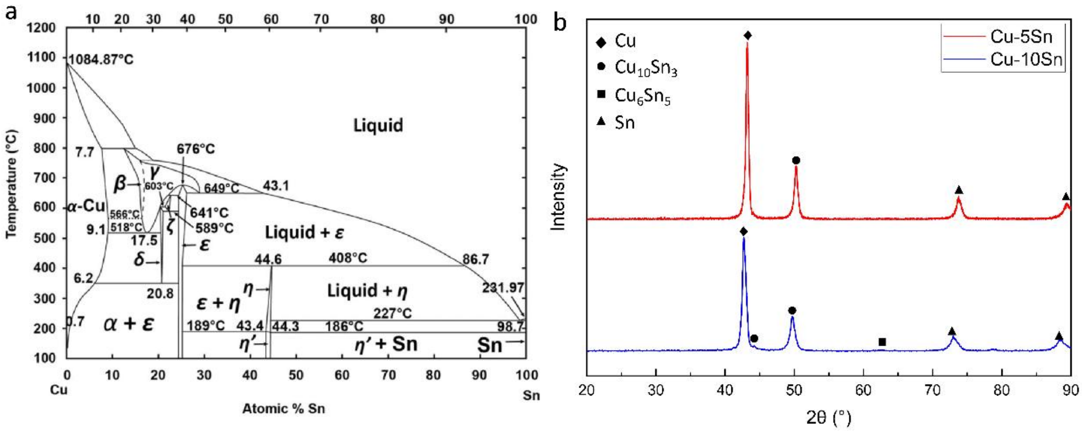

Fig. 4- 4 (a) Phase diagram of Cu-Sn binary system [142] and (b) corresponding XRD patterns of as-sprayed Cu-5Sn and Cu-10Sn.

The cross-sectional microstructure of as-sprayed Cu-5Sn and Cu-10Sn samples, observed by SEM, is shown in **Fig. 4-5**. The backscattered electron (BSE) mode, which primarily collects backscattered electrons, provides enhanced contrast based on elemental composition—heavier elements appear brighter, while lighter elements appear darker. The Cu-5Sn sample exhibited a relatively uniform microstructure, with small regions of Sn concentration indicating the presence of intermetallic compounds. In contrast, the Cu-10Sn sample showed a pronounced Sn-rich region at the center of the BSE image. This observation was further confirmed by corresponding EDS mappings. To quantify the Cu and Sn content in this area, line scanning was performed across the Sn-rich region, with results presented in **Fig. 4-6**. The Sn content remained around 10%, consistent with the feedstock composition, until the scan entered the concentrated Sn region, where the Sn percentage abruptly increased to over 20%. This hierarchical elemental distribution over a large area is believed to significantly affect the grain structure, thereby contributing to the alloy's exceptional mechanical properties.

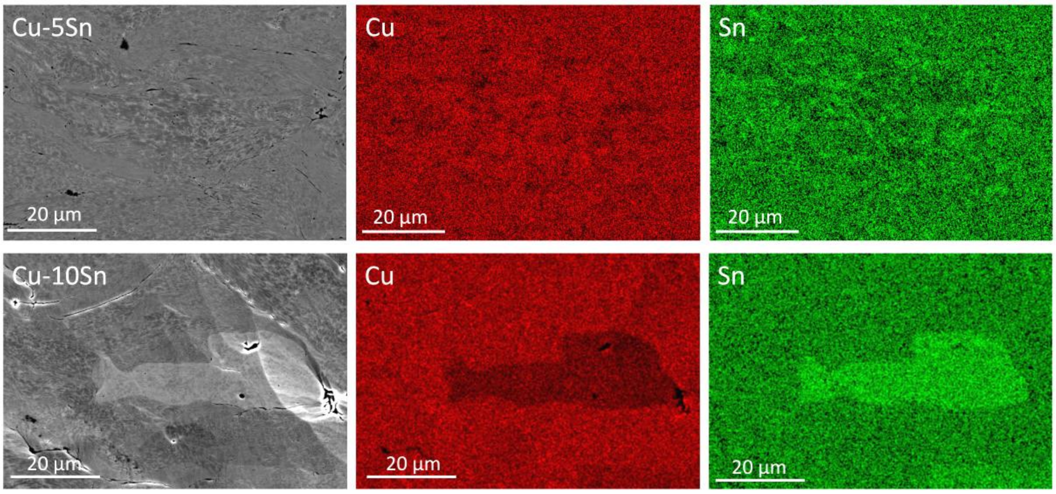

Fig. 4-5 BSE images illustrate the cross-sectional microstructure of the as-sprayed Cu-5Sn and Cu-10Sn alloys along with their corresponding EDS mappings. The upper three images refer to the Cu-5Sn, and the lower three represent the Cu-10Sn sample.

Table 4-1 Element distribution of Cu-5Sn and Cu-10Sn in **Fig.4-5**.

Element fraction (wt.%)	Cu	Sn
Cu-5Sn	94.7	5.3
Cu-10Sn	90.8	9.2

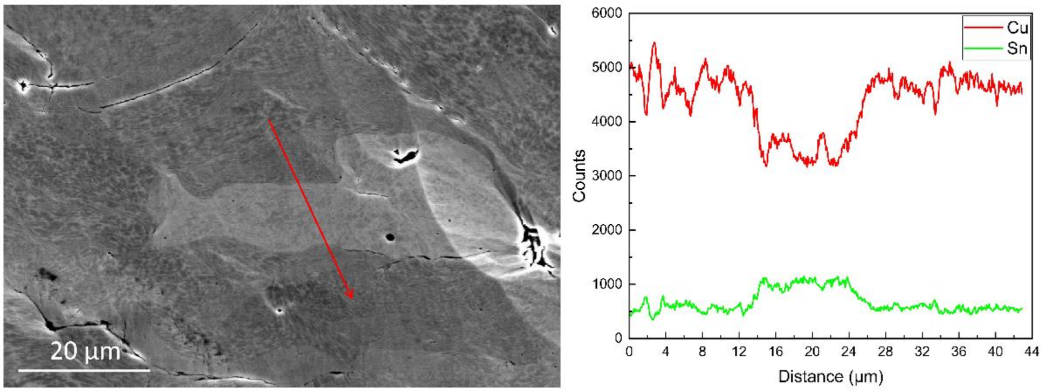

Fig. 4-6 EDS line scan showing the relative content of Cu and Sn. The red arrow represents the trace of the line scanning.

EBSD characterization was conducted on the as-sprayed Cu-5Sn and Cu-10Sn samples, with the results presented below. The phase constitution of these samples is shown in **Fig. 4-7**. The Cu-5Sn sample exhibited a relatively uniform phase distribution, predominantly consisting of α-Cu (Sn) solid solution, with some intermetallic compounds located at particle interfaces (the completely black regions in **Fig. 4-7(a)** represent these interfaces). In contrast, the Cu-10Sn sample displayed a hierarchical phase distribution. The area circled by the blue dashed line corresponds to the Sn-rich region identified in **Fig. 4-6**. This region contains a substantial amount of $Cu_{10}Sn_3$, along with some Sn and Cu_6Sn_5 intermetallic phases. Meanwhile, the particle interiors at the center of the image are primarily composed of Cu and Cu_6Sn_5 phases, as illustrated in **Fig. 4-7(b).**

The grain structures and GND distributions of the as-sprayed Cu-5Sn and Cu-10Sn samples are presented in **Fig. 4-8**. Both samples exhibit a characteristic bimodal microstructure, with ultra-fine grains located at inter-particle interfaces and relatively coarse grains within the particle interiors, as shown in **Figs. 4-8(a)** and **(b)**. Notably, the average grain size in Cu-10Sn is smaller than that in Cu-5Sn, despite both showing bimodal distributions. In the Cu-5Sn sample, some coarse grains exceed 3 μm in size, whereas nearly all grains in Cu-10Sn are below 1.5 μm. Additionally, the fraction of ultra-fine grains smaller than 1 μm is significantly higher in Cu-10Sn compared to Cu-5Sn, as illustrated in **Figs. 4-8(c)** and **(d)**. These findings suggest that increasing Sn content promotes grain refinement, which contributes to the improved mechanical properties observed.

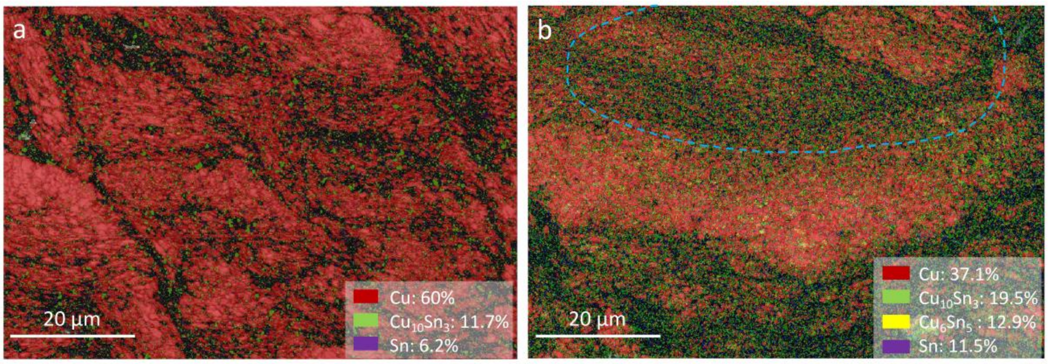

Fig. 4-7 Phase mappings of the as-sprayed Cu-Sn samples. (a) Phase mapping of Cu-5Sn. (b) Phase mapping of Cu-10Sn. Here, the region circled by blue dashed lines refers to the Sn concentration shown in **Fig. 4-6**.

The GND distribution of as-sprayed Cu-Sn alloys is shown in **Fig. 4-9.** For both samples, dislocations predominantly concentrate within the particle interior regions, as illustrated in **Figs. 4-9(a)** and **(b)**. Quantitative analysis reveals that the Cu-10Sn sample exhibits a GND density of 50.08 × 10^{14} m^{-2}, which is more than twice that of Cu-5Sn, measured at 22.43 × 10^{14} m^{-2}, as shown in **Figs. 4-9(c)** and **(d)**.

A summary of the experimental results is as follows: Both as-sprayed Cu-5Sn and Cu-10Sn exhibited enhanced mechanical properties compared to pure Cu, as discussed in Chapter 3. Increasing the Sn content further improved microhardness and compressive behavior, with the as-sprayed Cu-10Sn demonstrating superior compressive strength compared to Cu-Sn alloys produced by other conventional methods. Regarding microstructure, Cu-5Sn showed a relatively uniform phase and elemental distribution, while significant Sn segregation and phase concentration were observed in the Cu-10Sn sample. Although both samples displayed bimodal grain size distributions, the average grain size of Cu-10Sn was smaller than that of Cu-5Sn, indicating a more pronounced grain refinement effect. Additionally, the GND density of Cu-10Sn was more than twice that of Cu-5Sn. The mechanisms underlying the formation of this hierarchical structure and its strengthening effect will be discussed in the following sections.

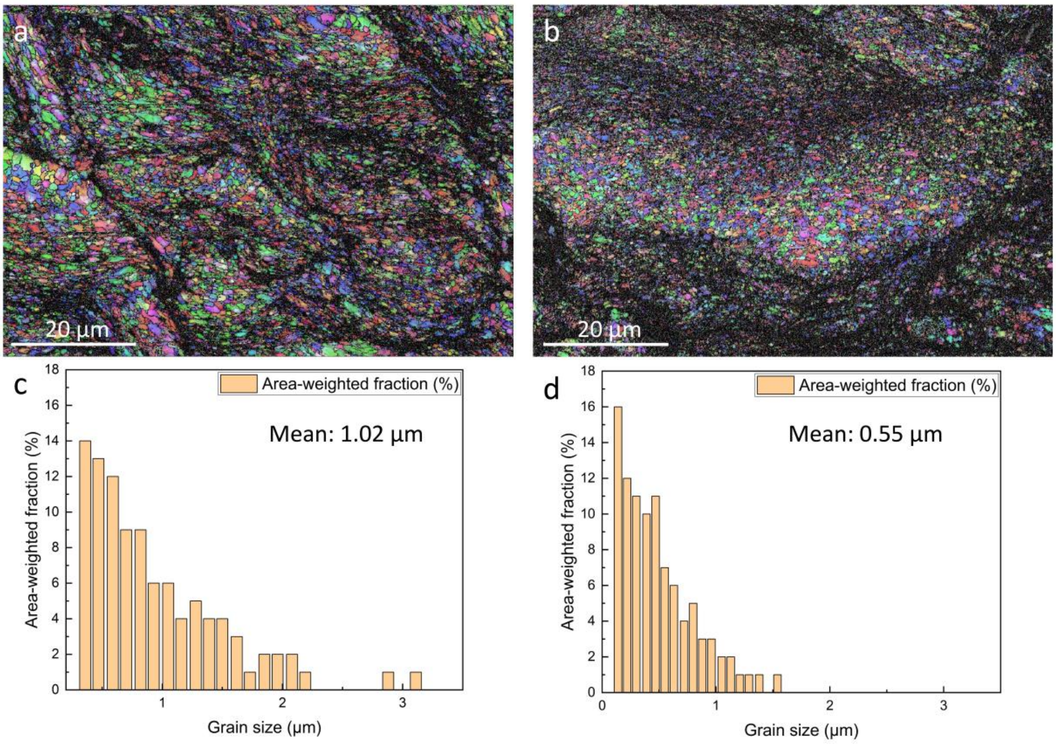

Fig. 4-8 IPF mappings and grain size distribution of as-sprayed Cu-Sn alloys. (a) IPF mapping of Cu-5Sn. (b) IPF mapping of Cu-10Sn. (c) Corresponding grain size distribution of Cu-5Sn. (d)

Corresponding grain size distribution of Cu-10Sn.

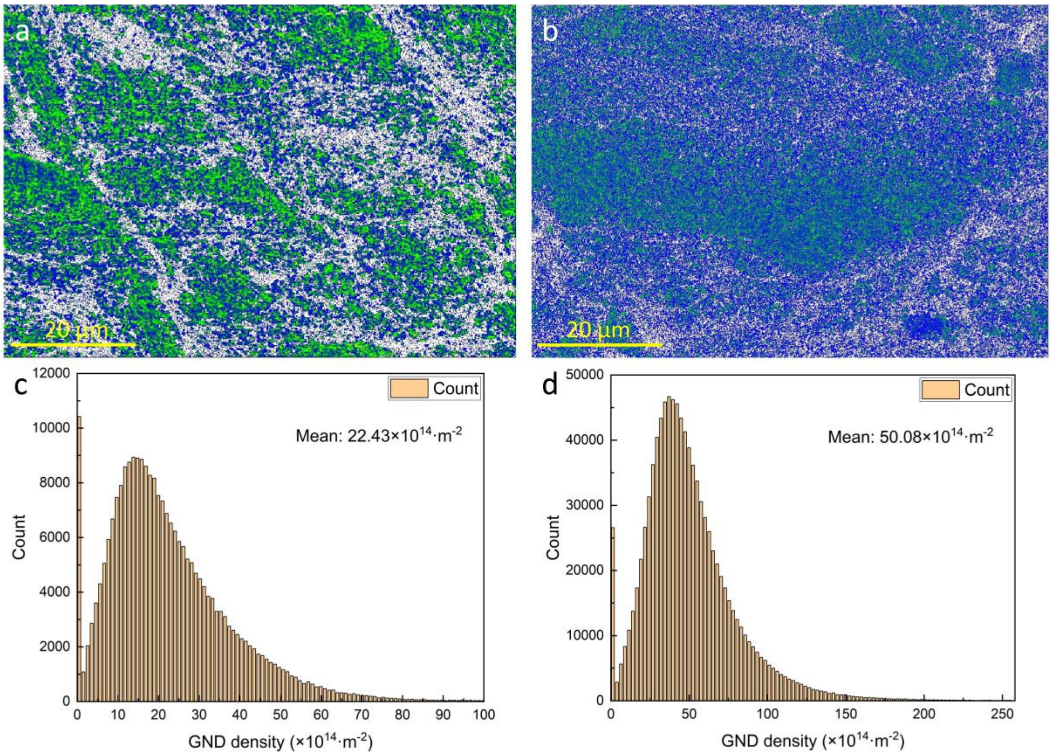

Fig. 4- 9 GND distribution of the as-sprayed Cu-5Sn and Cu-10Sn alloys. (a) GND density map of Cu-5Sn. (b) GND density map of Cu-10Sn. (c) Corresponding GND distribution of Cu-5Sn. (d) Corresponding GND distribution of Cu-10Sn.

4.3. Discussion

4.3.1. Origination of the chemical heterogeneity

Phase transformation in Cu-Sn alloys is primarily influenced by temperature. During deposition, the high kinetic energy of impacting powders converts to heat energy, causing a temperature rise at the interfaces between the particles and the substrate due to the extremely high strain rate (exceeding 10^9 s^{-1}). Over time, a temperature gradient develops within the deformed particle, with the highest temperature at the interfacial region and the lowest temperature in the particle interior. This mechanism in cold spray was confirmed by our previous simulation presented in Chapter 3. A schematic diagram of a Cu-10Sn powder during deposition is shown in **Fig. 4-10**. According to the Cu-Sn phase diagram (**Fig. 4-4(a)**), the particle interfaces—being the first to deform and reach elevated temperatures—favor the formation of the $Cu_{10}Sn_3$ intermetallic phase. The cooler powder interior promotes the presence of the η phase (Cu_6Sn_5) and α-Cu. Between these regions lies a transition zone with intermediate temperature, facilitating the coexistence of some Cu_6Sn_5 phase along with $Cu_{10}Sn_3$. Due to the complexity of the Cu-Sn binary system, further characterization techniques, such as HRTEM and STEM-HAADF, are necessary to verify this proposed mechanism.

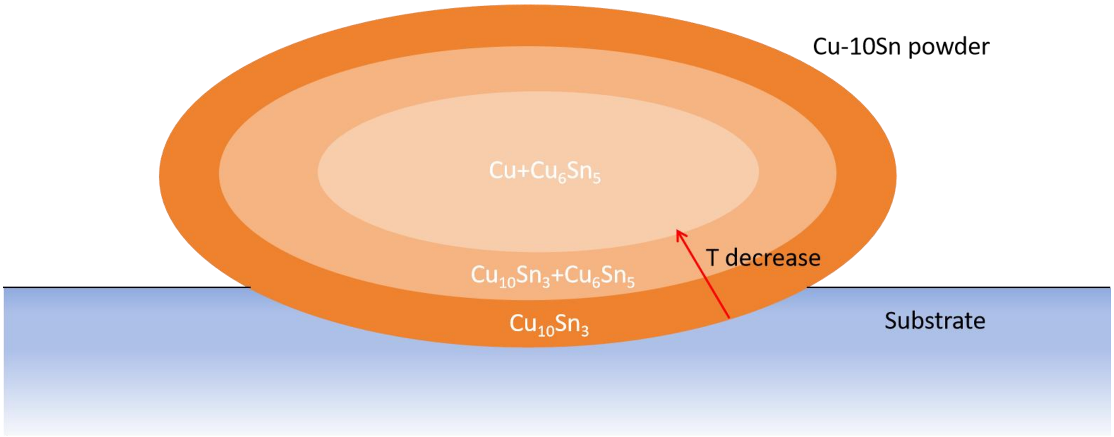

Fig. 4- 10 Schematic diagram of a single Cu-10Sn powder impacting the substrate with its phase distribution.

4.3.2. Impact of Sn content on recrystallization behavior

To further investigate the effect of Sn content on the microstructure of as-sprayed Cu-Sn alloys, grain orientation spread (GOS) mappings were generated for Cu-5Sn and Cu-10Sn. GOS reflects the average orientation deviation of pixels within a grain from the grain's mean orientation [143]. Higher GOS values indicate greater deformation. Based on established criteria, grains with GOS values below 2 are classified as fully recrystallized, those above 5 as deformed, and values between 2 and 5 represent substructures. As shown in **Figs. 4-11(a)** and **(b)**, over 70% of grains in Cu-10Sn were fully recrystallized, with only about 5% classified as deformed. In contrast, Cu-5Sn had less than 60% recrystallized grains and over 20% severely deformed grains. The average GOS value was 1.3 for Cu-10Sn and 2.81 for Cu-5Sn, more than twice that of Cu-10Sn, indicating a higher degree of recrystallization in Cu-10Sn.

Fig. 4-11(c) presents the percentages of low-angle grain boundaries (LAGB) and high-angle grain boundaries (HAGB) for both alloys. Consistent with our discussion in Chapter 3, dynamic recrystallization induced by ultra-high strain rates mainly occurs at particle interfaces, producing equiaxed ultra-fine grains with HAGBs. Cu-10Sn exhibited a higher fraction of HAGBs compared to Cu-5Sn, confirming that increasing Sn content promotes recrystallization.

This phenomenon is attributed to the differing melting points of the elements: Cu melts above 1000 ℃ [144], whereas Sn melts around 232 ℃ [145], much lower than Cu. The addition of Sn lowers the alloy's melting point, which correlates with a decrease in recrystallization temperature, typically about 40% of the melting point for metals. Thus, higher Sn content reduces the recrystallization temperature, enhancing the recrystallization process and resulting in more significant grain refinement.

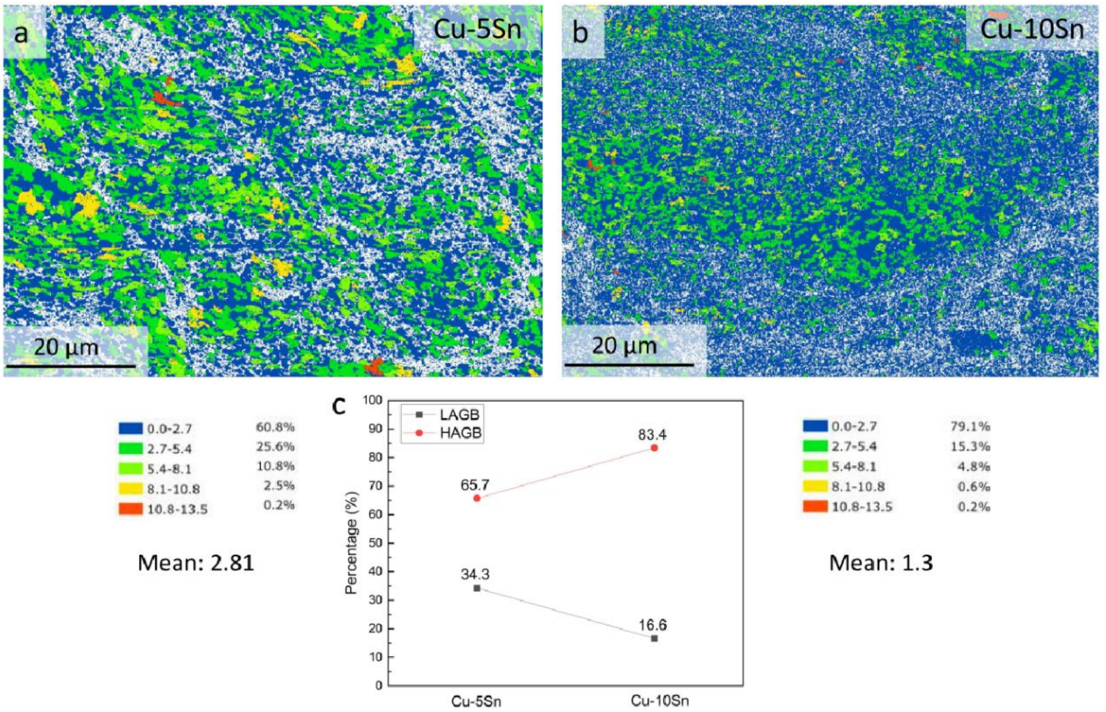

Fig. 4-11 GOS mappings of the as-sprayed Cu-Sn alloys. (a) GOS mapping of Cu-5Sn. (b) GOS mapping of Cu-10Sn. (c) Number fraction of low angle grain boundary (LAGB) and high angle grain boundary (HAGB) of Cu-5Sn and Cu-10Sn.

4.3.3. Enhanced mechanical properties

As shown in **Fig. 4-3**, both as-sprayed Cu-5Sn and Cu-10Sn exhibit enhanced mechanical properties compared to pure Cu. With increasing Sn content, both hardness and compressive strength improve. As discussed previously in Chapter 3, the strengthening of Cu-Sn alloys arises from several factors, including solid solution strengthening, grain boundaries, precipitation hardening, and dislocation strengthening. The overall strengthening mechanism can be expressed by the following formula:

$$\sigma_{ys} = \sigma_0 + \sigma_{gb} + \sigma_{ss} + \sigma_{dis} + \sigma_p \tag{13}$$

Where σ_{ys} represents the total yield strength; σ_0 denotes the intrinsic frictional stress of Cu-Sn, approximately 60.7 MPa [146]. σ_{gb} signifies the strength contributed by grain boundaries, σ_{ss} refers to the strengthening by solid solutions, σ_{dis} indicates the strength contributed by dislocations, and σ_p represents the strength attributed to precipitation. As for the grain boundary strengthening, the Hall-Petch effect [116, 117] was considered to calculate the strengthening effect, as expressed in the following formula:

$$\sigma_{gb} = k \cdot d^{-1/2} \tag{14}$$

Here, k is the constant based on the materials (0.356 MPa·m$^{1/2}$) [146] and d refers to the average grain size. Considering the mean grain size of 1.02 μm and 0.55 μm for the as-sprayed Cu-5Sn and Cu-10Sn alloys, the enhanced strength contributed from the grain boundaries is calculated to be 352 MPa and 481 MPa, respectively.

The dislocation strengthening effect can be drawn as follows:

$$\sigma_{dis} = M\alpha Gb \cdot \rho_{GND}^{1/2} \tag{15}$$

Where M is the Taylor factor, approximately 3 for Cu and its alloys; α is the Nye factor, around 0.2; G refers to the shear modulus (44.7 GPa); b is the Burgers factor (0.256 nm), and ρ_{GND} refers to the GND density by the EBSD characterization. As shown in **Fig. 4-9**, the GND density of as-sprayed Cu-5Sn and Cu-10Sn is 22.43×10^{14} /m^2 and 50.08×10^{14} /m^2, respectively. Taking the above calculations, the strength contributed by dislocation strengthening of Cu-5Sn and Cu-10Sn alloys is approximately 320 MPa and 480 MPa, respectively.

The solid solution strengthening in the as-sprayed Cu-Sn alloys can be summarized using the following formula [147]:

$$\sigma_{ss} = G\delta \mathrm{x}_{\alpha}^{3/2}\sqrt{\frac{\mathrm{x}_{\alpha}}{3}} \tag{16}$$

Where δ is the lattice distortion coefficient for Sn [148], approximately 0.22, and x_{α} represents the atomic fraction of the solid solution. According to the phase diagram, the corresponding atomic fraction of Sn is 2.7 % for Cu-5Sn (wt.%) and 5.9 % for Cu-10Sn (wt.%). After excluding the intermetallic compounds, the left atomic fraction of the solid solution for Cu-5Sn and Cu-10Sn is 1.8 at. % and 2.4 at. %, respectively. Assuming all left Sn atoms form solid solutions for simplification, the calculated σ_{ss} for Cu-5Sn and Cu-10Sn are 1.8 MPa and 3.3 MPa, which are neglected compared with the contributions from grain boundaries and dislocations. Based on the calculations, the theoretical strengths of the as-sprayed Cu-5Sn and Cu-10Sn are estimated to be 734.5 MPa and 1025 MPa, which correspond well with our experimental results, as illustrated in **Table 4-2**. Regarding precipitation strengthening arising from the intermetallic compounds in the as-sprayed Cu-5Sn and Cu-10Sn alloys, further characterization is required for the quantitative analysis of the distribution and size of these phases. This work will be undertaken in our future studies.

Table 4-2 Different strengthening mechanisms contributing to the yield strength of as-sprayed Cu-5Sn and Cu-10Sn (unit: MPa)

Sample	σ_0	σ_{gb}	σ_{dis}	σ_{ss}	σ_{ys} (Cal.)	σ_{ys} (Exp.)
Cu-5Sn	60.7	352	320	1.8	734.5	720
Cu-10Sn	60.7	481	480	3.3	1024	1004

4.4. Summary

In this study, Cu-5Sn and Cu-10Sn alloys were fabricated via cold spray additive manufacturing (CSAM). Both as-sprayed samples demonstrated high hardness and excellent compressive properties, which improved with increasing Sn content. Microstructural analysis revealed that the as-sprayed Cu-10Sn exhibited a heterogeneous phase distribution, with intermetallic phases concentrated at particle interfaces and α-Cu solid solution in the particle interiors, whereas the Cu-5Sn sample showed a relatively uniform chemical distribution. The increased Sn content lowered the recrystallization temperature of Cu-10Sn, thereby promoting dynamic recrystallization and enhancing grain refinement. The resulting severe plastic deformation led to a higher dislocation density, which, combined with the refined grains, contributed to the superior mechanical performance compared to Cu-5Sn. This work provides a preliminary investigation into the influence of Sn content on the microstructure and mechanical properties of cold-sprayed Cu-Sn alloys, highlighting their promising potential for industrial applications.

Chapter 5 Conclusions and future perspectives

5.1. Conclusions

In this thesis, we successfully fabricated Cu-O alloys and Cu-Sn alloys with varying Sn content using CSAM. The Cu-0.2O alloys demonstrated an exceptional balance of strength and thermal/electrical conductivity, presenting a novel approach to overcoming the strength-conductivity trade-off commonly observed in cold-sprayed Cu-based materials. The as-sprayed Cu-5Sn and Cu-10Sn alloys exhibited outstanding compressive performance, supporting their potential for broader industrial applications. The main conclusions of this thesis are summarized as follows:

(1) The spraying temperature and pressure have a significant impact on the properties of the deposited material. Increasing gas pressure and temperature enhances plastic deformation and work hardening, leading to a higher dislocation density and promoting dynamic recrystallization, which in turn results in grain refinement. Both refined grains and increased dislocation density contribute to improved microhardness. Furthermore, increasing the spraying pressure and temperature promotes improved metallurgical bonding between adjacent particles and minimizes the occurrence of defects, thereby enhancing both the thermal and electrical conductivity of cold-sprayed Cu coatings. Based on the optimization of processing parameters, a gas temperature of 700 °C and a gas pressure of 3.4 MPa were selected for the deposition process.

(2) Oxygen-bearing Cu alloys were successfully fabricated via CSAM, exhibiting an exceptional combination of mechanical and functional properties. These include hardness (~136 HV), yield strength (~480 MPa), thermal conductivity (310 W/m·K), and electrical conductivity (85.5% IACS). These properties surpass those of cast Cu and nearly all reported cold-sprayed Cu-ceramic composites.

(3) Detailed SEM and TEM analyses confirmed the presence of a substantial amount of Cu_2O precipitates in the Cu-0.2O samples, primarily concentrated near powder surfaces and grain boundaries. The formation and distribution of these Cu_2O nanoprecipitates are attributed to localized heat transfer and severe plastic

deformation occurring during particle impact in the cold spray process.

(4) The Cu_2O precipitates situated at grain boundaries effectively inhibit recovery and grain growth following recrystallization while providing a dislocation pinning effect. As a result, the mean grain size was refined from 5.83 μm to 1.75 μm, while the dislocation density increased from 9.47×10^{14} m^{-2} to 2.90×10^{15} m^{-2}. These microstructural modifications, in addition to the precipitation strengthening of Cu_2O, contribute significantly to the enhanced hardness and yield strength compared to pure Cu.

(5) Grain refinement and increased dislocation density serve as scattering centers for phonons and free electrons, thereby hindering thermal and electrical conduction. As a result, the presence of Cu_2O precipitates reduces both thermal and electrical conductivity. However, due to the relatively low volume fraction of Cu_2O, the overall conductivity remains competitive.

(6) Cu-5Sn and Cu-10Sn alloys were fabricated via CSAM. The as-sprayed alloys showcased high hardness (203 HV0.2 and 269 HV0.2) and outstanding compressive performances (yield strength of 720 MPa and 1004 MPa) compared with other Cu-Sn-based alloys.

(7) Compared to the as-sprayed Cu-5Sn, which exhibited a relatively uniform elemental distribution, the Cu-10Sn sample displayed a heterogeneous structure. Sn-rich intermetallic phases concentrated at the particle interfaces, while the α-Cu phase was located within the particle interiors, reflecting the temperature gradient developed during the spraying process.

(8) The increase in Sn content lowers the recrystallization temperature of the Cu-Sn alloys, thereby promoting dynamic recrystallization in Cu-10Sn and enhancing grain refinement. Additionally, higher Sn content facilitates greater plastic deformation during deposition, resulting in a higher dislocation density compared to as-sprayed Cu-5Sn. The combination of refined grains and increased dislocation density primarily drives the improved mechanical performance.

5.2. Future perspectives

Despite the conclusions reached in this thesis, several issues remain to be addressed. Further research will build upon this work, with the following future directions outlined:

(1) Although preliminary optimized processing parameters have been identified that enhance mechanical, thermal, and electrical properties, there is still potential for further improvement. Due to equipment limitations, the current maximum spraying temperature and pressure cannot be increased. Therefore, upgrading and modifying the spraying system to accommodate a wider range of parameters is the priority for ongoing work.

(2) Although the as-sprayed Cu-0.2O exhibits an excellent balance of strength and conductivity, the presence of nanoscale pores still adversely affects its properties. Conventional approaches to eliminate internal defects in cold-sprayed deposits, such as heat treatment and rolling, have limitations: heat treatment tends to reduce strength and hardness, while rolling alters the shape of the deposit and diminishes ductility. Therefore, it is crucial to develop novel strategies to eliminate defects and further enhance the performance of cold-sprayed Cu. Our future work will focus on devising a more effective method to heal these defects without compromising the material's inherent properties.

(3) In Chapter 3, we employed intentionally oxidized Cu powders to introduce 0.2 wt.% oxygen into the Cu matrix, resulting in the formation of Cu_2O precipitates during the spraying process. These precipitates enhanced the mechanical properties, albeit with a slight reduction in conductivity. However, the effects of varying amounts of Cu_2O precipitates on the microstructure and performance of as-sprayed Cu remain unclear. Therefore, my subsequent project aims to investigate the microstructural evolution, mechanical properties, and thermal/electrical conductivity of as-sprayed Cu-xO alloys, where x equals 0.1, 0.2, and 0.3. The influence of increasing Cu_2O precipitates on the microstructure and properties will be systematically examined using advanced electron microscopy techniques. By optimizing the oxygen content,

the sample exhibiting the best combination of properties will be identified, thereby guiding the future design of Cu-O alloys produced via CSAM.

(4) In Chapter 4, Cu-Sn alloys with varying Sn contents (5 wt.% and 10 wt.%) were fabricated via CSAM, exhibiting outstanding mechanical performance compared to other Cu-Sn-based alloys. The microstructures of the as-sprayed Cu-5Sn and Cu-10Sn were preliminarily characterized using SEM and EBSD. A heterogeneous phase distribution was observed in Cu-10Sn, attributed to the temperature gradient during deposition. However, the average size and distribution of the intermetallic phases have not yet been thoroughly investigated. Therefore, further characterization—such as HRTEM and STEM-HAADF—of the as-sprayed Cu-10Sn is necessary to confirm the presence of these phases and quantitatively analyze their strengthening effects. This work will be undertaken to complete the project.

(5) In Chapter 4, our investigation was limited to Cu-Sn alloys with two Sn contents (5 wt.% and 10 wt.%). To gain a more comprehensive understanding of the microstructure evolution and corresponding properties and thereby establish a clearer link between the alloys' microstructure and performance, future work will systematically examine Cu-Sn alloys over a broader range of Sn contents.

Publications

1. **Shengxi Jin**, Yifan Chen, Qi Liu, Chuanxi Ren, Hongning Wen, Yating Ran, Zibin Chen, Enhancing strength and thermal/electrical conductivity of cold sprayed copper via inducing Cu_2O precipitates, Materials Science and Engineering: A, submitted.

2. Qi Liu, **Shengxi Jin**, Chuanxi Ren, Dongdong Zhang, Ze Pu, Hongning Wen, Yating Ran, Xingdong Dan, Xuanlai Chen, Song Ni, Jing Lu, Zibin Chen, Reducing solidification cracks and enhancing mechanical performance in additively manufactured Cu-Ti alloys via chemical fluctuation manipulation, Virtual and Physical Prototyping 20(1) 2025 e2522274.

3. Chuanxi Ren, Tao Liang, **Shengxi Jin**, Zizheng Song, Xingdong Dan, Qi Liu, Yixuan Sun, Meng Wang, Yunbo Du, Chunjin Wang, Haobo Pan, Zibin Chen, Exceptional strength and antibacterial durability in hierarchically structured Cu-bearing 316L stainless steel through additive manufacturing, Journal of Materials Research and Technology 36 (2025) 5273-5285.

4. Chuanxi Ren, **Shengxi Jin**, Yifan Chen, Hengchao Shi, Yating Ran, Zizheng Song, Xingdong Dan, Qi Liu, Yixuan Sun, Haoran Sun, Zhiyuan Liu, Yuntian Zhu, Zibin Chen, Ultrahigh fatigue resistance enabled by heterostructural design, Microstructures, under revision.

References

[1] T. Watari, K. Nansai, K. Nakajima, Major metals demand, supply, and environmental impacts to 2100: A critical review, Resources, Conservation and Recycling 164 (2021) 105107.

[2] J. Miyake, G. Ghosh, M.E. Fine, Design of High-Strength, High-Conductivity Alloys, MRS Bulletin 21(6) (1996) 13-18.

[3] L. Lu, Y. Shen, X. Chen, L. Qian, K. Lu, Ultrahigh Strength and High Electrical Conductivity in Copper, Science 304(5669) (2004) 422-426.

[4] Z. Zhao, Y. Zhang, B. Tian, Y. Jia, Y. Liu, K. Song, A.A. Volinsky, Co effects on Cu-Ni-Si alloys microstructure and physical properties, Journal of Alloys and Compounds 797 (2019) 1327-1337.

[5] X. Guo, Z. Xiao, W. Qiu, Z. Li, Z. Zhao, X. Wang, Y. Jiang, Microstructure and properties of Cu-Cr-Nb alloy with high strength, high electrical conductivity and good softening resistance performance at elevated temperature, Materials Science and Engineering: A 749 (2019) 281-290.

[6] J.S. Dugdale, The electrical properties of metals and alloys, Courier Dover Publications2016.

[7] M.D. Merz, S.D. Dahlgren, Tensile strength and work hardening of ultrafine-grained high-purity copper, Journal of Applied Physics 46(8) (1975) 3235-3237.

[8] S.-P. Shen, W.-H. Chen, W.-P. Dow, T. Kamitamari, E. Cheng, J.-Y. Lin, W.-C. Chang, Copper seed layer repair using an electroplating process for through silicon via metallization, Microelectronic Engineering 105 (2013) 25-30.

[9] J. Fiebig, E. Bakan, T. Kalfhaus, G. Mauer, O. Guillon, R. Vaßen, Thermal Spray Processes for the Repair of Gas Turbine Components, Advanced Engineering Materials 22(6) (2020) 1901237.

[10] S.Y. Kim, H.-S. Lee, J.-H. Park, Deposition of Different Metallic Coatings as Repair Materials for Concrete by Using a Twin-Wire Arc Thermal Spray Process, Applied Sciences 12(23) (2022) 11874.

[11] C. Valente, T. Morgado, N. Sharma, LASER Cladding—A Post Processing Technique for Coating, Repair and Re-manufacturing, in: K. Gupta (Ed.), Materials Forming, Machining and Post Processing, Springer International Publishing, Cham, 2020, pp. 231-249.

[12] S. Grigoriev, A. Okunkova, A. Sova, P. Bertrand, I. Smurov, Cold spraying: From process fundamentals towards advanced applications, Surface and Coatings Technology 268 (2015) 77-84.

[13] S. Yin, P. Cavaliere, B. Aldwell, R. Jenkins, H. Liao, W. Li, R. Lupoi, Cold spray additive manufacturing and repair: Fundamentals and applications, Additive Manufacturing 21 (2018) 628-650.

[14] W. Li, K. Yang, S. Yin, X. Yang, Y. Xu, R. Lupoi, Solid-state additive manufacturing and repairing by cold spraying: A review, Journal of Materials Science & Technology 34(3) (2018) 440-457.

[15] C.J. Huang, H.J. Wu, Y.C. Xie, W.Y. Li, C. Verdy, M.P. Planche, H.L. Liao, G. Montavon, Advanced brass-based composites via cold-spray additive-manufacturing and its potential in component repairing, Surface and Coatings Technology 371 (2019) 211-223.

[16] A.P. Alkhimov, V.F. Kosarev, A.N. Papyrin, A method of "cold" gas-dynamic deposition, Soviet Physics Doklady 35 (1990) 1047.

[17] D. Herzog, V. Seyda, E. Wycisk, C. Emmelmann, Additive manufacturing of metals, Acta Materialia 117 (2016) 371-392.

[18] T. DebRoy, H.L. Wei, J.S. Zuback, T. Mukherjee, J.W. Elmer, J.O. Milewski, A.M. Beese, A. Wilson-Heid, A. De, W. Zhang, Additive manufacturing of metallic components – Process, structure and properties, Progress in Materials Science 92 (2018) 112-224.

[19] F.S. da Silva, N. Cinca, S. Dosta, I.G. Cano, M. Couto, J.M. Guilemany, A.V. Benedetti, Corrosion behavior of WC-Co coatings deposited by cold gas spray onto AA 7075-T6, Corrosion Science 136 (2018) 231-243.

[20] Q. Wang, N. Birbilis, M.-X. Zhang, On the Formation of a Diffusion Bond from Cold-Spray Coatings, Metallurgical and Materials Transactions A 43(5) (2012) 1395-1399.

[21] H. Wang, P. Li, W. Guo, G. Ma, H. Wang, Copper-Based Composite Coatings by Solid-State Cold Spray Deposition: A Review, Coatings 13(3) (2023) 479.

[22] P.C. King, G. Bae, S.H. Zahiri, M. Jahedi, C. Lee, An Experimental and Finite Element Study of Cold Spray Copper Impact onto Two Aluminum Substrates, Journal of Thermal Spray Technology 19(3) (2010) 620-634.

[23] M. Fukumoto, M. Mashiko, M. Yamada, E. Yamaguchi, Deposition Behavior of Copper Fine Particles onto Flat Substrate Surface in Cold Spraying, Journal of Thermal Spray Technology 19(1) (2010) 89-94.

[24] J. Karthikeyan, A. Kay, Cold spray processing of copper and copper alloys, 163 (2005).

[25] C. Huang, S. Yin, W. li, X. Guo, Cold Spray Technology and Its System: Research Status and Prospect, Surface Technology 50 (2021) 1-23.

[26] H. Assadi, F. Gärtner, T. Stoltenhoff, H. Kreye, Bonding mechanism in cold gas spraying, Acta Materialia 51(15) (2003) 4379-4394.

[27] M. Grujicic, C.L. Zhao, W.S. DeRosset, D. Helfritch, Adiabatic shear instability based mechanism for particles/substrate bonding in the cold-gas dynamic-spray process, Materials & Design 25(8) (2004) 681-688.

[28] M. Hassani-Gangaraj, D. Veysset, V.K. Champagne, K.A. Nelson, C.A. Schuh, Adiabatic shear instability is not necessary for adhesion in cold spray, Acta Materialia 158 (2018) 430-439.

[29] A. Fardan, C.C. Berndt, R. Ahmed, Numerical modelling of particle impact and residual stresses in cold sprayed coatings: A review, Surface and Coatings Technology 409 (2021) 126835.

[30] M. Hassani-Gangaraj, D. Veysset, V.K. Champagne, K.A. Nelson, C.A. Schuh, Response to Comment on “Adiabatic shear instability is not necessary for adhesion in cold spray”, Scripta Materialia 162 (2019) 515-519.

[31] J. Lienhard, C. Crook, M.Z. Azar, M. Hassani, D.R. Mumm, D. Veysset, D. Apelian, K.A. Nelson, V. Champagne, A. Nardi, C.A. Schuh, L. Valdevit, Surface oxide and hydroxide effects on aluminum microparticle impact bonding, Acta Materialia 197 (2020) 28-39.

[32] A. Moridi, H.-G.S. M., G. M., M. and Dao, Cold spray coating: review of material systems and future perspectives, Surface Engineering 30(6) (2014) 369-395.

[33] Y. Xie, S. Yin, C. Chen, M.-P. Planche, H. Liao, R. Lupoi, New insights into the coating/substrate interfacial bonding mechanism in cold spray, Scripta Materialia 125 (2016) 1-4.

[34] M. Grujicic, J.R. Saylor, D.E. Beasley, W.S. DeRosset, D. Helfritch, Computational analysis of the interfacial bonding between feed-powder particles and the substrate in the cold-gas dynamic-spray process, Applied Surface Science 219(3) (2003) 211-227.

[35] F. Gärtner, T. Stoltenhoff, J. Voyer, H. Kreye, S. Riekehr, M. Koçak, Mechanical properties of cold-sprayed and thermally sprayed copper coatings, Surface and Coatings Technology 200(24) (2006) 6770-6782.

[36] H. Zhou, C. Li, H. Yang, X. Luo, G. Yang, W. Li, T. Hussain, C. Li, Pores Structure Change Induced by Heat Treatment in Cold-Sprayed Ti6Al4V Coating, Journal of Thermal Spray Technology 28(6) (2019) 1199-1211.

[37] N.H. Tariq, L. Gyansah, X. Qiu, H. Du, J.Q. Wang, B. Feng, D.S. Yan, T.Y. Xiong, Thermo-mechanical post-treatment: A strategic approach to improve microstructure and mechanical properties of cold spray additively manufactured composites, Materials & Design 156 (2018) 287-299.

[38] H. Zhao, C. Tan, X. Yu, X. Ning, Z. Nie, H. Cai, F. Wang, Y. Cui, Enhanced reactivity of Ni-Al reactive material formed by cold spraying combined with cold-pack rolling, Journal of Alloys and Compounds 741 (2018) 883-894.

[39] Z. Zhao, N.u.H. Tariq, J. Tang, Y. Ren, H. Liu, M. Tong, L. Yin, H. Du, J. Wang, T. Xiong, Influence of annealing on the microstructure and mechanical properties

of Ti/steel clad plates fabricated via cold spray additive manufacturing and hot-rolling, Materials Science and Engineering: A 775 (2020) 138968.

[40] X. Qiu, N.u.H. Tariq, L. Qi, Y.-n. Zan, Y.-j. Wang, J.-q. Wang, H. Du, T.-y. Xiong, In-situ Sip/A380 alloy nano/micro composite formation through cold spray additive manufacturing and subsequent hot rolling treatment: Microstructure and mechanical properties, Journal of Alloys and Compounds 780 (2019) 597-606.

[41] G. Mauer, R. Singh, K.H. Rauwald, S. Schrüfer, S. Wilson, R. Vaßen, Diagnostics of Cold-Sprayed Particle Velocities Approaching Critical Deposition Conditions, Journal of Thermal Spray Technology 26(7) (2017) 1423-1433.

[42] H. Koivuluoto, J. Lagerbom, M. Kylmälahti, P. Vuoristo, Microstructure and Mechanical Properties of Low-Pressure Cold-Sprayed (LPCS) Coatings, Journal of Thermal Spray Technology 17(5) (2008) 721-727.

[43] H. Koivuluoto, A. Coleman, K. Murray, M. Kearns, P. Vuoristo, High Pressure Cold Sprayed (HPCS) and Low Pressure Cold Sprayed (LPCS) Coatings Prepared from OFHC Cu Feedstock: Overview from Powder Characteristics to Coating Properties, Journal of Thermal Spray Technology 21(5) (2012) 1065-1075.

[44] G. Sundararajan, N.M. Chavan, S. Kumar, The Elastic Modulus of Cold Spray Coatings: Influence of Inter-splat Boundary Cracking, Journal of Thermal Spray Technology 22(8) (2013) 1348-1357.

[45] P. Sudharshan Phani, D. Srinivasa Rao, S.V. Joshi, G. Sundararajan, Effect of Process Parameters and Heat Treatments on Properties of Cold Sprayed Copper Coatings, Journal of Thermal Spray Technology 16(3) (2007) 425-434.

[46] Y.-J. Li, X.-T. Luo, H. Rashid, C.-J. Li, A new approach to prepare fully dense Cu with high conductivities and anti-corrosion performance by cold spray, Journal of Alloys and Compounds 740 (2018) 406-413.

[47] J. Zou, G. Xu, K. Liu, J. Hao, E. Hao, L. Jia, X. Dong, G. Liu, L. Cui, Effect of carrier gas type on the microstructure and mechanical properties of alumina dispersion-strengthened copper for cold spray additive manufacturing, Journal of Alloys and Compounds 1022 (2025) 179983.

[48] G. Ghosh, J. Miyake, M.E. Fine, The systems-based design of high-strength, high-conductivity alloys, JOM 49(3) (1997) 56-60.

[49] K. Cao, M. Yu, C.M. Liang, H. Chen, Study on thermal conductivity of cold sprayed Cu coating, Surface Engineering 36(10) (2020) 1058-1066.

[50] Y. Zhang, Y. Epshteyn, R.R. Chromik, Dry sliding wear behaviour of cold-sprayed Cu-MoS2 and Cu-MoS2-WC composite coatings: The influence of WC, Tribology International 123 (2018) 296-306.

[51] S. Bai, L. Guan, Y. Zhang, Y. Wang, X. Zhang, Q. Gao, B. Fan, M. Li, B. Dong, B. Zhao, B. Song, R. Zhang, Enhanced tribological, electrical, and thermal properties of SiC/Cu composites by SiO2–Cu2O glass phase modification, Ceramics International 50(1, Part A) (2024) 750-756.

[52] Y. Chang, P. Mohanty, N. Karmarkar, M.T. Khan, Y. Wang, J. Wang, Microstructure and properties of Cu–Cr coatings deposited by cold spraying, Vacuum 171 (2020) 109032.

[53] O. Tazegul, V. Dylmishi, H. Cimenoglu, Copper matrix composite coatings produced by cold spraying process for electrical applications, Archives of Civil and Mechanical Engineering 16(3) (2016) 344-350.

[54] L. Zhang, Y. Zhang, H. Wu, S. Yang, X. Jie, Structure and corrosion behavior of cold-sprayed Cu/Ni composite coating post-treated by ultrasonic shot peening, SN Applied Sciences 2(2) (2020) 201.

[55] C. Lu, X. Feng, Y. Shen, Y. Tian, J. Jiang, L. Hu, Wear resistance and thermal conductivity of diamond/Cu-1Cr mechanical milled coatings after high temperature annealing, Diamond and Related Materials 97 (2019) 107438.

[56] L. Schramm, G. Behr, W. Löser, K. Wetzig, Thermodynamic reassessment of the Cu-O phase diagram, Journal of Phase Equilibria and Diffusion 26(6) (2005) 605-612.

[57] Q. Liu, C. Ren, Z. Song, X. Dan, J. Ju, T. Yang, S. Ni, J. Lu, L. Liu, J. Pan, Z. Chen, High-strength and high-conductivity additively manufactured Cu-O alloy enabled by cellular microstructure, Additive Manufacturing 88 (2024) 104244.

[58] R.N. Gu, P. Chen, Y.H. Zhou, H. Wang, X.C. Yan, K.S. Wong, M. Yan, Intentional Oxidation and Laser Remelting of Highly Reflective Pure Cu for Its High-Quality Additive Manufacturing, Advanced Engineering Materials 25(5) (2023) 2101138.

[59] Q. Lei, Z. Li, Y. Gao, X. Peng, B. Derby, Microstructure and mechanical properties of a high strength Cu-Ni-Si alloy treated by combined aging processes, Journal of Alloys and Compounds 695 (2017) 2413-2423.

[60] J. Chalon, J.D. Guérin, L. Dubar, A. Dubois, E.S. Puchi-Cabrera, Characterization of the hot-working behavior of a Cu-Ni-Si alloy, Materials Science and Engineering: A 667 (2016) 77-86.

[61] S. Semboshi, S. Sato, A. Iwase, T. Takasugi, Discontinuous precipitates in age-hardening CuNiSi alloys, Materials Characterization 115 (2016) 39-45.

[62] J.S. Park, C.W. Park, K.J. Lee, Implication of peritectic composition in historical high-tin bronze metallurgy, Materials Characterization 60(11) (2009) 1268-1275.

[63] A. Tavakoli, R. Liu, X.J. Wu, Improved mechanical and tribological properties of tin–bronze journal bearing materials with newly developed tribaloy alloy additive, Materials Science and Engineering: A 489(1) (2008) 389-402.

[64] T. Gustmann, J.M. dos Santos, P. Gargarella, U. Kühn, J. Van Humbeeck, S. Pauly, Properties of Cu-Based Shape-Memory Alloys Prepared by Selective Laser Melting, Shape Memory and Superelasticity 3(1) (2017) 24-36.

[65] S. Scudino, C. Unterdörfer, K.G. Prashanth, H. Attar, N. Ellendt, V. Uhlenwinkel, J. Eckert, Additive manufacturing of Cu–10Sn bronze, Materials Letters 156 (2015) 202-204.

[66] F.C. Walsh, C.T.J. Low, A review of developments in the electrodeposition of tin-copper alloys, Surface and Coatings Technology 304 (2016) 246-262.

[67] R.C. Barik, J.A. Wharton, R.J.K. Wood, K.S. Tan, K.R. Stokes, Erosion and erosion–corrosion performance of cast and thermally sprayed nickel–aluminium bronze, Wear 259(1) (2005) 230-242.

[68] P. Yang, D. He, W. Shao, Z. Tan, X. Guo, S. Lu, K. Anton, Study of the microstructure and mechanical properties of Cu–Sn alloys formed by selective

laser melting with different Sn contents, Journal of Materials Research and Technology 24 (2023) 5476-5485.

[69] M. Yan, Y. Wu, J. Chen, X. Zhou, Microstructure Evolution in Preparation of Cu-Sn Contact Wire for High-speed Railway, Advanced Materials Research 415-417 (2011) 446-451.

[70] Z. Mao, D.Z. Zhang, J. Jiang, G. Fu, P. Zhang, Processing optimisation, mechanical properties and microstructural evolution during selective laser melting of Cu-15Sn high-tin bronze, Materials Science and Engineering: A 721 (2018) 125-134.

[71] L. Broglie, H. Nishimura, Research on the theory of quanta, 2021.

[72] H. Busch, Berechnung der Bahn von Kathodenstrahlen im axialsymmetrischen elektromagnetischen Felde, Annalen der Physik 386(25) (1926) 974-993.

[73] M. Knoll, E. Ruska, Das Elektronenmikroskop, Zeitschrift für Physik 78(5) (1932) 318-339.

[74] E. Ruska, über Fortschritte im Bau und in der Leistung des magnetischen Elektronenmikroskops, Zeitschrift für Physik 87(9) (1934) 580-602.

[75] M. Knoll, Aufladepotentiel und Sekundäremission elektronenbestrahlter Körper, Z. Techn. Phys., 1935, p. 467.

[76] A.J. Wilkinson, T.B. Britton, Strains, planes, and EBSD in materials science, Materials Today 15(9) (2012) 366-376.

[77] W. Zhou, R. Apkarian, Z.L. Wang, D. Joy, Fundamentals of Scanning Electron Microscopy (SEM), in: W. Zhou, Z.L. Wang (Eds.), Scanning Microscopy for Nanotechnology: Techniques and Applications, Springer New York, New York, NY, 2007, pp. 1-40.

[78] A.J. Schwartz, M. Kumar, B.L. Adams, D.P. Field, Electron backscatter diffraction in materials science, Springer2009.

[79] D.B. Williams, C.B. Carter, The Transmission Electron Microscope, in: D.B. Williams, C.B. Carter (Eds.), Transmission Electron Microscopy: A Textbook for Materials Science, Springer US, Boston, MA, 2009, pp. 3-22.

[80] J. Wall, J. Langmore, M. Isaacson, A.V. Crewe, Scanning Transmission Electron Microscopy at High Resolution, Proceedings of the National Academy of Sciences 71(1) (1974) 1-5.

[81] Z. Chen, In-situ electron microscopy investigation of ferroelectric domain switching kinetics, 2017.

[82] E.G.T. Bosch, I. Lazić, Analysis of HR-STEM theory for thin specimen, Ultramicroscopy 156 (2015) 59-72.

[83] D.A. Muller, Structure and bonding at the atomic scale by scanning transmission electron microscopy, Nature Materials 8(4) (2009) 263-270.

[84] W. Pantleon, Resolving the geometrically necessary dislocation content by conventional electron backscattering diffraction, Scripta Materialia 58(11) (2008) 994-997.

[85] W.-Y. Li, C. Zhang, C.-J. Li, H. Liao, Modeling Aspects of High Velocity Impact of Particles in Cold Spraying by Explicit Finite Element Analysis, Journal of Thermal Spray Technology 18(5) (2009) 921-933.

[86] W.-Y. Li, W. Gao, Some aspects on 3D numerical modeling of high velocity impact of particles in cold spraying by explicit finite element analysis, Applied Surface Science 255(18) (2009) 7878-7892.

[87] B. Yildirim, S. Muftu, A. Gouldstone, Modeling of high velocity impact of spherical particles, Wear 270(9) (2011) 703-713.

[88] G. Bae, Y. Xiong, S. Kumar, K. Kang, C. Lee, General aspects of interface bonding in kinetic sprayed coatings, Acta Materialia 56(17) (2008) 4858-4868.

[89] S. Kumar, G. Bae, C. Lee, Deposition characteristics of copper particles on roughened substrates through kinetic spraying, Applied Surface Science 255(6) (2009) 3472-3479.

[90] S. Yin, X.-f. Wang, B.-p. Xu, W.-y. Li, Examination on the Calculation Method for Modeling the Multi-Particle Impact Process in Cold Spraying, Journal of Thermal Spray Technology 19(5) (2010) 1032-1041.

[91] S. Yin, X.-f. Wang, W.-y. Li, B.-p. Xu, Numerical Investigation on Effects of Interactions Between Particles on Coating Formation in Cold Spraying, Journal of Thermal Spray Technology 18(4) (2009) 686-693.

[92] G. Qiu, S. Henke, J. Grabe, Application of a Coupled Eulerian–Lagrangian approach on geomechanical problems involving large deformations, Computers and Geotechnics 38(1) (2011) 30-39.

[93] W.-Y. Li, H. Liao, C.-J. Li, H.-S. Bang, C. Coddet, Numerical simulation of deformation behavior of Al particles impacting on Al substrate and effect of surface oxide films on interfacial bonding in cold spraying, Applied Surface Science 253(11) (2007) 5084-5091.

[94] W.-Y. Li, S. Yin, X.-F. Wang, Numerical investigations of the effect of oblique impact on particle deformation in cold spraying by the SPH method, Applied Surface Science 256(12) (2010) 3725-3734.

[95] A. Manap, K. Ogawa, T. Okabe, Numerical Analysis of Interfacial Bonding of Al-Si Particle and Mild Steel Substrate by Cold Spray Technique Using the SPH Method, Journal of Solid Mechanics and Materials Engineering 6 (2012) 241-250.

[96] A. Manap, T. Okabe, K. Ogawa, Computer simulation of cold sprayed deposition using smoothed particle hydrodynamics, Procedia Engineering 10 (2011) 1145-1150.

[97] I. Smojver, D. Ivančević, Bird strike damage analysis in aircraft structures using Abaqus/Explicit and coupled Eulerian Lagrangian approach, Composites Science and Technology 71(4) (2011) 489-498.

[98] R. Johnson G, A Constitutive Model and Data for Metals Subjected to Large Strains, High Strain Rates and High Temperatures, Proceedings of the 7th International Symposium on Ballistics, The Hague, Netherlands, 1983 (1983).

[99] S. Yin, X.-f. Wang, W.Y. Li, H.-e. Jie, Effect of substrate hardness on the deformation behavior of subsequently incident particles in cold spraying, Applied Surface Science 257(17) (2011) 7560-7565.

[100] D. Poirier, J.-G. Legoux, P. Vo, B. Blais, J.D. Giallonardo, P.G. Keech, Powder Development and Qualification for High-Performance Cold Spray Copper Coatings on Steel Substrates, Journal of Thermal Spray Technology 28(3) (2019) 444-459.

[101] T. Stoltenhoff, C. Borchers, F. Gärtner, H. Kreye, Microstructures and key properties of cold-sprayed and thermally sprayed copper coatings, Surface and Coatings Technology 200(16) (2006) 4947-4960.

[102] Q. Chen, M. Yu, K. Cao, H. Chen, Thermal conductivity and wear resistance of cold sprayed Cu-ceramic phase composite coating, Surface and Coatings Technology 434 (2022) 128135.

[103] A. Sova, A. Papyrin, I. Smurov, Influence of Ceramic Powder Size on Process of Cermet Coating Formation by Cold Spray, Journal of Thermal Spray Technology 18(4) (2009) 633-641.

[104] H. Koivuluoto, P. Vuoristo, Effect of Powder Type and Composition on Structure and Mechanical Properties of Cu + Al2O3 Coatings Prepared by using Low-Pressure Cold Spray Process, Journal of Thermal Spray Technology 19(5) (2010) 1081-1092.

[105] F.S. da Silva, N. Cinca, S. Dosta, I.G. Cano, J.M. Guilemany, C.S.A. Caires, A.R. Lima, C.M. Silva, S.L. Oliveira, A.R.L. Caires, A.V. Benedetti, Corrosion resistance and antibacterial properties of copper coating deposited by cold gas spray, Surface and Coatings Technology 361 (2019) 292-301.

[106] S. Grigoriev, E. Gershman, I. Gershman, A. Mironov, Properties of Cold Spray Coatings for Restoration of Worn-Out Contact Wires, Coatings 11(6) (2021) 626.

[107] H. Okamoto, M.E. Schlesinger, E.M. Mueller, Alloy phase diagrams, Asm International2016.

[108] S. Yin, M. Meyer, W. Li, H. Liao, R. Lupoi, Gas Flow, Particle Acceleration, and Heat Transfer in Cold Spray: A review, Journal of Thermal Spray Technology 25(5) (2016) 874-896.

[109] F. Meng, S. Yue, J. Song, Quantitative prediction of critical velocity and deposition efficiency in cold-spray: A finite-element study, Scripta Materialia 107 (2015) 83-87.

[110] M.A. Meyers, Y.B. Xu, Q. Xue, M.T. Pérez-Prado, T.R. McNelley, Microstructural evolution in adiabatic shear localization in stainless steel, Acta Materialia 51(5) (2003) 1307-1325.

[111] A. Mishra, B.K. Kad, F. Gregori, M.A. Meyers, Microstructural evolution in copper subjected to severe plastic deformation: Experiments and analysis, Acta Materialia 55(1) (2007) 13-28.

[112] S. Liang, C. Wei, C. Ke, Effect of anisotropy in thermal conductivity on grain boundary migration under temperature gradient – A phase field study, Materials Letters 303 (2021) 130517.

[113] X.-M. Bai, Y. Zhang, M.R. Tonks, Testing thermal gradient driving force for grain boundary migration using molecular dynamics simulations, Acta Materialia 85 (2015) 95-106.

[114] D. Ouyang, Z.-Y. Liu, W.-L. Song, J. Pan, Y.-C. Xie, C. Zhang, L. Zhang, L. Liu, A novel void healing mechanism in cold sprayed nanostructured coating via grain boundary migration under low-temperature sintering, Additive Manufacturing 91 (2024) 104347.

[115] A. Mehta, L. Zhou, H. Hyer, T. Huynh, B. Lu, K. Graydon, E.J. Drobner, S.H. Park, Y. Sohn, Microstructural characteristics and mechanical properties of additively manufactured Cu–10Sn alloys by laser powder bed fusion, Materials Science and Engineering: A 838 (2022) 142775.

[116] E.O. Hall, The Deformation and Ageing of Mild Steel: III Discussion of Results, Proceedings of the Physical Society. Section B 64(9) (1951) 747.

[117] J. Petch N, The cleavage strength of polycrystals, J. Iron Steel Inst. 174 (1953) 25-28.

[118] H. Wen, T.D. Topping, D. Isheim, D.N. Seidman, E.J. Lavernia, Strengthening mechanisms in a high-strength bulk nanostructured Cu–Zn–Al alloy processed

via cryomilling and spark plasma sintering, Acta Materialia 61(8) (2013) 2769-2782.

[119] A. Ardell, Precipitation Hardening, Metallurgical Transactions A 16 (1985) 2131-2165.

[120] S. Qu, L. Wang, S. Zhang, C. Yang, H.Y. Chia, G. Wu, Z. Hu, J. Ding, W. Yan, Y. Zhang, C.H. Chan, W. Chen, Y. Lu, X. Song, Oxide-dispersion-enabled laser additive manufacturing of high-resolution copper, Nature Communications 16(1) (2025) 3234.

[121] A. Hadadzadeh, F. Mokdad, M.A. Wells, D.L. Chen, A new grain orientation spread approach to analyze the dynamic recrystallization behavior of a cast-homogenized Mg-Zn-Zr alloy using electron backscattered diffraction, Materials Science and Engineering: A 709 (2018) 285-289.

[122] H. Wen, J. Jin, X. Tang, X. Wang, H. Yang, Y. Zhang, L. Deng, P. Gong, Q. Wei, Y. He, J. Guo, Systematic analysis of distinct flow characteristics and underlying microstructural evolution mechanisms of a novel fine-grained P/M nickel-based superalloy during isothermal compression, Journal of Materials Science & Technology 162 (2023) 57-73.

[123] H. Wen, S. Wang, J. Jin, X. Wang, X. Tang, Y. Zhang, L. Deng, P. Gong, D. Li, B. Ning, Q. Wei, Deep learning-based modeling of the strain rate-dependent thermomechanical processing response for a novel HIPed P/M nickel-based superalloy, Journal of Materials Processing Technology 324 (2024) 118226.

[124] J.P. Hou, Q. Wang, Z.J. Zhang, Y.Z. Tian, X.M. Wu, H.J. Yang, X.W. Li, Z.F. Zhang, Nano-scale precipitates: The key to high strength and high conductivity in Al alloy wire, Materials & Design 132 (2017) 148-157.

[125] S. Qu, J. Ding, J. Fu, M. Fu, X. Song, Anisotropic material properties of pure copper with fine-grained microstructure fabricated by laser powder bed fusion process, Additive Manufacturing 59 (2022) 103082.

[126] S. Riedel, J. Röber, T. Geßner, Electrical properties of copper films produced by MOCVD, Microelectronic Engineering 33(1) (1997) 165-172.

[127] P.G. Klemens, Thermal conductivity of inhomogeneous media, High Temperatures. High Pressures (Print) 23(3) (1991) 241-248.

[128] N. Burger, A. Laachachi, M. Ferriol, M. Lutz, V. Toniazzo, D. Ruch, Review of thermal conductivity in composites: Mechanisms, parameters and theory, Progress in Polymer Science 61 (2016) 1-28.

[129] I.A. Starkov, A.S. Starkov, Maxwell–Garnett model for thermoelectric materials, International Journal of Solids and Structures 202 (2020) 226-233.

[130] A. Giri, P.E. Hopkins, J.G. Wessel, J.C. Duda, Kapitza resistance and the thermal conductivity of amorphous superlattices, Journal of Applied Physics 118(16) (2015).

[131] Y.-G. Liu, S.-B. Zhang, Z.-H. Han, Y.-J. Zhao, Influence of grain size on the thermal conduction of nanocrystalline copper, Acta Physica Sinica 65(10) (2016) 104401-104401.

[132] J. Zhang, X. Cui, Y. Wang, Y. Yang, J. Lin, Characteristics of ultrahigh electrical conductivity for Cu–Sn alloys, Materials Science and Technology 30(4) (2014) 506-509.

[133] Q. Liu, J. Shengxi, R. Chuanxi, Z. Dongdong, P. Ze, W. Hongning, R. Yating, D. Xingdong, C. Xuanlai, N. Song, L. Jing, Z. and Chen, Reducing solidification cracks and enhancing mechanical performance in additively manufactured Cu-Ti alloys via chemical fluctuation manipulation, Virtual and Physical Prototyping 20(1) (2025) e2522274.

[134] H. Assadi, H. Kreye, F. Gärtner, T. Klassen, Cold spraying – A materials perspective, Acta Materialia 116 (2016) 382-407.

[135] X. Guo, G. Zhang, W.-Y. Li, L. Dembinski, Y. Gao, H. Liao, C. Coddet, Microstructure, microhardness and dry friction behavior of cold-sprayed tin bronze coatings, Applied Surface Science 254(5) (2007) 1482-1488.

[136] I. Ozdemir, B. Bulbul, T. Grund, T. Lampke, Wear and Corrosion Behavior of Cold-Sprayed Cu-10Sn Coatings, Crystals 13(3) (2023) 523.

[137] Y.-K. Kim, S.-H. Park, K.-A. Lee, Effect of post-heat treatment on the thermophysical and compressive mechanical properties of Cu-Ni-Sn alloy

manufactured by selective laser melting, Materials Characterization 162 (2020) 110194.

[138] A. Nassef, M. El-Hadek, Microstructure and Mechanical Behavior of Hot Pressed Cu-Sn Powder Alloys, Advances in Materials Science and Engineering 2016(1) (2016) 9796169.

[139] H. Çelik, E. Aldırmaz, U. Sarı, Đ. Aksoy, Effect of cooling rate on stress-strain behaviour and micrustructure of Cu-Zn-Sn alloy, BPL 16(1) (2009) 161070.

[140] S.H. Huang, S.X. Chai, X.S. Xia, Q. Chen, D.Y. Shu, Compression Deformation Behavior and Processing Map of Pure Copper, Strength of Materials 48(1) (2016) 98-106.

[141] P. Kratochvíl, J. Mencl, J. Pešička, S.N. Komnik, The structure and low temperature strength of the age hardened Cu-Ni-Sn alloys, Acta Metallurgica 32(9) (1984) 1493-1497.

[142] S. Fürtauer, D. Li, D. Cupid, H. Flandorfer, The Cu–Sn phase diagram, Part I: New experimental results, Intermetallics 34 (2013) 142-147.

[143] S.W. Cheong, H. Weiland, Understanding a microstructure using GOS (grain orientation spread) and its application to recrystallization study of hot deformed Al-Cu-Mg alloys, Materials Science Forum, Trans Tech Publ, 2007, pp. 153-158.

[144] W. Hume-Rothery, G. Mabbott, W., K.M. Channel Evans, H.C.H. Carpenter, The freezing points, melting points, and solid solubility limits of the alloys of sliver and copper with the elements of the b sub-groups, Philosophical Transactions of the Royal Society of London. Series A, Containing Papers of a Mathematical or Physical Character 233(721-730) (1934) 1-97.

[145] Y. Liu, K.N. Tu, Low melting point solders based on Sn, Bi, and In elements, Materials Today Advances 8 (2020) 100115.

[146] H. Dybiec, The Hall-Petch relation in Cu-6 wt% Sn bronze, Journal of Materials Science Letters 9(6) (1990) 678-680.

[147] Y.S. Li, N.R. Tao, K. Lu, Microstructural evolution and nanostructure formation in copper during dynamic plastic deformation at cryogenic temperatures, Acta Materialia 56(2) (2008) 230-241.

[148] Z. Wu, Y. Gao, H. Bei, Thermal activation mechanisms and Labusch-type strengthening analysis for a family of high-entropy and equiatomic solid-solution alloys, Acta Materialia 120 (2016) 108-119.